

10. SITE 722¹

Shipboard Scientific Party²

HOLE 722A

Date occupied: 6 September 1987

Date departed: 8 September 1987

Time on hole: 37 hr

Position: 16°37.312'N, 59°47.755'E

Water depth (sea level; corrected m, echo-sounding): 2027.8

Water depth (rig floor; corrected m, echo-sounding): 2038.3

Bottom felt (m, drill pipe): 2034.0

Penetration (m): 280.0

Number of cores: 29

Total length of cored section (m): 280.0

Total core recovered (m): 225.96

Core recovery (%): 80.7

Oldest sediment cored:

Depth sub-bottom (m): 280.0

Nature: nannofossil ooze

Age: late Miocene

Measured velocity (km/s): 1.7

HOLE 722B

Date occupied: 8 September 1987

Date departed: 13 September 1987

Time on hole: 4 days, 23 hr

Position: 16°37.312'N, 59°47.755'E

Water depth (sea level; corrected m, echo-sounding): 2027.8

Water depth (rig floor; corrected m, echo-sounding): 2038.3

Bottom felt (m, drill pipe): 2033.2

Penetration (m): 565.6

Number of cores: 59

Total length of cored section (m): 565.6

Total core recovered (m): 385.9

Core recovery (%): 68.2

Oldest sediment cored:

Depth sub-bottom (m): 565.0

Nature: silty claystones

Age: early Miocene

Measured velocity (km/s): 2.21

Principal results: Site 722 is located in the Western Arabian Sea on the Owen Ridge and was drilled to recover a continuous upper Neogene sequence of pelagic sediments from an area of monsoonal upwelling.

The section penetrated at Site 722 ranges from early Miocene to Holocene in age and has been divided into four major lithologic units.

Unit I (0.0–221.5 mbsf) consists exclusively of alternating light and dark layers of foraminifer-bearing to foraminifer-nannofossil ooze and nannofossil ooze of Holocene to late Miocene age. Radiolarian and foraminiferal upwelling assemblages occur throughout this interval. The sediments of this unit reveal strong cyclicity that is indicated by changes in colors, bulk densities, carbonate content, and particularly well by magnetic susceptibility on whole-round cores. Sedimentation rates in lithologic Unit I range from 20 m/m.y. to about 45 m/m.y. and are lowest in the uppermost part of the upper Miocene and the lower Pliocene.

Unit II (221.5–343.4 mbsf) is composed of foraminifer-bearing, radiolarian-bearing, diatomaceous, and diatomaceous marly nannofossil chalks of late to middle Miocene age. Biogenic opal is an abundant component and its abundance is the major difference between lithologic Units I and II.

Unit III (343.4–411.1 mbsf) is primarily composed of white nannofossil chalk of middle Miocene age. Silica preservation is poor in the carbonate-rich chalks but increases dramatically at the boundary to lithologic Unit II in the uppermost part of the middle Miocene. The onset of silica preservation at this site coincides with the occurrence of upwelling faunas in the uppermost middle Miocene in Unit III.

Unit IV (411.1–565.6 mbsf) is early to middle Miocene in age. It is characterized by turbidite beds of silty clays capped by nannofossil chalks. The entire turbidite interval of early Miocene age becomes coarser downsection, where coarse basal layers with disseminated charcoal and pyrite are common in the silty clays. Preservation of planktonic calcareous and opaline tests is poor and the abundance of benthic foraminifers is low. The trend from turbiditic to increasingly pelagic deposition is related to the uplift of the Owen Ridge.

BACKGROUND AND OBJECTIVES

Site 722 is located near the crest of the Owen Ridge at 16°37.312'N and 59°47.755'E, at a water depth of 2028 m (Fig. 1). The site was selected at the intersection of two seismic lines collected on the site survey (RC2704). The site is located on Line 38 at 0745, 3 June 1986, and Line 1 at 2047, 19 May 1986 (Fig. 2).

Total sediment thickness (using Hamilton (1979) to convert two-way traveltime to thickness) at Site 722 is about 0.7 s (about 725 m) and the target depth is at 0.62 s (about 625 m). The upper part of the section (~290 mbsf) is characterized by relatively smooth, low-amplitude parallel reflectors that lie above a prominent but smooth reflector at 0.32 s (seismic reflector Owen Ridge A, OR-A). A second prominent reflector (Owen Ridge reflector B, OR-B) occurs at 0.53 s (about 520 mbsf). The interval between reflectors OR-A and OR-B is characterized by relatively flat lying, smooth, low-amplitude reflectors. The reflector sequence below OR-B has strongly dipping, high-amplitude reflectors lapping onto basement drape (reflectors conformable with acoustic basement) and an irregular surface thought to be a basement high. Correlation of the section at DSDP Site 224 with the seismic data from the site survey indicates that reflector OR-A is of late Miocene age and reflector OR-B is of middle to early Miocene age. The strongly reflective onlapping reflectors

¹ Prell, W. L., Niitsuma, N., et al., 1989. *Proc. ODP, Init. Repts.*, 117: Col- lege Station, TX (Ocean Drilling Program).

² Shipboard Scientific Party is as given in the list of Participants preceding the contents.

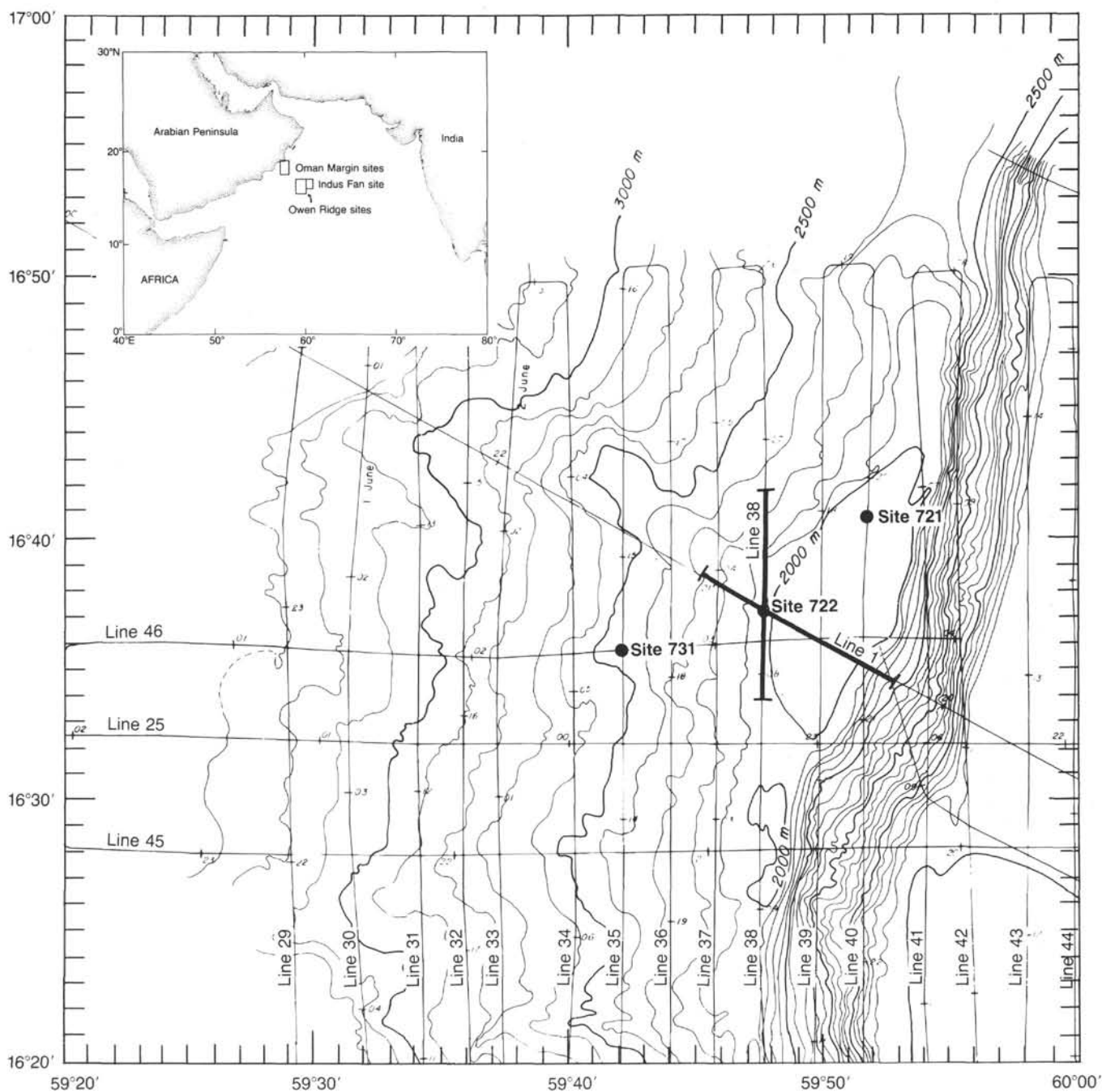


Figure 1. The location of Site 722 on the Owen Ridge. Bathymetry is from Sea Beam site survey data (Prell, unpubl. data). The portions of RC2704 seismic lines (Lines 1 and 38) (shown in Fig. 2) crossing Site 722 are indicated by the heavy lines.

of OR-B are thought to correlate to the detrital silts and claystones found in Site 224. The target depth in Site 722 is to penetrate these terrigenous sediments.

OPERATIONS

Moving the ship over 6 mi in dynamic positioning mode while tripping pipe, the rig relocated from Site 721 at 0230 on 07 September to the beacon dropped at Site 722 during the joint survey for Sites 721 and 722. The final position of Site 722 was established by Global Positioning System (GPS) as 16°37.312'N and 59°47.755'E. The first core was shot at 0455 in 2027.8 m water depth. For a plot of the ship's track during survey and positioning of the beacon, refer to "Operations" section, "Site 721" chapter (this volume).

Hole 722A was drilled by Advanced Piston Coring (APC) to Core 117-722A-9H (86.5 mbsf), when overpull rose to 50,000 pounds from previous 5,000 pounds and made deployment of the Extended Core Barrel (XCB) necessary. Cores 117-722A-5H to -9H were oriented. Recovery of the nine APC cores averaged 102%. Core 117-722A-29X was the last core to be cut in Hole 722A, which reached a total depth of 280.0 mbsf. Recovery in the XCB mode averaged 71%, so that overall recovery rate in Hole 722A averages 80.7%. The hole was terminated at this depth because the *in-situ* Pore-Water Sampler (PWS) became stuck in the flapper valve. The string had to be pulled up to retrieve the PWS and upon inspection of the Bottom-hole Assembly (BHA) the tool was found to be stuck at a flapper connection and was recovered on the rig floor. The ship offset 20 m to

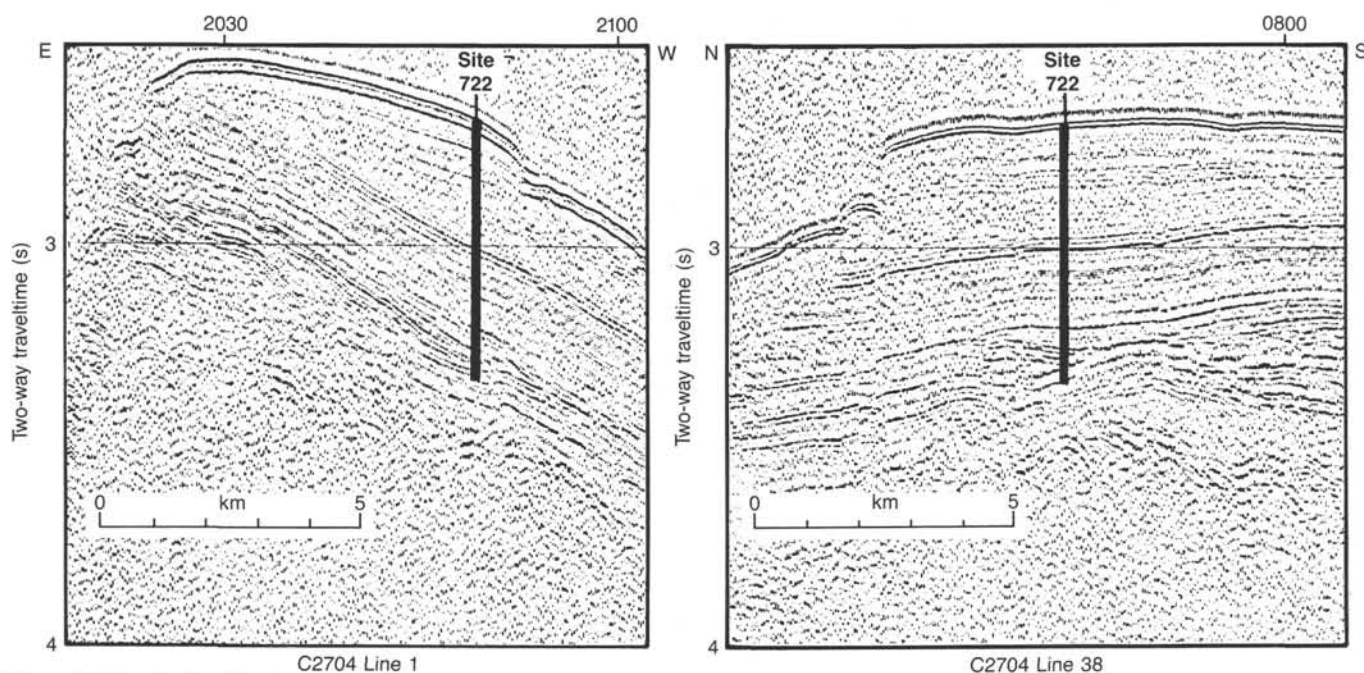


Figure 2. The seismic reflection profiles, Lines 1 and 38 of RC2704, that intersect Site 722. Track locations are shown in Figure 1.

the northwest, where Hole 722B was spudded at 1615 hr on 8 September.

In order to obtain the mud line and to overlap the cores of Holes 722A and 722B, the bit was positioned 5 m above the mud line when Core 117-722B-1H was shot. Ten APC cores with an average recovery of 103% were drilled to 91.9 mbsf, below which 25,000 pounds of overpull in Core 117-722B-10H made continuation by XCB necessary. Oriented cores were taken from Core 117-722B-7H to -10H. Total depth of 565.6 mbsf was reached with Core 117-722B-59X on 11 September (Table 1). The average recovery of XCB system was 61% and varied widely in response to variable lithology and sediment lithification. Overall recovery for Hole 722B was 68.3%.

Wiper trips to total depth and sweeping with polymer conditioned the hole for logging with the sidewall entry sub to facilitate removal of potential bridges. After two runs with the shifting tool to release the bit, the BHA was positioned 94.3 mbsf at the bottom of the section excellently recovered by APC. A string consisting of sonic, gamma ray, resistivity, and caliper tools was deployed first and obtained a good log from approximately 555.5 mbsf to the BHA at 94.3 mbsf in the first run. A second string with LD, CNL, and NGT tools was disabled by a short in the cable head, repaired, and deployed a second time. The run failed due to a defect in the swivel head of the tool, and it was decided to log without the SES after the hole conditions were established by running the pipe to the bottom of the hole. The third deployment of the second logging string was successful, and good logs were obtained from 71.4 mbsf to 550.9 mbsf (14 m above total depth).

Upon retrieval of the second logging string, the bowspring of the tool became stuck at the end of the BHA. 8,000 pounds of pull on the logging line failed to free the tool and a crimping tool was pumped down to crimp the logging line and subsequently cut it with a Kinley cutter. In order to be able to reenter the hole if the crimper had failed to hold the tool, a minicone was deployed before the drill string was pulled. The tool was found stuck in the BHA upon retrieval to the drill floor.

The ship was underway to Masirah Island at 1130 on 13 September to pick up two Omani shipboard participants before proceeding to the next target, Site 723 on the Oman margin.

LITHOSTRATIGRAPHY

Lithologic Units

Sediments recovered from Site 722 range from early Miocene to Holocene in age. The lithologies consist of nannofossil oozes and chalks, and fine-grained turbidites interbedded with nannofossil chalks. Site 722 sediments are divided into four lithologic units based on visual core descriptions, smear slide analysis, and calcium carbonate content (Table 2, Fig. 3). The lithologies at Site 722 are identical to those at Site 721, though Site 721 contains a hiatus between lithologic Units II and III. Thus, lithologic Units II and III are 100 and 40 m thicker, respectively, at Site 722 compared to Site 721. Further, lithologic Unit I at Site 721 contains disturbed (slumped) sediments which are not present at Site 722 (see "Lithostratigraphy" section, "Site 721" chapter, this volume).

Unit I (Depth: Hole 722A, 0–221.5 mbsf; Hole 722B, 0–221.5 mbsf; Age: Holocene to late Miocene)

Core 117-722A-1H to Section 117-722A-23X, CC, 2 cm; Core 117-722B-1H to Section 117-722B-24X-1, 72 cm.

Lithologic Unit I consists of alternating light and dark beds of foraminifer-bearing nannofossil ooze, nannofossil ooze/chalk, and marly nannofossil ooze/chalk. The beds range in thickness from 0.05 to 1.00 m. Bioturbation is minor to moderate throughout the unit; occasional pyrite-lined burrows were noted. Contacts between beds are generally gradational and mottled by burrows (Fig. 4). Light beds range in color from gray (5Y 6/1) to light olive gray (5Y 6/2), light gray (5Y 7/1, 7/2), and light greenish gray (5GY 7/1, 10Y 6/2). Darker beds range from pale olive (5Y 6/3) to olive gray (5Y 5/2), olive (5Y 4/3, 4/4, 5/3), and dark olive gray (5Y 3/2). Dark beds contain 10%–20% more silty clay than do the light beds. The average calcium carbonate content for this unit is 70%, ranging from 50% to 89% (Table 3, Fig. 5). The higher calcium carbonate values correspond to the lighter color beds.

Smear slide analysis indicates that nannofossils are the dominant sediment component throughout lithologic Unit I. Foraminifers range from 5% to 25% in the first four cores (roughly

Table 1. Coring summary, Site 722.

Core no.	Date (Sept. 1987)	Time	Depth (mbsf)	Cored (m)	Recovered (m)	Recovery (%)
117-722A-						
1H	7	0455	0.0-9.8	9.8	9.87	101.0
2H	7	0545	9.8-19.4	9.6	9.70	101.0
3H	7	0625	19.4-29.0	9.6	9.76	101.0
4H	7	0700	29.0-38.6	9.6	9.73	101.0
5H	7	0800	38.6-48.2	9.6	9.79	102.0
6H	7	0845	48.2-57.5	9.3	10.00	107.5
7H	7	0930	57.5-67.2	9.7	10.00	103.1
8H	7	1015	67.2-76.8	9.6	9.92	103.0
9H	7	1105	76.8-86.5	9.7	9.83	101.0
10X	7	1255	86.5-96.2	9.7	7.83	80.7
11X	7	1340	96.2-105.9	9.7	9.55	98.4
12X	7	1425	105.9-115.6	9.7	8.55	88.1
13X	7	1515	115.6-125.3	9.7	9.50	97.9
14X	7	1555	125.3-134.9	9.6	6.57	68.4
15X	7	1630	134.9-144.6	9.7	9.53	98.2
16X	7	1710	144.6-154.3	9.7	9.62	99.2
17X	7	1755	154.3-163.9	9.6	4.70	48.9
18X	7	1840	163.9-173.6	9.7	7.79	80.3
19X	7	1920	173.6-183.3	9.7	9.42	97.1
20X	7	2000	183.3-193.0	9.7	7.76	80.0
21X	7	2035	193.0-202.7	9.7	4.66	48.0
22X	7	2115	202.7-212.4	9.7	9.41	97.0
23X	7	2155	212.4-222.0	9.6	9.88	103.0
24X	7	2230	222.0-231.7	9.7	9.73	100.0
25X	7	2310	231.7-241.7	10.0	1.58	15.8
26X	7	2340	241.7-251.0	9.3	1.32	14.2
27X	8	0055	251.0-260.7	9.7	5.84	60.2
28X	8	0220	260.7-270.4	9.7	0.52	5.4
29X	8	0340	270.4-280.0	9.6	3.60	37.5
				280.0	225.96	
117-722B-						
1H	8	1700	0.0-5.5	5.5	5.53	100.0
2H	8	1730	5.5-15.1	9.6	9.56	99.6
3H	8	1810	15.1-24.7	9.6	10.08	105.0
4H	8	1840	24.7-34.3	9.6	9.89	103.0
5H	8	1910	34.3-43.9	9.6	9.79	102.0
6H	8	1950	43.9-53.2	9.3	9.94	107.0
7H	8	2025	53.2-62.9	9.7	10.10	104.1
8H	8	2100	62.9-72.5	9.6	9.84	102.5
9H	8	2155	72.5-82.2	9.7	10.04	103.5
10H	8	2235	82.7-91.9	9.2	10.05	109.2
11X	8	2325	91.9-101.5	9.6	6.06	63.1
12X	9	0005	101.5-111.2	9.7	4.59	47.3
13X	9	0045	111.2-120.9	9.7	4.44	45.8

0-40 mbsf), thereafter comprising from 0% to 5% of the sediment. Siliceous tests are present only in trace amounts within lithologic Unit I. Clays and inorganic calcite constitute the major terrigenous components. Clays range from 10% to 30%; the largest concentrations are found in the marly nannofossil oozes (darker beds) of cores 117-722A-6H to 117-722A-11X (roughly 45-100 mbsf). Inorganic calcite is found in amounts ranging from 5% to 10%. Other minerals (usually less than 5% of the sediment) include quartz, feldspar, mica, opaque minerals (pyrite?), and dolomite. Volcanic glass is also present in trace amounts.

Unit II (Depth: Hole 722A, 221.5-280.0 mbsf; Hole 722B, 221.5-343.4 mbsf; Age: late Miocene to middle Miocene)

Section 117-722A-23X-CC, 2 cm, to Section 117-722A-29X, CC, 12 cm; Section 117-722B-24X-1, 72 cm, to Section 117-722B-36X, CC, 45 cm.

Lithologic Unit II consists of alternating light and dark beds of nannofossil chalks, foraminifer-bearing nannofossil chalks, diatom-nannofossil chalks, radiolarian-bearing diatom-nannofossil chalks, and diatom-marly nannofossil chalks. Bioturbation is minor to moderate throughout the unit. Lighter beds range from white (10Y 8/1, 5Y 8/1) to light olive gray (5Y 6/2),

light gray (5Y 7/1, 7/2), light greenish gray (10Y 7/1, 7/2), and gray (5Y 6/1). Darker beds range from pale olive (5Y 6/3) to olive gray (5Y 5/2, 4/2), olive (5Y 5/3, 5/4), dark greenish gray (10Y 5/2), and dark olive gray (5Y 3/2).

The major difference between lithologic Units I and II is the presence of diatoms and radiolarians in the darker beds of Unit II. Smear slide analysis indicates that the biogenic silica content (primarily diatoms) gradually increases with depth, from trace amounts at the bottom of lithologic Unit I to a maximum (as much as 20%) in Cores 117-722B-27X to -35X (roughly 245-330 mbsf). The biogenic silica content declines sharply to 0% at the top of lithologic Unit III. The gradual increase in silica down-section in lithologic Unit II is also evident in the down-hole logs (see "Downhole Measurements" section, this chapter). The overall increase in biogenic silica in this unit is coincident with a decrease in the average calcium carbonate content from 70% in lithologic Unit I to 51% in lithologic Unit II (Table 3, Fig. 5).

The increase in biogenic silica in lithologic Unit II is further indicated by low grain density and bulk density and high porosity and water content values (see "Physical Properties" section, this chapter). Lithologic Unit II also contains an echelon, subvertical dewatering(?) structures (Fig. 6). These structures are coeval with the slump features and missing section in nearby Site 721 and may be genetically related. Similar structures were

Table 1 (continued).

Core no.	Date (Sept. 1987)	Time	Depth (mbsf)	Cored (m)	Recovered (m)	Recovery (%)
117-722B-						
14X	9	0120	120.9–130.5	9.6	9.52	99.1
15X	9	0155	130.5–140.2	9.7	1.76	18.1
16X	9	0230	140.2–149.9	9.7	9.48	97.7
17X	9	0300	149.9–159.5	9.6	9.59	99.9
18X	9	0340	159.5–169.2	9.7	9.75	100.0
19X	9	0415	169.2–178.9	9.7	7.92	81.6
20X	9	0455	178.9–188.5	9.6	4.23	44.0
21X	9	0530	188.5–198.2	9.7	5.74	59.2
22X	9	0605	198.2–207.9	9.7	9.18	94.6
23X	9	0645	207.9–217.5	9.6	7.88	82.1
24X	9	0725	217.5–227.2	9.7	9.72	100.0
25X	9	0810	227.2–236.9	9.7	9.49	97.8
26X	9	0840	236.9–246.5	9.6	9.34	97.3
27X	9	0920	246.5–256.2	9.7	9.76	100.0
28X	9	1025	256.2–265.9	9.7	3.21	33.1
29X	9	1130	265.9–275.6	9.7	9.59	98.8
30X	9	1230	275.6–285.3	9.7	2.21	22.8
31X	9	1330	285.3–295.0	9.7	9.28	95.7
32X	9	1440	295.0–304.7	9.7	6.52	67.2
33X	9	1545	304.7–314.3	9.6	5.00	52.1
34X	9	1650	314.3–324.0	9.7	5.70	58.7
35X	9	1800	324.0–333.7	9.7	9.93	102.0
36X	9	1900	333.7–343.4	9.7	5.91	60.9
37X	9	2005	343.4–353.1	9.7	9.74	100.0
38X	9	2110	353.1–362.8	9.7	9.38	96.7
39X	10	0000	362.8–372.5	9.7	3.00	30.9
40X	10	0215	372.5–382.2	9.7	3.70	38.1
41X	10	0400	382.2–391.8	9.6	2.37	24.7
42X	10	0615	391.8–401.4	9.6	5.31	55.3
43X	10	0830	401.4–411.1	9.7	3.65	37.6
44X	10	1050	411.1–420.8	9.7	7.67	79.1
45X	10	1250	420.8–430.5	9.7	9.76	100.0
46X	10	1430	430.5–440.2	9.7	9.94	102.0
47X	10	1555	440.2–449.8	9.6	0.00	0.0
48X	10	1705	449.8–459.4	9.6	1.13	11.8
49X	10	1845	459.4–469.0	9.6	6.43	67.0
50X	10	2005	469.0–478.6	9.6	6.21	64.7
51X	10	2130	478.6–488.2	9.6	1.36	14.1
52X	10	2305	488.2–497.9	9.7	9.88	102.0
53X	11	0030	497.9–507.6	9.7	1.22	12.6
54X	11	0140	507.6–517.2	9.6	0.92	9.6
55X	11	0340	517.2–526.9	9.7	0.66	6.8
56X	11	0540	526.9–536.6	9.7	0.34	3.5
57X	11	0745	536.6–546.2	9.6	1.56	16.3
58X	11	1005	546.2–555.9	9.7	9.92	102.0
59X	11	1316	555.9–565.6	9.7	1.14	11.7
				565.6	385.91	

previously observed in opal-rich sediments at Site 681 off Peru and were attributed to volume loss due to conversion from opal A to opal CT (Suess, von Huene, et al., 1988). Additional characteristic features of sediments in this unit are concentric purple alteration halos around burrows (Fig. 7).

Unit III (Depth: 343.3–411.1 mbsf; Age: middle Miocene)

Section 117-722B-36X-CC, 45 cm, to Section 117-722B-43X, CC, 20 cm.

Lithologic Unit III consists of alternating light and dark beds of nannofossil chalks, foraminifer-bearing nannofossil chalks, and marly nannofossil chalks. Bioturbation is minor to moderate throughout the unit. The bed thickness ranges from 0.05 to 1.00 m. Light beds dominate and range in color from white (5Y 8/1, 2.5Y 8/1, N8/) to light gray (5Y 7/1, N7/), light greenish gray (10Y 7/1, 6/1, 6/2, 5G 7/1, 5BG 7/1), light olive gray (5Y 6/2), and gray (5Y 5/1, 6/1). Darker layers are olive gray (5Y 5/2, 4/2). The calcium carbonate content in lithologic Unit III ranges from 41% to 92% (Table 3, Fig. 5). Biogenic silica is found only in trace amounts in lithologic Unit III. Compared to lithologic Units I and II, lithologic Unit III sediments show a

sharp increase in magnetic susceptibility and bulk density and a decrease in porosity and water content (see “Paleomagnetism” and “Physical Properties” sections, this chapter). The differences in the physical properties between lithologic Units II and III account for the well-developed seismic reflector correlated to the white chalks (Cores 117-722B-41X to -43X; 382–411 mbsf) in the lower half of lithologic Unit III (see “Seismic Stratigraphy” section, this chapter).

Unit IV (Depth: 411.1–565.6 mbsf; Age: middle Miocene to early Miocene)

Section 117-722B-43X, CC, 20 cm, to Section 117-722B-59X, CC, 25 cm.

The upper 87 m of lithologic Unit IV (roughly 410–497 mbsf) consists of interbedded greenish gray (5G 6/1, 5/1) silty claystones and nannofossil/marly nannofossil chalks (Fig. 8). The silty claystones contain millimeter- to centimeter-scale parallel laminae, have sharp basal contacts, and fine upward into the nannofossil chalks, forming repeated fine-grained turbidite sequences (20–50 cm thick) capped by gray and olive gray bioturbated nannofossil chalks. The silty clay intervals occasionally

Table 2. Lithologic summary, for Site 722.

	Lithologic unit	Depth (mbsf)	Cores	Age	CaCO ₃ (̄ %)
I	Foraminifer-bearing nannofossil ooze and nannofossil and marly nannofossil ooze/chalk; alternating light and dark beds	0.0-221.5 0.0-221.5	722A-1H to -23X-CC, 2 cm 722B-1H to -24X-1, 72 cm	Holocene- late Miocene	70
II	Foraminifer-bearing nannofossil, nannofossil, diatomaceous-nannofossil, radiolarian-bearing diatomaceous nannofossil, and diatomaceous-marly nannofossil chalks; alternating light and dark beds	221.5-280.0 221.5-343.4	722A-23X-CC, 2 cm to -29X-CC, 12 cm 722B-24X-1, 72 cm to -36X-CC, 45 cm	late Miocene- middle Miocene	51
III	Nannofossil, foraminifer-bearing nannofossil, and marly nannofossil chalks	343.4-411.1	722B-36X-1, 45 cm to -43X-CC, 20 cm	middle Miocene	64
IV	Interbedded fine-grained turbidites and marly nannofossil chalk	411.1-565.6	722B-43X-CC, 20 cm to -59X-CC, 25 cm	middle Miocene- early Miocene	12

contain millimeter- to centimeter-scale charcoal-rich bands (Fig. 8, 84-85 cm), pyrite-rich bands, and biogenic carbonate turbidites. The nannofossil chalks and marly nannofossil chalks range in color from light gray (5Y 7/1, 10YR 7/2) to gray (5Y 6/1), greenish gray (5Y 5/1), olive gray (5Y 5/2, 4/3, 4/2), olive (5Y 6/2), yellowish brown (10YR 5/4), light brownish gray (10YR 6/2), pale brown (10YR 6/3), brown (10YR 5/3), and dark grayish brown (10YR 4/3). Smear slide analysis indicates little compositional difference between the nannofossil chalks found in lithologic Units I and III and those found in lithologic Unit IV. However, the nannofossil chalks found in lithologic Unit IV contain darker beds and are low in calcium carbonate content (Table 3, Fig. 5). No nannofossil chalks were recovered below Core 117-722B-52X (497.9 mbsf). Recovery was very poor (22%) below 497.9 mbsf; sediments recovered below this depth consist of micaceous sands, sandstones, and silty claystones which appear to be interbedded and fine upward into claystones (Core 117-722B-59X).

The basal turbidite layers of lithologic Unit IV coarsen from silty clay (Core 117-722B-44X) to clayey sand (Core 117-722B-52X), while the upper nannofossil chalks are replaced by silty clays (Cores 117-722B-53X to -58X) and clays (Cores 117-722B-58X to -59X) downhole. Based on our limited recovery, the overall trend for lithologic Unit IV is a downsection coarsening of basal layers and fining of upper layers within individual turbidites.

Discussion

The basal (coarsest) layers of the early to middle Miocene turbidite sequences (Unit IV) fine upsection from micaceous sands to silty clays, reflecting the early Miocene tectonic uplift of the Owen Ridge (Whitmarsh, 1974). This change may have occurred as the uplift of the Owen Ridge moved Site 722 above the level of turbidite bed-load (sand) deposition, allowing only the suspended portions of turbidity flows to reach the site. The upper layers of the turbidites, however, coarsen upsection from clay to silty clay through the early Miocene.

The coarsening-upward trend of the fine-grained turbidite tops requires either a coarsening of the suspended load of the individual turbidity flows or a change in the turbidite source during the early Miocene, possibly coincident with initial stages of Owen Ridge uplift. The two most likely terrigenous turbidite sources for Site 722 during the early Miocene were the Oman margin and the Indus Fan. The extent to which each actively supplied sediment to Site 722 was influenced by the history of glacio-eustatic sea-level fluctuations, the uplift history of the

Owen Ridge, and, in the case of the Indus Fan, the history of channel migrations. Initial X-ray diffraction (XRD) investigations indicate that the Indus Fan is more likely to be the primary source of turbidite sediment throughout most of Unit IV (see "Inorganic Geochemistry" section, this chapter). During the late early Miocene, the Owen Ridge was uplifted above the realm of turbidite deposition, and the initiation of pelagic dominated sedimentation began.

By the middle Miocene, deposition at Site 722 consisted entirely of pelagic nannofossil ooze/chalk (lithologic Units I-III, 0-411.1 mbsf). With the cessation of turbidite deposition at Site 722, the major control on sedimentation became the relative production and preservation of biogenic calcium carbonate and silica, and the supply of terrigenous eolian sediment (Kolla et al., 1981) from the surrounding landmasses. The relative input of these sedimentary components has varied both on tectonic time scales (millions of years) and on orbital and climatic time scales (Milankovitch frequencies and glacial-interglacial cycles).

The shift from turbidite sedimentation to pelagic sedimentation is thought to be a tectonically controlled change at Site 722 (Whitmarsh, 1974), while Milankovitch cyclicity (climatically controlled sedimentation variations) in Owen Ridge sediments has been documented in Pleistocene high-resolution pollen and planktonic foraminifer (*G. bulloides*) records. These pollen and foraminifer records, which are used as proxy monsoon-strength indicators, are highly correlated with the 22-k.y. precession periodicity (Prell and Van Campo, 1986). Preliminary low-resolution carbonate records and high-resolution magnetic susceptibility records from Site 722 indicate that these types of cyclicities may extend into the Tertiary (see Fig. 5 and "Paleomagnetism" section, this chapter). Thus, Site 722 sediments contain long-term signals (tectonic uplift) upon which higher frequency signals (Milankovitch cyclicities) are superimposed. Detailed resolution and interpretation of these signals and evaluation of the forcing mechanisms to which they respond await shore-based investigation.

BIOSTRATIGRAPHY

Introduction

Planktonic and benthic foraminifers, nannofossils, and radiolarians in the cored sediments at Site 722 have been analyzed in order to evaluate the effects of upwelling on sediments deposited on the Owen Ridge.

Biostratigraphic analysis of planktonic foraminifers, nannofossils, and radiolarians in the sediments of Site 722 show that

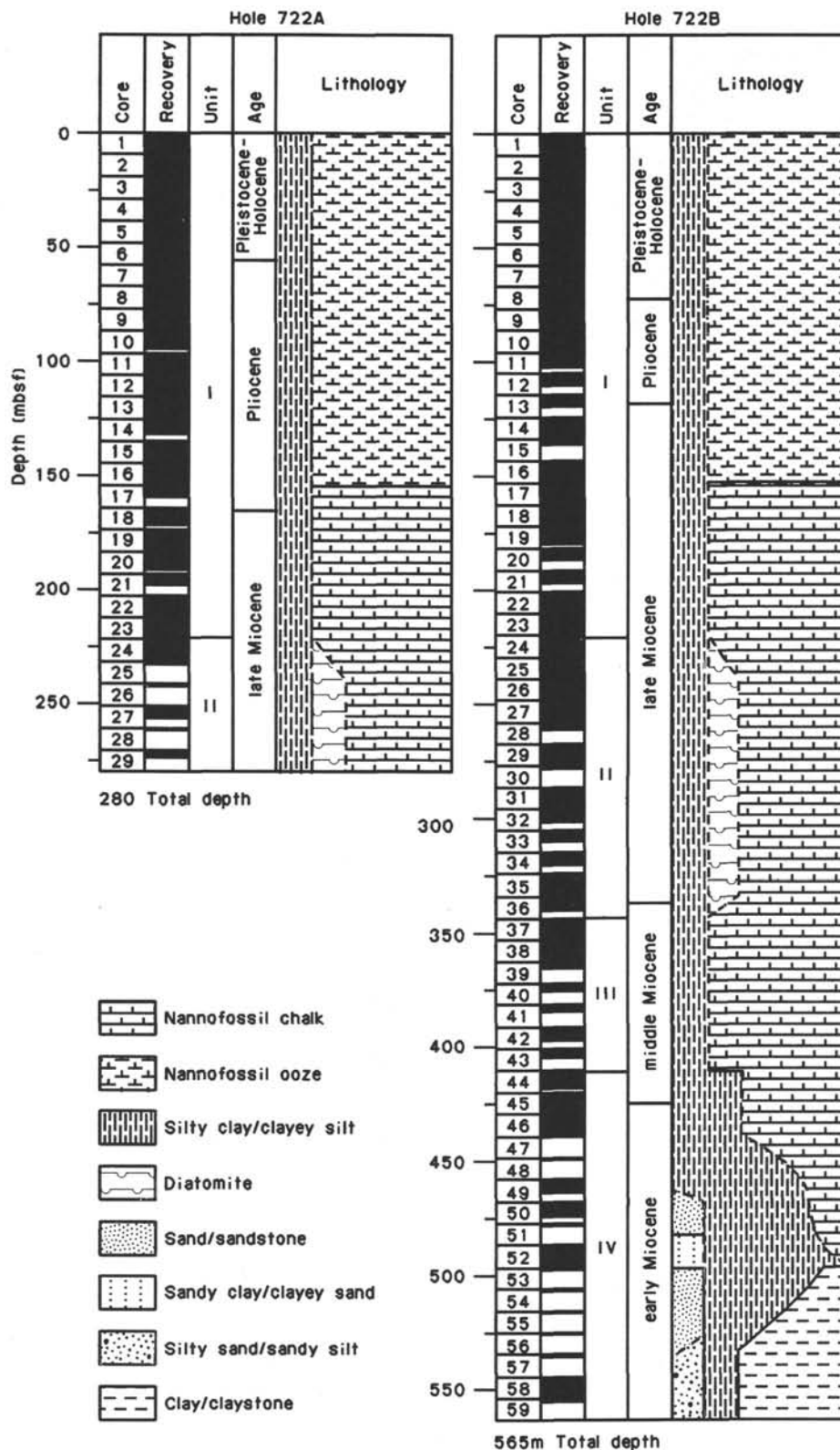


Figure 3. Lithologic summary, Site 722. Lithology is inferred between recovered intervals.

there has been more or less continuous sedimentation from early Miocene through Pleistocene (see Figs. 9 and 10). The Pliocene/Pleistocene boundary was recognized at approximately 55 mbsf. Nannofossils indicate that there is a hiatus between the uppermost Miocene and lowermost Pliocene. A plot of faunal datum

levels and paleomagnetic reversals vs. sub-bottom depth is presented in Figure 11; for a detailed listing of these data points see Table 4.

Planktonic foraminifers are abundant, highly diverse, and well preserved in Hole 722A and in the upper part of Hole

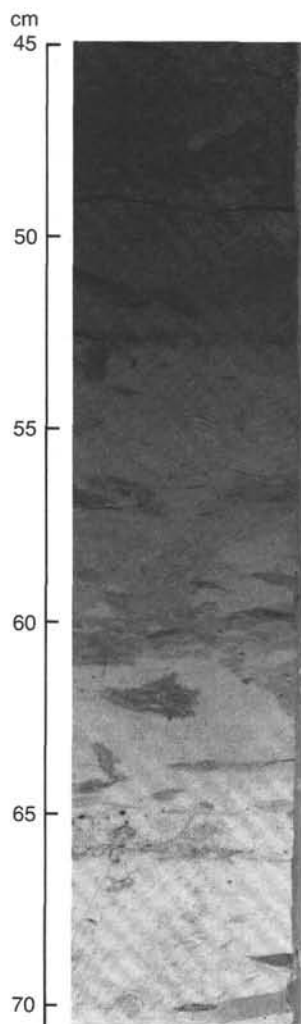


Figure 4. Burrow structures at the boundary between light and dark layers characteristic of sediments in Unit I (Section 117-722B-34X-3, 45–70 cm).

722B, down to about 230 mbsf (lithologic Units I and the upper part of II). Below 230 mbsf, the planktonic foraminiferal fauna is sparse and poorly preserved.

Radiolarians are abundant, robust, and well preserved down to about 360 mbsf, but are absent downhole from 360 mbsf.

The benthic foraminiferal fauna is diverse and well preserved, especially in the upper 77 m. The number of benthic species, as well as the total number of specimens and the state of preservation deteriorates downhole. Further downhole, the benthic foraminifera show signs of pyritization and occasionally are recrystallized. The lowest part of the hole, below 425 mbsf, is barren.

The calcareous nannofossil flora is characterized by its low diversity, especially in the upper 200 m. Below 200 mbsf, the preservation improves and the abundance increases. However, the preservation of the nannofossils below 411.1 mbsf is generally poor; asteroliths and sphenoliths are overgrown and coccoliths show dissolution.

Planktonic Foraminifers

Planktonic foraminifer faunas were analyzed in all core catchers of Hole 722A and Samples 117-722B-30X, CC, to 117-722B-59X, CC (285.5–565.5 mbsf), of Hole 722B.

Lithologic Unit I (see “Lithostratigraphy” section, this chapter) ranges from Pleistocene to upper Miocene, indicated by the

presence of foraminiferal Zones N23 through the upper part of Zone N16. This unit, a foraminifer-bearing nannofossil ooze, contains highly diverse and well-preserved foraminiferal assemblages. The top part of this unit comprises Quaternary sediments marked by sparse *Globorotalia truncatulinoides* and *Globigerinella calida calida* specimens. The N23/N22 zonal boundary lies between Samples 117-722A-2H, CC, and 117-722A-3H, CC (19.4–29.0 mbsf). Below this level *Globorotalia truncatulinoides* disappears rapidly and is absent in Sample 117-722A-5H, CC (48.2 mbsf), which makes the position of the Pliocene/Pleistocene boundary difficult to determine. The last appearance of *Globigerinoides obliquus* has been used to approximate this boundary, which occurs between Samples 117-722A-6H, CC, and 117-722A-7H, CC (57.5–67.2 mbsf). The virtual absence of *Globorotalia tosaensis* in the upper Pliocene sequence hampers the recognition of Zone N21. The upper boundary of Zone N18 has tentatively been placed between Samples 117-722A-15X, CC, and 117-722A-16X, CC (144.6–154.3 mbsf), based on the first occurrence of *Sphaeroidinella dehiscens*. The Miocene/Pliocene boundary was noted between Samples 117-722A-17X, CC, and 117-722A-18X, CC (163.9–173.6 mbsf), as the robust, relatively large *Globorotalia tumida tumida* specimens disappear below this level.

Below Sample 117-722A-24X, CC (231.7 mbsf) the sediments are composed of partly opal-rich nannofossil chalks of lithologic Unit II, in which planktonic foraminifers occur rarely. The preservation remains moderate to good. The lower part of Zone N16 through Zone N13 could be recognized, which indicates a middle to late Miocene age for the entire unit. The zonal boundary N15/N16 was found in Sample 117-722A-30X, CC (285.3 mbsf) as defined by the first appearance of *Globorotalia acostensis*. The basal part of Unit II is referred to Zones N13 to N14 on the basis of *Globorotalia mayeri* specimens.

Lithologic Unit III is nannofossil chalks with rare occurrences of planktonic foraminifers; the preservation of the tests is poor. Zones N9 to N13 of middle Miocene age are present, and the evolutionary series of *Globorotalia foysi* subspecies can be recognized. The co-occurrence of *Globorotalia peripheronda* and *Globorotalia peripheroacuta* indicates the presence of Zones N10 to N11 in Samples 117-722B-40X, CC, and 117-722B-41X, CC (382.2–391.8 mbsf). The basal part of lithological Unit III is referred to Zone N9 as supported by the presence of *Globorotalia peripheronda* and *Globorotalia birnageae* in Sample 117-722B-42X, CC (401.4 mbsf).

Lithologic Unit IV comprises a turbidite sequence, and no planktonic foraminifers could be found in the core-catcher samples from this interval. An additional Sample (117-722B-58X-5, 6–8 cm; 552 mbsf), derived from a carbonate-rich layer between two turbidites, contained some crushed specimens of *Catapsydrax dissimilis* and the *Globorotalia kugleri/peripheronda* series (Zones N4–5). The basal part of the drilled turbidite sequence is therefore earliest Miocene in age.

Benthic Foraminifers

The benthic foraminiferal fauna was studied at Site 722 in the core-catcher samples of Hole 722A down to 280.0 mbsf (117-722A-1H, CC, through -29X, CC) and in the core-catcher samples of Hole 722B for the depths below 265.9 mbsf (117-722B-28X, CC, through -59X, CC).

The abundance ranges from abundant to common in the uppermost interval (down to 202.7 mbsf in Hole 722A). The interval from 212.4 mbsf to 280.0 mbsf of Hole 722A and 265.9 mbsf to 285.3 mbsf of Hole 722B contains few benthic foraminifers, as does the interval down to 420.8 mbsf. The interval below 430.5 mbsf down to 565.6 mbsf is essentially barren. The diversity is high in the upper part of the recovered sequence and deteriorates downhole and becomes very poor below 430.5 mbsf.

This stepwise decrease in the abundance of benthic foraminifers corresponds well in both the total number and the timing to data from Site 721 (see "Biostratigraphy" section, Site 721 chapter).

The state of preservation is very good throughout the studied sequence, although a fair portion of the benthic foraminiferal population, as well as of the planktonic foraminifer population, has been pyritized. This pyritization seems to be most prominent below Sample 117-722A-24X, CC (231.7 mbsf), at the approximate level where the sedimentation changes from a siliceous nannofossil-bearing ooze (lithologic Unit II) to a foraminifer-bearing nannofossil ooze (lithologic Unit I). It becomes more distinct below this level. In some of the samples a distinct calcitic recrystallization can be recognized. Samples 117-722A-28X, CC (270.4 mbsf), 117-722B-41X, CC (391.8 mbsf), and 117-722B-42X, CC (401.4 mbsf) are strongly affected by recrystallization. The tests of planktonic foraminifers outnumber the tests of benthic foraminiferal species in most samples. However, in samples below Sample 117-722B-42X, CC (401.4 mbsf), that yielded benthic foraminifers, planktonic foraminifers had a very low percentage or were totally absent. This can be explained by selective preservation where the tests of planktonic foraminifers dissolves more easily than benthic foraminiferal tests.

Several species occur with varying relative abundance throughout the sequence studied. The most abundant are *Astrononion novozealandicum*, *Globocassidulina subglobosa*, *Epistominella exigua*, *Oridorsalis umbonatus*, *Pullenia bulloides*, and the arenaceous species *Eggerella bradyi*; minor species are *Melonis barleeianum* and *Pullenia subcarinata*. These abundant species are essentially the same as in Site 721. Occurrence of other species are restricted to certain intervals. *Bulimina aculeata* and *Chilostomella oolina* are only present in Samples 117-722A-1H, CC, through 117-722A-5H, CC (9.8–48.2 mbsf); the former has a known stratigraphic range from upper Miocene (N16) through Pleistocene (N23). *Bulimina exilis*, which has an stratigraphic range from lower Pliocene (N19) through Pleistocene (N23), is only found in three samples within the upper Pliocene (N21), i.e., Samples 117-722A-7H, CC, 117-722A-8H, CC, and 117-722A-9H, CC (67.2–86.5 mbsf). Tests of *Melonis pompilioides* are numerous below Sample 117-722A-16X, CC (154.3 mbsf), whereas they occur only sporadically above this level. The final peak in the relative abundance of *M. pompilioides* is concomitant with a peak in the relative abundance in *Ehrenbergina trigona* and slightly predates the appearance of *Cassidulina carinata*. The changes in *M. pompilioides* and *E. trigona* are coeval at Site 721 and Site 722.

The species *Uvigerina auerberiana* appears for the first time in Sample 117-722B-31X, CC (295.0 mbsf), *Uvigerina peregrina* appears slightly above. They both occur throughout the sequence of Hole 722B and throughout all of Hole 722A. The order as well as the timing of these two occurrences corresponds well to the data from Site 721.

Species restricted to the lower part of the sequence are *Ehrenbergina hystrix*, *Anomalinoidea semicribratus*, and *Globocassidulina decorata* with their last appearances encountered in Samples 117-722A-29X, CC, (280.0 mbsf), 117-722B-39X, CC (372.5 mbsf), and 117-722B-44X, CC (420.8 mbsf), respectively. The timing of these occurrences again agrees well with the data from Site 721. Species of the genera *Globobulimina* and *Nonionella* occur in Sample 117-722B-50X, CC (478.6 mbsf), from within the turbiditic sequence of lithologic Unit IV and they account for about 60% of the benthic foraminiferal fauna in that sample. These two species were not recognized at Site 721.

Not surprisingly, the benthic foraminiferal fauna of Site 722 is very similar to that of nearby Site 721. The interval missing at Site 721 is present at Site 722 and in some instances first and last appearances of some species at the approximate level of Sample

117-721B-33X, CC (318.0 mbsf), turned out to be caused by the interrupted sedimentary sequence when compared to the complete section at Site 722.

Calcareous Nannofossils

Nannofossil floras at Site 722 are similar to those observed at Site 721. At this site Holocene, Pleistocene, Pliocene, and Miocene sediments could be identified by calcareous nannofossil stratigraphy (Zones NN21–NN3), and all samples from lithologic Units I and II are characterized by fairly abundant calcareous nannofossils. Lithologic Unit I was found to range from NN21 to NN11, and the Pliocene/Pleistocene boundary was recognized in this unit. The species diversity, however, is comparatively low, especially in Quaternary and Pliocene sediments from the upper part of lithologic Unit I. The upper part of lithologic Unit III, a nannofossil chalk, has moderate to good preservation, while the lower part is poorly preserved. In general, nannofossils are abundant throughout Unit III. In samples from lower Miocene lithologic Unit IV, the abundance of calcareous nannofossil ranges from barren to abundant and the state of the preservation is generally poor.

Quaternary

Samples 117-722A-1H-4, 115–117 cm (5.65 mbsf), and 117-722B-1H, CC (5.5 mbsf), are assigned to Zone NN21. Because *Emiliania huxleyi* and *Pseudoemiliania lacunosa* are absent in Sample 117-722A-1H-5, 115–117 cm, through 117-722A-2H-5, 115–117 cm, (7.15–16.95 mbsf) 117-722B-2H, CC (15.1 mbsf), and 117-72B-3H, CC (24.7 mbsf), the samples are assigned to the Pleistocene Zone NN20. The presence of *P. lacunosa* and the absence of discoasters place Samples 117-722A-2H-6, 115–177 cm, through 117-722A-7H-4, 114–116 cm (18.46–63.14 mbsf), and 117-722B-4H, CC, through 117-722B-7H, CC (34.3–62.9 mbsf), in Zone NN19, where the following calcareous nannofossil datums are recognized in Hole 117-722B:

Top of acme of <i>Reticulofenestra</i> sp. A	0.83 Ma
117-722B-4H, CC (34.3 mbsf)/117-722B-5H, CC (43.9 mbsf)	
FAD <i>Gephyrocapsa parallela</i>	0.89 Ma
117-722B-4H, CC (34.3 mbsf)/117-722B-5H, CC (43.9 mbsf)	
LAD <i>Helicosphaera sellii</i>	1.19 Ma
117-722B-5H, CC (43.9 mbsf)/117-722B-6H, CC (53.2 mbsf)	
FAD <i>Gephyrocapsa oceanica</i>	1.57 Ma
117-722B-6H, CC (53.2 mbsf)/117-722B-7H, CC (62.9 mbsf)	
FAD <i>Gephyrocapsa caribbeanica</i>	1.66 Ma
117-722B-7H, CC (62.9 mbsf)/117-722B-8H, CC (72.5 mbsf)	

Neogene

The Pliocene/Pleistocene boundary was recognized between Samples 117-722A-6H-4, 115–117 cm (53.85 mbsf), and 117-722A-6H-5, 115–117 cm (55.35 mbsf), in Hole 722A and 117-722B-7H, CC (62.9 mbsf), and 117-722B-8H, CC (72.5 mbsf), in Hole 722B. The presence of *Discoaster brouweri* in Samples 117-722A-7H-5, 115–117 cm (64.65 mbsf), and 117-722B-8H, CC (72.5 mbsf), assigns them to Zone NN18. Samples 117-722A-8H-6, 115–117 cm, through 117-722A-11X, CC (75.85–105.61 mbsf), and 117-722B-9H, CC, through 117-722B-12X, CC (82.2–111.20 mbsf), contain *Discoaster pentaradiatus* but lack *D. surculus* and are assigned to the middle upper Pliocene (Zone NN17 to NN16). As at Site 721, *D. surculus* is not present in the uppermost part of its known range.

Ceratoliths are rare and amauroliths are absent at this site as they were at Site 721. The first samples with *R. pseudoumbilica* are 117-722A-12X-1, 116–118 cm (107.06 mbsf), and 117-722B-13X, CC (120.9 mbsf). These have been assigned to Zone NN15 because they occur below the samples of Zone NN16. Without *Amaurolithus tricorniculatus* and *Discoaster asymmetricus*, how-

Table 3. Calcium carbonate and organic carbon contents, Site 722.

Hole, core, section, interval (cm)	Depth (mbsf)	Total carbon (%)	Inorganic carbon (%)	Organic carbon (%)	CaCO ₃ (%)
722A-1H-2, 52-54	2.02		8.29		69.1
722A-1H-4, 52-54	5.02		6.72		56.0
722A-1H-4, 144-145	5.94	7.93	7.58	0.35	63.1
722A-1H-6, 52-54	8.02		8.57		71.4
722A-2H-2, 50-52	11.80		9.43		78.6
722A-2H-4, 50-52	14.80		9.16		76.3
722A-2H-6, 50-52	17.80		7.95		66.2
722B-3H-3, 51-53	18.61	9.04	8.17	0.87	68.1
722A-3H-2, 50-52	21.40		9.01		75.1
722A-3H-4, 50-52	24.40		9.27		77.2
722A-3H-4, 114-115	25.04	9.22	8.39	0.83	69.9
722A-3H-6, 50-52	27.40		8.73		72.7
722A-4H-2, 50-52	31.00		7.23		60.2
722A-4H-4, 50-52	34.00		7.77		64.7
722A-4H-6, 50-52	37.00		8.33		69.4
722A-5H-2, 50-52	40.60		8.09		67.4
722A-5H-4, 50-52	43.60		6.92		57.6
722A-5H-6, 50-52	46.60		9.21		76.7
722A-6H-2, 50-52	50.20		7.35		61.2
722A-6H-4, 50-52	53.20		7.46		62.1
722A-6H-4, 114-115	53.84	7.89	6.76	1.13	56.3
722A-6H-6, 50-52	56.20		6.69		55.7
722A-7H-2, 50-52	59.50		7.02		58.5
722A-7H-4, 50-52	62.50		6.14		51.2
722A-7H-6, 50-52	65.50		8.59		71.6
722A-8H-2, 50-52	69.20		9.15		76.2
722A-8H-4, 50-52	72.20		8.01		66.7
722A-8H-6, 50-52	75.20		7.56		63.0
722A-9H-2, 50-52	78.80		6.03		50.2
722A-9H-4, 50-52	81.80		7.71		64.2
722A-9H-4, 119-120	82.49	10.43	8.33	2.10	69.4
722A-9H-6, 50-52	84.80		8.25		68.7
722A-10X-2, 50-52	88.50		7.58		63.1
722A-10X-4, 50-52	91.50		8.06		67.1
722A-11X-2, 50-52	98.20		8.90		74.1
722A-11X-4, 50-52	101.20		9.26		77.1
722A-11X-6, 50-52	104.20		9.04		75.3
722A-12X-2, 49-51	107.89		9.57		79.7
722A-12X-4, 49-51	110.89		8.13		67.7
722A-12X-4, 119-120	111.59	9.81	9.40	0.41	78.3
722A-12X-6, 49-51	113.89		8.45		70.4
722A-13X-2, 50-52	117.60		10.03		83.6
722A-13X-4, 50-52	120.60		8.09		67.4
722A-13X-6, 50-52	123.60		9.40		78.3
722A-14X-2, 50-52	127.30		9.88		82.3
722A-14X-4, 52-54	130.32		8.76		73.0
722A-15X-2, 60-62	137.00		8.30		69.1
722A-15X-4, 60-62	140.00		10.40		86.6
722A-15X-5, 145-150	142.35	10.66	10.45	0.21	87.1
722A-15X-6, 15-17	142.55		6.11		50.9
722A-16X-2, 20-21	146.30	10.07	10.42	0.00	86.8
722A-16X-2, 25-26	146.35	10.53	10.09	0.44	84.1
722A-16X-2, 29-30	146.39	10.37	9.79	0.58	81.6
722A-16X-2, 34-35	146.44	10.51	9.48	1.03	79.0
722A-16X-2, 39-40	146.49	10.21	8.55	1.66	71.2
722A-16X-2, 43-44	146.53	10.47	8.53	1.94	71.1
722A-16X-2, 48-49	146.58	9.99	8.06	1.93	67.1
722A-16X-2, 52-54	146.62		7.90		65.8
722A-16X-2, 56-57	146.66	9.28	7.35	1.93	61.2
722A-16X-2, 60-61	146.70	8.79	6.85	1.94	57.1
722A-16X-2, 65-66	146.75	8.62	6.74	1.88	56.1
722A-16X-2, 69-70	146.79	8.85	6.79	2.06	56.6
722A-16X-2, 75-76	146.85	9.62	6.65	2.97	55.4
722A-16X-2, 80-81	146.90	9.26	8.14	1.12	67.8
722A-16X-2, 85-86	146.95	9.56	8.62	0.94	71.8
722A-16X-2, 90-91	147.00	10.61	10.14	0.47	84.6
722A-16X-2, 95-96	147.05	10.61	10.16	0.45	84.6
722A-16X-4, 53-55	149.63		8.07		67.2
722A-16X-6, 50-52	152.60		8.93		74.4
722A-17X-1, 108-110	155.38		10.13		84.4
722A-17X-3, 103-105	158.33		8.86		73.8
722A-18X-2, 58-60	165.98		8.39		69.9
722B-19X-1, 40-42	169.60		1.25		10.4
722A-18X-6, 58-60	170.20		10.40		86.6
722A-19X-2, 62-64	175.72		7.63		63.6
722A-19X-4, 59-61	178.69		10.45		87.1

Table 3 (continued).

Hole, core, section, interval (cm)	Depth (mbsf)	Total carbon (%)	Inorganic carbon (%)	Organic carbon (%)	CaCO ₃ (%)
722A-19X-4, 119-120	179.29	8.58	7.27	1.31	60.6
722A-20X-2, 36-38	185.16		10.54		87.8
722A-20X-4, 60-62	188.40		7.94		66
722A-21X-1, 57-59	193.57		10.29		85.7
722A-21X-3, 60-62	196.60		7.66		63.8
722A-22X-2, 52-54	204.72		10.06		83.8
722A-22X-4, 52-54	207.72		9.86		82.1
722A-22X-4, 119-120	208.39	8.28	7.68	0.60	64.0
722A-22X-4, 119-120	208.39	8.28	7.68	0.60	64.0
722A-22X-6, 52-54	210.72		8.70		72.5
722A-23X-2, 50-52	214.40		8.72		72.6
722A-23X-4, 68-70	217.58		8.53		71.1
722A-23X-6, 38-40	220.28		8.02		66.8
722A-24X-2, 17-20	223.67		8.72		72.6
722A-24X-4, 50-52	227.00		6.46		53.8
722A-24X-6, 50-52	230.00		7.61		63.4
722A-25X-1, 50-52	232.20		10.71		89.2
722A-26X-1, 58-60	242.28		7.31		60.9
722B-27X-4, 114-115	252.14	9.30	9.09	0.21	75.7
722A-27X-2, 29-31	252.79		5.11		42.6
722A-27X-2, 114-115	253.64	9.64	9.54	0.10	79.5
722A-27X-4, 17-19	255.67		2.69		22.4
722B-28X-2, 47-49	258.17		10.54		87.8
722B-29X-3, 60-63	269.50		5.34		44.5
722B-29X-3, 113-114	270.03	9.54	9.38	0.16	78.1
722B-29X-3, 120-121	270.10	8.15	7.43	0.72	61.9
722B-29X-3, 125-126	270.15	7.78	5.99	1.79	49.9
722B-29X-3, 130-131	270.20	7.60	5.37	2.23	44.7
722B-29X-3, 135-136	270.25	7.56	5.34	2.22	44.5
722B-29X-3, 140-141	270.30	7.16	4.99	2.17	41.6
722B-29X-3, 145-146	270.35	6.95	4.69	2.26	39.1
722B-29X-3, 149-150	270.39	6.89	4.66	2.23	38.8
722B-29X-4, 5-6	270.45	6.15	4.31	1.84	35.9
722B-29X-4, 10-11	270.50	5.36	3.85	1.51	32.1
722B-29X-4, 15-16	270.55	3.90	3.77	0.13	31.4
722B-29X-4, 20-21	270.60	5.39	4.29	1.10	35.7
722B-29X-4, 25-26	270.65	4.98	4.01	0.97	33.4
722B-29X-4, 30-31	270.70	5.27	4.44	0.83	37.0
722B-29X-4, 35-36	270.75	6.21	5.41	0.80	45.1
722A-29X-1, 37-40	270.77		10.17		84.7
722B-29X-4, 40-41	270.80	7.94	7.45	0.49	62.1
722B-29X-4, 47-48	270.87	9.46	8.72	0.74	72.6
722B-29X-4, 52-53	270.92	9.53	9.25	0.28	77.1
722B-29X-4, 60-61	271.00	9.03	8.76	0.27	73.0
722A-29X-3, 39-40	273.79	6.36	2.20	4.16	18.3
722B-31X-2, 50-52	287.30		6.24		52.0
722B-31X-4, 50-52	290.30		9.55		79.6
722B-31X-4, 114-115	290.94	6.62	5.71	0.91	47.6
722B-31X-6, 50-52	293.30		9.33		77.7
722B-32X-2, 50-52	297.00		8.92		74.3
722B-32X-4, 50-52	300.00		5.47		45.6
722B-33X-2, 28-30	306.48		2.95		24.6
722B-34X-2, 80-82	316.60		3.34		27.8
722B-34X-2, 114-115	316.94	5.08	3.77	1.31	31.4
722B-34X-4, 40-42	319.20		4.87		40.6
722B-35X-2, 52-54	326.02		7.97		66.4
722B-35X-4, 51-53	329.01		3.22		26.8
722B-35X-6, 50-52	332.00		6.64		55.3
722B-36X-2, 48-50	335.68		6.11		50.9
722B-36X-4, 77-79	338.97		5.18		43.2
722B-37X-2, 51-53	345.41		8.99		74.9
722B-37X-4, 51-53	348.41		6.35		52.9
722B-37X-6, 50-52	351.40		9.91		82.6
722B-38X-2, 71-73	355.31		4.97		41.4
722B-38X-4, 83-85	358.43		8.48		70.6
722B-38X-6, 52-54	361.12		5.04		42.0
722B-39X-1, 12-14	362.92		8.52		71.0
722B-40X-3, 16-18	375.66		4.48		37.3
722B-41X-2, 29-31	383.99		11.09		92.4
722B-42X-1, 22-24	392.02		10.80		90.0
722B-42X-3, 33-35	395.13		6.30		52.5
722B-43X-1, 40-42	401.80		10.74		89.5
722B-43X-2, 114-115	404.04	7.01	6.83	0.18	56.9
722B-43X-3, 23-25	404.63		6.36		53.0
722B-44X-2, 38-40	412.98		6.32		52.7
722B-44X-4, 17-19	415.77		0.76		6.3

Table 3 (continued).

Hole, core, section, interval (cm)	Depth (mbsf)	Total carbon (%)	Inorganic carbon (%)	Organic carbon (%)	CaCO ₃ (%)
722B-45X-2, 23-25	422.53		0.62		5.2
722B-45X-4, 27-29	425.57		3.00		25.0
722B-45X-6, 138-140	429.68		0.58		4.8
722B-46X-2, 1-3	432.01		1.31		10.9
722B-46X-4, 141-143	436.41		3.25		27.1
722B-46X-5, 114-115	437.64	0.89	0.78	0.11	6.5
722B-46X-6, 132-134	439.32		1.56		13.0
722B-48X-1, 33-35	450.13		1.14		9.5
722B-49X-1, 40-42	459.80		1.25		10.4
722B-49X-3, 114-115	463.54	1.76	1.49	0.27	12.4
722B-49X-4, 40-42	464.30		1.25		10.4
722B-50X-2, 39-41	470.89		1.26		10.5
722B-50X-4, 30-32	473.80		1.36		11.3
722B-51X-1, 69-71	479.29		1.42		11.8
722B-51X-CC, 0-0	479.39	41.91	0.10	41.81	0.8
722B-52X-2, 79-81	490.49		0.51		4.3
722B-52X-5, 54-56	494.74		1.17		9.8
722B-52X-7, 8-10	497.28		0.51		4.3
722B-53X-1, 41-43	498.31		1.74		14.5
722B-58X-1, 134-136	547.54		1.50		12.5
722B-58X-3, 74-76	549.94		1.28		10.7
722B-58X-4, 114-115	551.84	2.55	2.50	0.05	20.8
722B-59X-CC, 12-14	556.86		0.72		6.0

ever, we cannot be certain that this is the correct age assignment. As was the case with the above two samples, Samples down to 117-722A-17X, CC (158.63 mbsf), and 117-722B-14X, CC, through 117-722B-17X, CC (130.5-159.5 mbsf), may belong to Zone NN15-NN12. *D. quinqueramus* is present in Samples 117-722A-18X-1, 115-116 cm, through 117-722A-28X, CC (165.05-270.4 mbsf), and 117-722B-18X, CC, through 117-722B-29X, CC (169.2-275.6 mbsf). These samples generally contain a diverse assemblage of nannofossils which includes several species of discoasters. *D. berggrenii*, *D. pentaradiatus*, *D. brouweri*, *D. variabilis*, *D. pseudovariabilis*, *D. bellus*, *D. blackstockae*, *D. triradiatus*, *D. neohamatus*, *D. challengerii*, *D. loeblichii*, *D. neorectus*, *D. intercalaris*, *D. calcaris*, and *D. surculus* are found in this zone.

In Hole 722B Zone NN12 (upper Miocene to lowermost Pliocene) appears to be missing and the discontinuity is assumed between Samples 117-722B-17X, CC (159.5 mbsf), and 117-722B-18X, CC (169.2 mbsf). The same discontinuity may be present in Hole 722A but the lack of marker species in cores of the equivalent ages precludes the definite recognition of missing sediments. Because Samples 117-722A-29X-1, 114-116 cm (271.54 mbsf), the deepest sample from the bottom of Hole 722A, and 117-722B-30X, CC, through 117-722B-32X, CC (285.3-304.7 mbsf), contain neither *D. quinqueramus* nor *D. hamatus*, they are assigned to Zone NN10 (middle upper Miocene). *D. hamatus* is found in Samples 117-722B-33X-1, 115-116 cm, through 117-722B-34X, CC (305.85-324.0 mbsf), so that a zonal assignment of NN9 is given. *Catinaster coalitus* is not found in samples of this site and only the presence of *Discoaster kugleri* identifies Samples 117-722B-35X, CC, through 117-722B-40X-2, 110-111 cm (333.55-375.10 mbsf), as belonging to Zones NN8-NN7 (middle Miocene). Samples 117-722B-40X, CC (382.2 mbsf), through 117-722B-41X-1, 21-22 cm (382.41 mbsf), contains neither *D. kugleri* nor *Sphenolithus heteromorphus* and can be assigned to Zone NN6. *S. heteromorphus* is present in Samples 117-722B-41X, CC, through 117-722B-43X, CC (391.8-411.1 mbsf), that this interval has been included in NN4-NN5. The presence of *Helicosphaera ampliaptera* is used to divide Zones NN4 from NN5, but unfortunately *H. ampliaptera* is missing from the sediments of this site as was the case at Site 721.

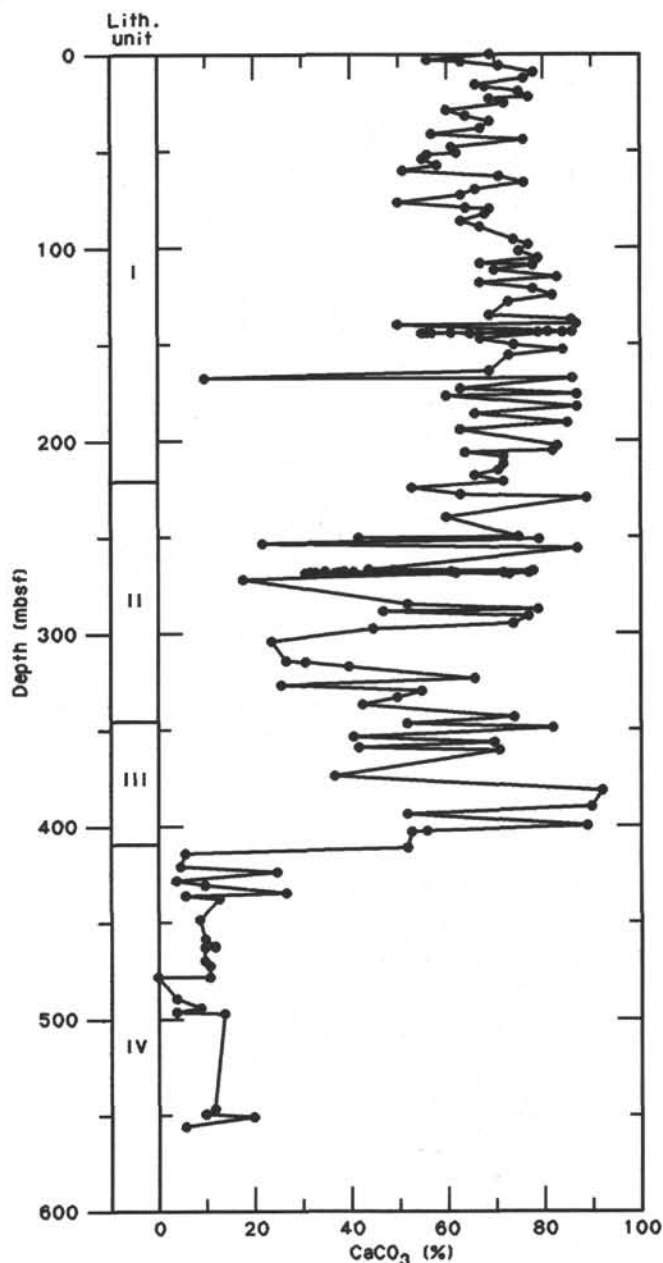


Figure 5. Calcium carbonate profile at Site 722. Samples from 0 to 255 mbsf are from Hole 722A and samples from 255 to 556 mbsf are from Hole 722B.

The preservation of nannofossils becomes poor in Sample 117-722B-42X, CC (401.4 mbsf), and remains poor to the bottom of the hole. Asteroliths and sphenoliths are heavily overgrown and the coccoliths have undergone varying degrees of dissolution. As a result, the biostratigraphy of this part of the hole is dubious. Samples 117-722B-49X, CC, through 117-722B-51X, CC (469.0-488.2 mbsf), are barren or have such small quantities of nannofossils that they should be considered barren. Samples 117-722B-53X, CC, through 117-722B-57X, CC (507.6-546.2 mbsf), contain no age-diagnostic species. Sample 117-722B-58X, CC (555.9 mbsf), from turbiditic sediments of lithologic Unit IV contains a mixed flora of Miocene, Oligocene, and Eocene age. Sample 117-722B-59X, CC (565.6 mbsf), contains *S. belemnus* and *D. druggii* and was assigned to Zone NN3 (lower Miocene).

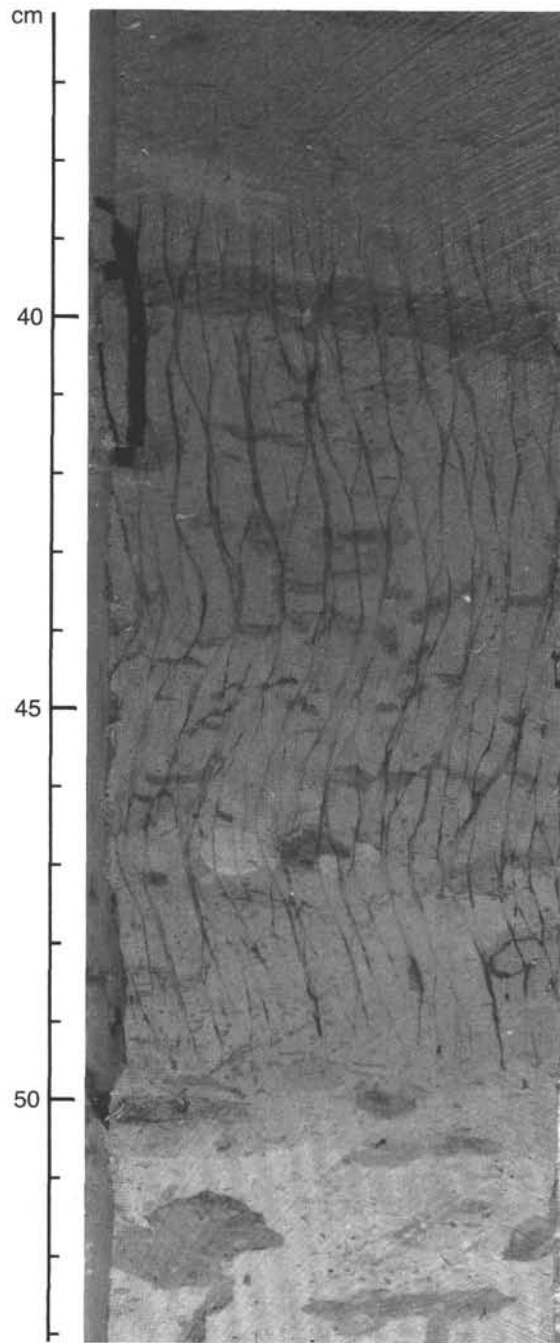


Figure 6. Subvertical, en echelon dewatering(?) structures characteristic of opal-rich sediments in Unit III (Section 117-722B-34X-1, 37–53 cm).

Radiolarians

Shipboard analysis included all core-catcher samples from Hole 722A and Samples 117-722B-28X, CC, through Sample 117-722B-38X, CC (265.9–362.8 mbsf). Intermediate samples were analyzed during subsequent shore-based studies. Radiolarians are abundant, robust, and well preserved throughout Hole 722A and in lithologic Units I and II of Hole 722B. Sample 117-722B-38X, CC (362.8 mbsf), contains few radiolarians, most of which are coated with pyrite. The remainder of Hole 722B below this sample is barren of radiolarians. Radiolarian zones from the Pleistocene to upper Miocene were identified in lithologic Unit I of Hole 722A. The uppermost Quaternary radiolarian

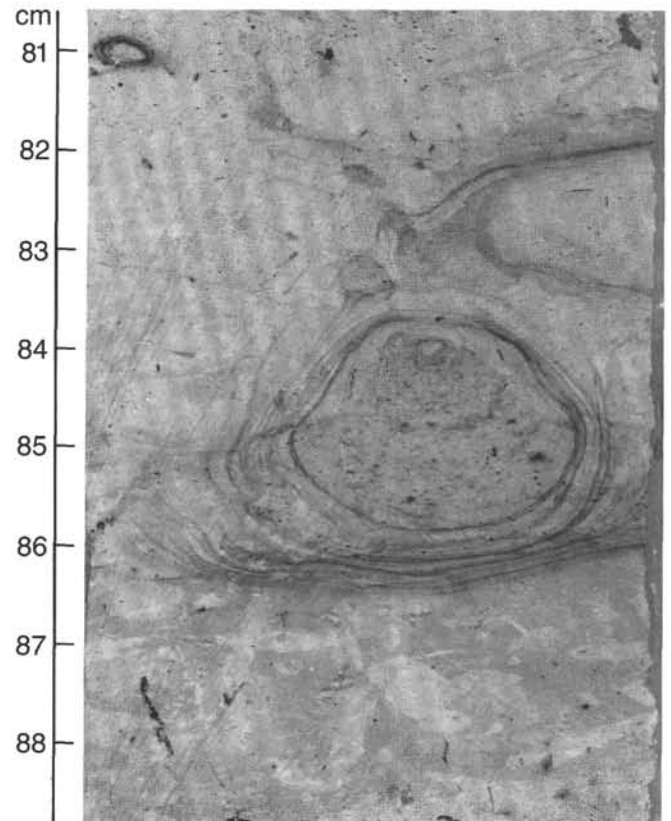


Figure 7. Concentric, purple alteration rings characteristic of sediments in Unit III (Section 117-722B-35X-5, 81–88 cm).

zone, *Buccinosphaera invaginata*, is missing and Sample 117-722A-1H, CC (9.8 mbsf), probably belongs to the *Collosphaera tuberosa* Zone. Samples 117-722A-2H-4, 85–87 cm (15.15 mbsf), through 117-722A-6H-4, 85–87 cm (43.95 mbsf), belong to the *Amphirhopalum ypsilon* Zone, while Samples 117-722A-5H, CC, through 117-722A-6H-4, 85–87 cm (48.20–53.55 mbsf), are in the *Anthocyrtidium angulare* Zone. The top of the *Pterocanium prismatium* Zone has been placed at Sample 117-722A-6H, CC (57.5 mbsf), but this is based on the presence of only two specimens of *P. prismatium*, which seems to be very rare in this part of the Indian Ocean. The zone is present through Sample 117-722A-8H, CC (76.8 mbsf). Sample 117-722A-9H, CC (86.5 mbsf), contains the last common occurrence of *Stichocorys peregrina* and marks the top of the *Spongaster pentas* Zone, although few reworked specimens were found above this level. The lower limit of the *S. pentas* Zone is impossible to locate accurately, because it is based on the evolutionary transition of *Spongaster berminghami* to *Spongaster pentas*; the latter species seems to be absent or extremely rare in this area. Therefore, the *S. pentas*/*S. peregrina* boundary has been approximated to the last occurrence of *Solenosphaera omnitubus* in Sample 117-722A-16X, CC (154.3 mbsf). The lower limit of the *S. peregrina* Zone is also difficult to determine accurately because that boundary is defined by the evolutionary transition of *Stichocorys delmontensis* to *S. peregrina* and the samples contain considerable reworking of the ancestral species, as well as various Miocene species of *Didymocyrtis* and *Diartus*. The boundary between the *S. peregrina* and *Didymocyrtis penultima* Zone has been placed, with some misgivings, between Samples 117-722A-22X, CC, and 117-722A-23X-4, 85–87 cm (212.40–217.75 mbsf). Hence, the boundary between lithologic Units I and II is located in the *D. penultima* Zone. The top of the *Didymocyrtis*

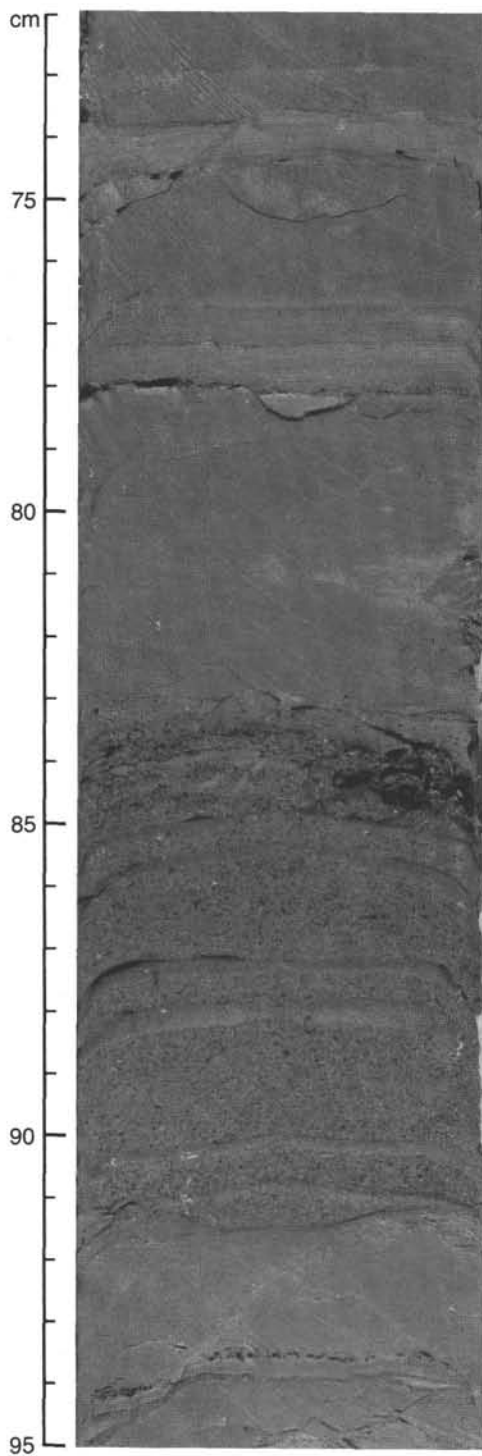


Figure 8. Silty claystone interbedded with silty clays and marly nannofossil chinks; representative of the upper 100 m of Unit IV. Note charcoal-rich bed from 84 to 85 cm. Downsection the silty claystone is replaced by micaceous sands and sandstones while the marly nannofossil chinks are replaced by silty clays (Section 117-722B-49X-2, 72-95 cm).

antepenultima Zone is defined by the last occurrence of *Diartus hughesi* in Sample 117-722A-26X, CC (251.0 mbsf), although reworking of *D. hughesi* presents some difficulties in defining the boundary. At this level diatoms also become quite common.

Analysis in Hole 722B began with Sample 117-722B-28X, CC, which was assigned to the *D. antepenultima* Zone; the zone

Core	Epoch	Calcareous nannofossils	Radiolarians	Planktonic foraminifers		
0	Holocene - Pleistocene	1H	<i>Collosphaera tuberosa</i>	N23		
2H		NN21				
3H		NN19	<i>Amphirhopalum ypsilon</i>	N22		
4H					NN20	
5H					NN18	
6H	Pliocene	NN17	<i>Anthocyrtidium angulare</i>	N18 - N21		
7H					NN16	
8H		NN15 - NN12	<i>Pterocanium prismatum</i>			
9H					NN18	
10X					NN17	
11X					NN16	
12X		Miocene	NN11		<i>Spongaster pentas</i>	
13X						NN15
14X						NN12
15X						NN11
16X	NN10					
17X	<i>Stichocorys peregrina</i>			N16 - N17		
18X						NN11
19X						NN10
20X						NN11
21X						NN10
22X	<i>Didymocyrtis penultima</i>	N16 - N17				
23X			NN11			
24X			NN10			
25X			NN11			
26X			NN10			
27X			NN11			
28X			NN10			
29X	NN10					
			<i>Didymocyrtis antepenultima</i>			

Figure 9. Correlation of planktonic microfossil zones in Hole 722A.

continues through Sample 117-722B-30X, CC (265.9-285.3 mbsf). The remainder of the section lies within the *Diartus petterssoni* Zone. However, reworking again makes it difficult to locate a boundary which is dependent upon an evolutionary sequence (*D. petterssoni* to *D. hughesi* in this case). In the lower part of Unit II and upper part of Unit III (Sample 117-722B-31X, CC, and downhole to Sample 117-722B-37X, CC (295.0-353.1 mbsf), diatoms are abundant. The siliceous fauna in Sample 117-722B-37X, CC (353.1 mbsf), of Unit III is robust and diverse. In Sample 117-722B-38X, CC (362.8 mbsf), of Unit III, however, the fauna is much reduced and more than half the radiolarians have been pyritized; diatoms are absent.

Paleoenvironmental Implications

The preservation states of the calcareous tests of planktonic foraminifers and coccoliths are thought to be related to the uplift history of Owen Ridge and variations of the CCD and lysocline. The lower part of the sequence corresponding to lithologic Unit IV contains only badly preserved coccoliths and one pelagic calcareous interval with some planktonic foraminifer remains, which indicates deposition just above the CCD. In the lower upper Miocene to lower middle Miocene (lithologic Unit III) planktonic and benthic foraminifers are rare, but coccoliths are abundant. By this time Owen Ridge had been either at least partially uplifted or the lysocline had deepened. Improvement of preservation on Owen Ridge continued during the late Miocene, as is indicated by well-developed planktonic and benthic foraminiferal faunas in the upper sediments of lithological Unit II.

The increase of opal in the lower part of lithological Unit II (upper Miocene) indicates changing environmental conditions which may be related to changes in circulation, global cooling, and/or increased upwelling intensity. This cooling period may have enhanced bottom circulation and could have been responsible for a rise in the CCD in the Indian Ocean (Kennett, 1982). However, benthic foraminiferal data do not indicate that high-latitude water masses influenced the Arabian Sea. The Carls-

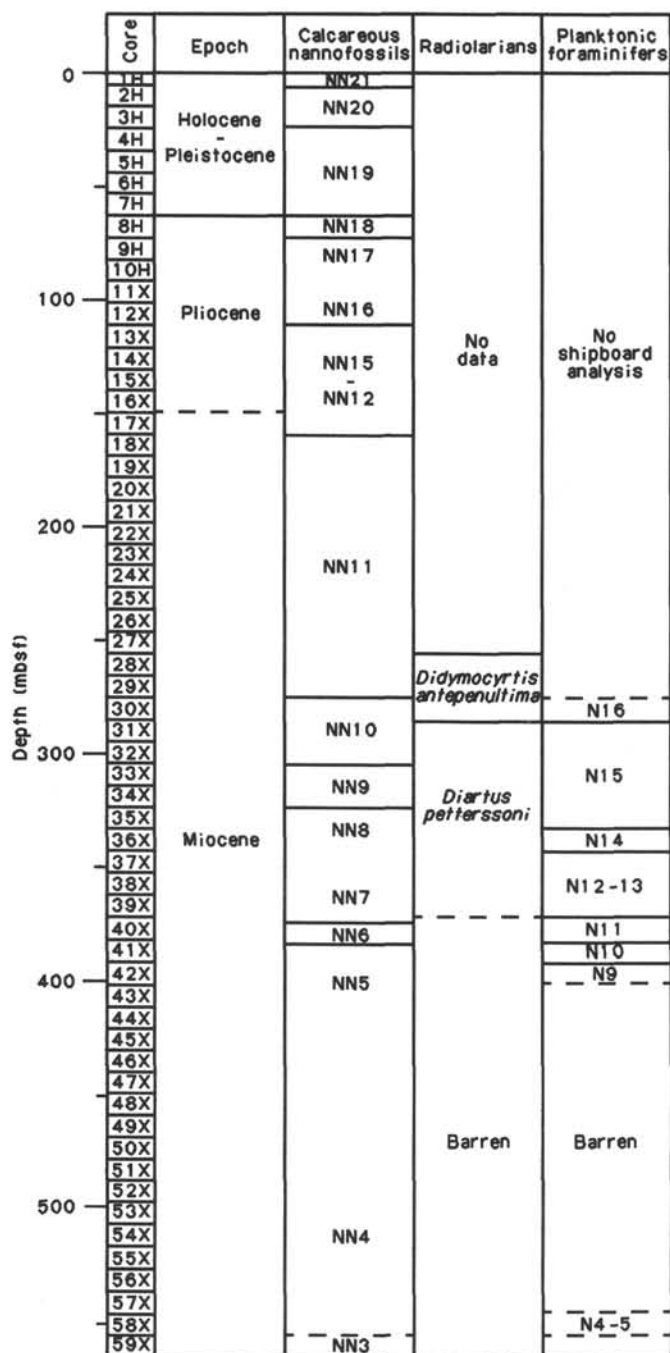


Figure 10. Correlation of planktonic microfossil zones in Hole 722B.

berg Ridge may have prevented these bottom currents from affecting this area.

PALEOMAGNETISM

Magnetic Measurements

We used the pass-through cryogenic magnetometer to measure the natural remanent magnetization (NRM) of the archive halves of Cores 117-722A-1H through 117-722A-9H, and the whole rounds and archive halves of Cores 117-722B-6H and 117-722B-7H. However, as at Sites 720 and 721, we were unable to achieve reliable results; again this appeared to be the result of a coring/core-barrel-induced remanence, together with a possible

anhysteretic remanent magnetization acquired from the pass-through alternating-field (AF) demagnetizer. Therefore, all our magnetostratigraphic results are based on measurements of discrete samples using the MINISPIN fluxgate spinner magnetometer and the Schonstedt AF demagnetizer. We measured 144 samples from Hole 722A and 150 samples from Hole 722B. Because of time constraints we did not routinely subject selected samples to stepwise alternating field demagnetization but instead demagnetized all samples at a blanket AF of either 10 or 15 mT. Our results from Site 721 (about 6 mi away from Site 722) suggested that for these sediments a field of 10–15 mT is sufficient to isolate the characteristic magnetization of most of the samples. More detailed shore-based demagnetization studies revealed that some samples change their magnetic polarity between 10 mT and 15 mT AF cleaning.

Figure 12 shows the discrete sample NRM results after AF demagnetization for the combined data from Holes 722A and 722B. The geometric mean intensity is very low: 0.13 mA/m. The circular standard deviation (CSD) is a measure of the reliability of each measurement, with higher values indicating decreasing reliability. In the nannofossil oozes and chalks of lithologic Units I to III (see "Lithostratigraphy" section, this chapter) the intensities after AF demagnetization are very weak (almost always less than 0.2 mA/m); higher values (up to about 20 mA/m) occur in lithologic Unit IV (predominantly silty claystones), beginning at 411.1 mbsf in Hole 722B. This pattern is paralleled in the magnetic susceptibility record (see discussion below), showing that the NRM intensity is controlled primarily by the concentration of magnetic minerals. A clear inverse relationship exists between the reliability of the measurements, as expressed by the CSD, and the NRM intensity.

Magnetostratigraphy

Figure 13 shows a histogram of the inclination values grouped into 10° classes; the arrows show the expected geocentric axial dipole inclination value (30.6°) for this latitude. Despite the low NRM intensities, the correspondence between the observed and expected inclination values is acceptable, which gives us some confidence in our magnetostratigraphic interpretations of a somewhat noisy data set.

We determined magnetic polarity zone boundaries of Holes 722A and 722B, based on inclination values of samples with CSD values of less than 40 together with results of shore-based measurements after 15 mT AF demagnetization. The depth within core and section of the reversal boundaries are given in Table 5. As at Site 721 the Chron C1/C1r (Brunhes/Matuyama Chronozone) boundary is absent or poorly defined (although it is indicated by a shallowing of inclination values between 30 and 40 mbsf), and we interpret the first clear normal to reversed transition at about 40 mbsf as the boundary between Subchron C1r-1 (Jaramillo Subchronozone) and Chron C1r (Matuyama Chronozone). As at Site 721, Chron C2 (Olduvai Subchronozone) cannot be identified. We place the upper and lower boundaries of Chron C2A (Gauss Chronozone) at about 85 mbsf and about 105 mbsf respectively, and the lower boundary of Chron C3.3 (Thvera) at about 150–155 mbsf. These assignments are in good agreement with biostratigraphic evidence (see "Biostratigraphy" section, this chapter). We place the upper boundary of Chron C3A (Chronozone 5) at about 180–185 mbsf. Because of the relatively small number of stable samples over this interval we are less confident in recognizing the lower boundary of Chron C3A (Chronozone 5), but place it at about 220 mbsf. Again, this agrees with biostratigraphic evidence.

The character of the polarity transitions at this site is of interest: as at Site 721 the interval of reattainment of the expected geocentric axial dipole inclination values across a transition ex-

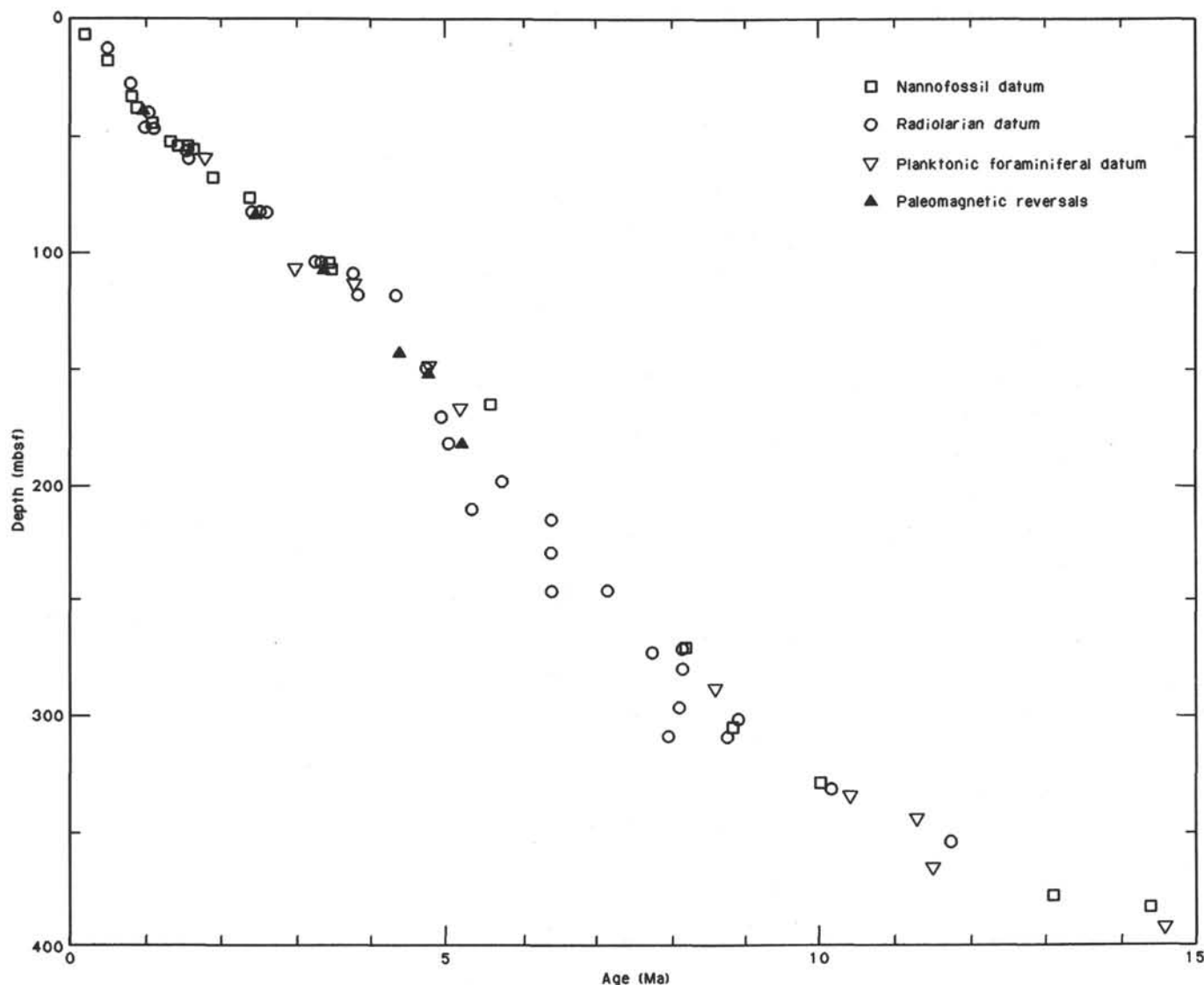


Figure 11. Age-depth plot for Site 722. For a detailed listing of the events see Table 4.

tends over several meters. With an average sediment accumulation rate of about 3 cm/k.y. at this site this represents a much longer period of time than the duration of an average polarity transition (about 5 k.y.). This suggests that the time required for the geomagnetic signal to be "locked in" is much longer than appears to be the case for some other deep-sea sediments. This inference is compatible with the apparent inability of the sediment sequences at Sites 721 and 722 to record polarity intervals of relatively short duration, such as the interval between the base of Chron C1 (Brunhes Chronozone) and the upper boundary of Subchron C1r-1 (Jaramillo Subchronozone), and Chron C2 (Olduvai Subchronozone). Intense bioturbation is a possible explanation; however, this would have to operate over a depth range of several meters to achieve the required effect, which seems unlikely. Moreover, the occurrence of susceptibility variations on a depth scale of 1 m and less (see discussion below) argues against bioturbation being the cause. Another possibility is that the NRM is of chemical origin, perhaps carried by authigenic ferrimagnetic iron sulfides, which could require relatively long intervals to form. Such an explanation is compatible with the highly reduced state of the sediments. Shore-based rock-magnetic and X-ray diffraction studies of magnetic concentrates could provide a way of testing this second possibility. At present both explanations are entirely speculative.

Core Orientation

Table 6 compares the orientation of Cores 117-722A-5H through -7H and Cores 117-722B-6H and -8H through -10H as estimated from the multishot device with the orientation as estimated from the measured average declination values of discrete samples from the cores. As at Site 721, there is complete disagreement between the two methods, which raises further doubt about the reliability of the multishot estimates.

Magnetic Susceptibility

The volume magnetic susceptibility of whole sections of Holes 722A and 722B was measured using the Bartington M.S. 1 whole-core sensor at the 0.1 sensitivity and low-frequency (0.47-kHz) settings. All cores from Hole 722A and Cores 117-722B-1H to -11X were measured at 5-cm intervals; Cores 117-722B-12X to -58X were measured at 10-cm intervals to speed up core processing. A total of 3914 and 4368 measurements were made for Holes 722A and 722B, respectively.

The susceptibility data from Hole 722A were very similar in character to those obtained from Site 721, which was located ~6 mi to the southwest (Fig. 14; see "Paleomagnetism" section, "Site 721" chapter, this volume). As with the Site 721 sediments, the susceptibility values are generally very low and the

Table 4. Stratigraphic listing of faunal events and paleomagnetic reversals for Holes 722A and 722B.

Event	Core level	Depth (mbsf)	Age (Ma)	Source of age	Notes
B <i>Emiliana huxleyi</i>	A1H-4, 115-117	5.65	0.19	3	
	1H-5, 115-117	7.15			
B <i>Collosphaera tuberosa</i>	1H-CC	9.80	0.40-0.59	1	Cores MD81-369, RC14-22 and VM34-35; DSDP 214 probably less accurate.
	2H-4, 85-87	15.15			
T <i>Pseudoemiliana lacunosa</i>	2H-5, 115-117	16.95	0.49	3	
	2H-6, 115-117	18.45			
B <i>Pterocorys hertwigii</i>	3H-4, 85-87	24.75	0.76-0.84	1	
	3H-CC	29.00			
T <i>Reticulofenestra</i> sp. A	4H-2, 118-119	31.68	0.82	3	
	4H-3, 115-117	33.15			
B <i>Gephyrocapsa parallela</i>	4H-5, 118-119	36.18	^a 0.89	4	
	4H-6, 118-119	37.68			
B Jaramillo	4H-6, 115-117	37.65	0.98	6	
	4H-7, 40-42	38.40			
B <i>Lamprocyrtis nigriniae</i>	4H-CC	38.60	1.02-1.07	1	
	5H-2, 85-87	40.95			
T <i>Gephyrocapsa</i> "large" ^b	5H-3, 115-117	42.75	^a 1.10	4	
	5H-4, 115-117	44.25			
T <i>Anthocyrtidium angulare</i>	5H-4, 85-87	43.95	0.94-1.04	1	
	5H-CC	48.20			
T <i>Lamprocyrtis neoheteroporos</i>	5H-4, 85-87	43.95	1.09-1.13	1	
	5H-CC	48.20			
T <i>Helicosphaera sellii</i>	6H-1, 115-117	49.35			No good published age; event appears to be diachronous.
	6H-2, 115-117	50.85			
B <i>Gephyrocapsa</i> "large" ^b	6H-2, 115-117	50.85	^a 1.36	4	
	6H-3, 115-117	52.35			
T <i>Calcidiscus macintyreii</i>	6H-3, 115-117	52.35	1.45	6	
	6H-4, 115-117	53.85			
B <i>Gephyrocapsa oceanica</i>	6H-3, 115-117	52.35	^a 1.57	4	
	6H-4, 115-117	53.85			
T <i>Pterocanium prismatium</i>	6H-4, 85-87	53.55	1.52-1.56	1	Rare in Hole 722A.
	6H-CC	57.50			
B <i>Gephyrocapsa caribbeanica</i>	6H-4, 115-117	53.85	^c 1.66	4,8	
	6H-5, 115-117	55.35			
T <i>Globigerinoides extermus</i>	6H-CC	57.50	^d 1.8	6	
	7H-2, 65-67	59.65			
B <i>Anthocyrtidium angulare</i>	6H-CC	57.50	1.52-1.64	1	
	7H-2, 85-87	59.85			
T <i>Discoaster brouweri</i>	7H-4, 114-116	63.14	1.90	6	
	7H-5, 115-117	69.65			
T <i>Discoaster pentaradiatus</i>	8H-5, 115-117	74.35	2.40	6	
	8H-6, 115-117	75.85			
Matuyama/Gauss	9H-4, 115-117	82.45	2.47	6	
	9H-5, 115-117	83.95			
B <i>Theocalypta davisiana</i>	8H-CC	76.80	2.42-2.44	1	
	9H-CC	86.50			
B <i>Lamprocyrtis neoheteroporos</i>	8H-CC	76.80	2.51-2.53	1	
	9H-CC	86.50			
T <i>Stichocorys peregrina</i>	8H-CC	76.80	2.62-2.64	1	
	9H-CC	86.50			
T <i>Phormostichoartus fistula</i>	11X-4, 85-87	101.55	3.26-3.28	1	
	11X-CC	105.90			
T <i>Lychnodictyum audax</i>	11X-4, 85-87	101.55	3.33-3.35	1	
	11X-CC	105.90			
T <i>Sphenolithus abies</i>	11X-5, 115-117	103.35	3.47	6	
	11X-6, 115-117	104.85			
T <i>Reticulofenestra pseudoubilica</i>	11X-CC	105.90	3.50	6	
	12X-1, 116-118	107.06			
T <i>Sphaeroidinellopsis</i> sp.	11X-CC	105.90	3.0	6	Rare in Hole 722A.
	12X-2, 65-67	108.05			
Gauss/Gilbert	11X-5, 115-117	103.35	3.40	6	
	12X-3, 115-117	110.05			
T <i>Phormostichoartus doliolum</i>	11X-CC	105.90	3.53-3.55	1	
	12X-4, 85-87	111.25			
B <i>Amphirhopalum ypsilon</i>	11X-CC	105.90	3.77-3.79	1	
	12X-4, 85-87	111.25			
coiling change in <i>Pulleniatina</i>	12X-4, 65-67	111.05	3.8	6	
	12X-CC	115.60			
B <i>Spongaster tetras tetras</i>	12X-CC	115.60	3.83-3.85	1	
	13X-4, 85-87	120.95			
<i>S. berminghami</i> to <i>S. pentas</i> ^e	12X-CC	115.60	4.3-4.44	2	? or lower.
	13X-4, 85-87	120.95			
T <i>Spongodiscus ambus</i>	14X-4, 85-87	130.65			
	14X-CC	134.90			
T <i>Didymocyrtis penultima</i>	14X-CC	134.90			
	15X-4, 85-87	140.25			
T Sidufjall	15X-5, 115-117	142.03	4.40	6	
	15X-6, 45-47	142.85			

Table 4 (continued).

Event	Core level	Depth (mbsf)	Age (Ma)	Source of age	Notes
T <i>Solenosphaera omnitubus</i>	15X-CC	144.60	4.7-4.8	2	
	16X-CC	154.30			
B <i>Sphaeroidinella dehiscens</i>	16X-2, 62-64	146.72	4.8	5	
	16X-4, 65-67	149.75			
B Thvera	16X-5, 40-42	151.00	4.77	6	
	16X-5, 123-125	151.83			
T <i>Discoaster quinqueramus</i>	17X-CC	163.90	5.6	6	Age appears to be erroneous.
	18X-1, 115-116	165.05			
T <i>Botryostrobus bramlettei</i>	18X-2, 85-87	166.25	4.9-5.0	2	
	18X-CC	173.60			
B <i>Globorotalia tumida tumida</i>	18X-2, 65-67	166.05	5.2	6	
	18X-4, 65-67	168.18			
T <i>Siphostichartus corona</i>	19X-4, 85-87	178.95	5.0-5.1	2	
	19X-CC	183.30			
Gilbert/Chronozone 5	19X-5, 113-115	180.73	5.35	6	
	19X-6, 115-117	182.25			
T <i>Stichocorys delmontensis</i>	19X-CC	183.30			
	20X-CC	193.00			
B <i>Pulleniatina primalis</i>	20X-4, 65-67	188.45	5.8	6	
	20X-CC	193.00			
T <i>Stichocorys johnsoni</i>	20X-CC	193.00	^f 5.7-5.8	2	
	21X-CC	202.70			
T <i>Acrobotrys tritubus</i>	22X-4, 85-87	208.05	5.3-5.4	2	Rare in Hole 722A.
	22X-CC	212.40			
B <i>Spongodiscus ambus</i>	22X-4, 85-87	208.05			
	22X-CC	212.40			
Chronozone 5/Chronozone 6	22X-6, 113-115	211.33	5.89	6	
	23X-6, 115-117	221.05			
<i>S. delmontensis</i> to <i>S. peregrina</i> ^e	22X-CC	212.40	6.1-6.7	2	
	23X-4, 85-87	217.75			
T <i>Calocyclus caepa</i>	24X-4, 85-87	227.35	6.2-6.6	2	Age in western Pacific.
	24X-CC	231.70			
T <i>Phormostichoartus marylandicus</i>	24X-CC	231.70			
	25X-CC	241.70			
B <i>Solenosphaera omnitubus</i>	25X-CC	241.70	6.3-6.5	2	
	26X-CC	251.00			
T <i>Diartus hughesi</i>	25X-CC	241.70	7.1-7.2	2	
	26X-CC	251.00			
B <i>Stichocorys peregrina</i>	26X-CC	251.00			
	27X-CC	260.70			
B <i>Discoaster quinqueramus</i>	28X-CC	270.40	8.2	6	
	29X-1, 114-116	271.54			
T <i>Dictyocoryne ontongensis</i>	28X-CC	270.40			
	29X-CC	280.00			
T <i>Botryostrobus miralestensis</i>	28X-CC	270.40	8.1-8.2	2	May be reworked.
	29X-2, 85-87	272.75			
B <i>Acrobotrys tritubus</i>	B29X-4, 85-87	271.25	7.7-7.8	2	Rare in Hole 722A.
	29X-CC	275.60			
T <i>Didymocyrtis laticonus</i>	29X-4, 85-87	271.25			
	29X-CC	275.60			
T <i>Diartus petterssoni</i>	29X-CC	275.60	8.1-8.2	2	
	30X-CC	285.30			
<i>D. petterssoni</i> to <i>D. hughesi</i> ^e	30X-CC	285.30	8.3-8.5	2	
	32X-CC	304.70			
B <i>Neogloboquadrina acostaensis</i>	31X-2, 65-67	287.45	8.6	7	
	31X-4, 65-67	290.45			
T <i>Stichocorys wolffii</i>	31X-CC	295.00	^g 8.0-8.2	2	
	32X-4, 85-87	300.35			
B <i>Botryostrobus bramlettei</i>	32X-4, 85-87	300.35	8.8-9.0	2	
	32X-CC	304.70			
T <i>Discoaster hamatus</i>	32X-CC	304.70	8.85	6	
	33X-1, 115-116	305.85			
B <i>Spongaster berminghami</i>	32X-CC	304.70	7.9-8.0	2	
	33X-CC	314.30			
B <i>Diartus hughesi</i>	32X-CC	304.70	8.7-8.8	2	
	33X-CC	314.30			
B <i>Discoaster hamatus</i>	34X-CC	324.00	10.0	6	
	35X-CC	333.70			
T <i>Cyrtocapsella japonica</i>	35X-4	329.35	10.0-10.3	2	
	35X-CC	333.70			
T <i>Globorotalia mayeri</i>	35X-CC	333.70	^h 10.4	6	
	36X-2, 65-67	335.85			
B <i>Globogerinoides nepenthes</i>	36X-CC	339.05	11.3	6	
	37X-4, 65-67	348.55			
T <i>Lithopera thornburgi</i>	37X-4, 85-87	348.75			
	37X-CC	353.10			
T <i>Cyrtocapsella cornuta</i>	37X-CC	353.10	11.6-11.9	2	
	38X-4, 85-87	358.45			

Table 4 (continued).

Event	Core level	Depth (mbsf)	Age (Ma)	Source of age	Notes
T <i>Globorotalia fohsi</i>	38X-4, 65-67	358.25	11.5	6	
	39X-CC	372.50			
B <i>Discoaster kugleri</i>	40X-2, 110-111	375.10	13.1	6	
	40X-CC	382.20			
T <i>Sphenolithus heteromorphus</i>	41X-1, 21-22	382.41	14.4	6	
	41X-2, 32-33	384.02			
T <i>Globorotalia peripheronda</i>	41X-CC	391.80	14.6	6	
	42X-2, 56-58	393.86			

Note: T = upper limit and B = lower limit. Sources of age are: 1 = Johnson et al., in press; 2 = Johnson and Nigrini, 1985; 3 = oxygen isotope data for Site 723 (N. Niitsuma, unpubl. data); 4 = Takayama and Sato, 1987; 5 = Barron et al., 1985; 6 = Berggren et al., 1985; 7 = van Gorsel and Troelstra, 1981; and 8 = Sato et al., in press.

^a North Atlantic data.

^b Long axis greater than 6 μm .

^c North Atlantic age consistent with Italian-type section.

^d *G. obliquus extremus* cited in Berggren et al., 1985.

^e An evolutionary transition.

^f *E. cf. diaphanes* cited in Johnson and Nigrini, 1985.

^g Pacific Ocean data.

^h *G. siakensis* cited in this source.

range of values is relatively narrow (~ 25 to 125×10^{-6} volume S.I. units). Hole 722A was APC-cored to 86.5 mbsf (Core 117-722A-9H), and recovery by drilling in XCB mode to 280.0 mbsf was generally very good. Occasionally, pipe-rust contamination of the XCB cores was so severe that many of the susceptibility features apparent in Holes 721B and 721C were obscured at Hole 722A. This condition generally prohibited intersite correlations below ~ 90 mbsf. However, within the common interval of APC recovery (above ~ 90 mbsf) susceptibility features between sites are correlatable to within the interval of measurement, or 5-10 cm (Fig. 15). Insufficient time was available at sea to create correlated composite sequences for Sites 721 and 722, this will be one of our main shore-based objectives.

Cyclicity in the susceptibility data of Holes 722A and 722B is apparent at ~ 1 m, 1-2 m, 3-4 m, and 12-14 m periods. Applying sedimentation rate of ~ 3.5 cm/k.y. obtained for Hole 722A, these periods correspond roughly to the 19-23 k.y., 41 k.y., 100 k.y., and ~ 400 k.y. periodicities of orbital insolation forcing. Below we discuss a preliminary analysis of the frequency spectra of the susceptibility data from Sites 721 and 722.

Hole 722B was APC-cored with full recovery to Core 117-722B-10H (91.9 mbsf), XCB-coring continued below this with generally good recovery to 565.6 mbsf (Fig. 16). As in Hole 722A, detailed intra- and intersite correlations are possible for the APC-cored sediments (Fig. 15). Detailed interhole correlations based on these data and lithologic marker layers are presented in the "Interhole Correlation" section (this chapter). The pipe-rust contamination seen in Hole 722A was less severe in Hole 722B, and this should permit some detailed correlations below the depth of APC recovery. Lithologic Unit I, a foraminifer-bearing nannofossil ooze extending to 221.5 mbsf, contains the low and cyclic susceptibility variations described previously (Fig. 16). Although Unit I contained couplets of alternating light greenish-grey and dark olive sediments within spacings of about 1 m, detailed comparison of these layers with the susceptibility data did not indicate a simple relationship between color and susceptibility. The siliceous nannofossil chalk facies of lithologic Unit II (221.5-343.4 mbsf) does not display any remarkable differences from lithologic Unit I in terms of the susceptibility data, except that the Unit II values are slightly higher. The cyclicity apparent in Unit I is also present in many of the less disturbed cores from Unit II. The cycles appear to have very regular ~ 1 -m periods (Fig. 17). The susceptibility data representative of lithologic Unit III (nannofossil chalk; 343.4-411.1 mbsf) are sparse due to the very poor recovery of this interval. Slightly increased susceptibility values were observed for Unit

III. The susceptibility cyclicity apparent in lithologic Units I and II is also present in some of the less disturbed sections of Unit III. Again, the predominant cyclicity is at ~ 1 -m periods (Fig. 17). Lithologic Unit IV consists largely of silty claystone turbidites interbedded with pelagic nannofossil chalks. As in Hole 721B, this unit coincides with a dramatic increase in susceptibility of nearly two decades (Fig. 16). The data of Unit IV do not have the cyclic periodicities which were present in the previous lithologic units; the increase in values is most likely in response to the increased grain size and concentration of ferromagnetic grains.

Spectral Analysis

Noting that the frequencies of susceptibility variation were roughly coincident with those predicted by Milankovitch orbital insolation anomalies, we analyzed the frequency spectra of two susceptibility records. Since core quality and recovery were best for the APC cores, the data from the first nine APC cores of Holes 721B (to 86.0 mbsf) and 722A (to 86.5 mbsf) were selected for spectral analysis. A principal constraint for our analyses, however, was the lack of detailed age-depth data. For both holes, the only firm datums available were the Jaramillo/Matuyama boundary (0.98 Ma) and the Matuyama/Gauss boundary (2.48 Ma). Depth tabulations of these datums for Hole 722A and 721B are shown in Table 5 (this chapter) and Table 7 of the "Paleomagnetism" section in the "Site 721" chapter (this volume). The susceptibility data for both holes were linearly interpolated to age, resampled to equal age increments of 1.5 k.y. and linearly detrended. The total time-series represented is 0 to ~ 2.7 Ma for Hole 721B, and 0 to ~ 2.6 Ma for Hole 722A.

The frequency spectra program used in this analysis uses a windowing procedure in which the data set is subdivided into a series of overlapping data subsets, or windows. Each window is one-quarter length of the entire data set (~ 0.68 Ma for Hole 721B, ~ 0.65 Ma for Hole 722A). The power spectrum is calculated for the first window, then the window position shifts downward to a level equal to one-eighth of the data-set length, and then the power spectrum of the second window is calculated. For a given data set, spectra are calculated for seven consecutive, overlapping windows.

The resulting frequency power spectra for Holes 721B and 722A are shown in Figure 18. Vertical lines are drawn to show the positions of the principal orbital periodicities of precession (19 k.y., 23 k.y.), obliquity (41 k.y.), and eccentricity (100 k.y., ~ 400 k.y.). Although the age models are crude, the calculated power spectra of both holes suggest that orbital periodicities are

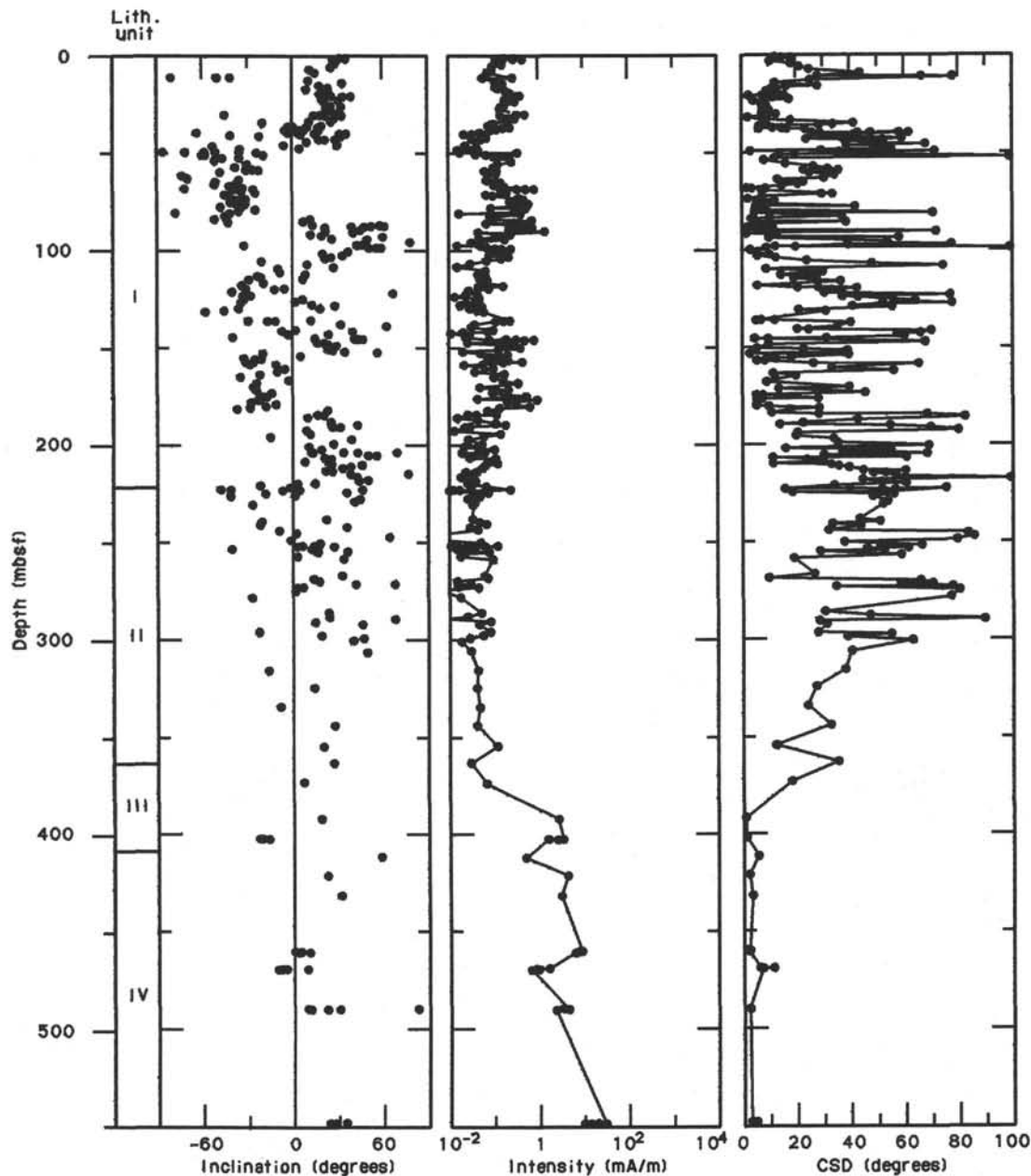


Figure 12. Inclination, intensity, and circular standard deviation (CSD) for the combined discrete sample sets from Holes 722A and 722B.

present in the susceptibility data. The windowing procedure illustrates two important aspects of the observed power spectra. First, the 23 k.y./19 k.y. precessional couplet can be seen to shift in unison toward slightly higher and lower frequencies than expected. This suggests that the orbital spectra are present but are displaced due to age model inadequacies. Second, the distribution of power among the 100 k.y., 41 k.y., 23 k.y., and 19 k.y. frequencies is highly variable between windows. Although this may also be a consequence of crude age modeling, the general shift in both Holes 721B and 722A from high 100-k.y. power for the youngest windows (0–1.0 Ma) to high 41 k.y. power for the oldest windows (~1.0–2.6 Ma) may be significant in terms of paleoclimate. This tentative interpretation is consistent with oxygen-isotope and sea-surface temperature data from the North Atlantic which indicate that the predominantly 41-k.y. periodic-

ity of ice-sheet-induced climate variability during the late Pliocene to middle Pleistocene shifted to a predominantly 100-k.y. periodicity during the late Pleistocene (Pisias and Moore, 1981).

ACCUMULATION RATES

Sedimentation rates for Site 722 are based on the mean depth and age magneto- and biostratigraphic datum levels identified in Holes 722A and 722B (Table 4 and Fig. 19). Because of uncertainties in the shipboard paleomagnetic data (see "Explanatory Notes" section, this volume), we favor the nannofossil biostratigraphic datums for the determination of the sedimentation rates at Leg 117 sites. For the interval from 0 to 2.4 m.y., we used six nannofossil datums with ages based on oxygen isotope stratigraphy (Niitsuma, unpubl. data) and from Berggren et al. (1985) to determine variations in the mean sedimentation (Ta-

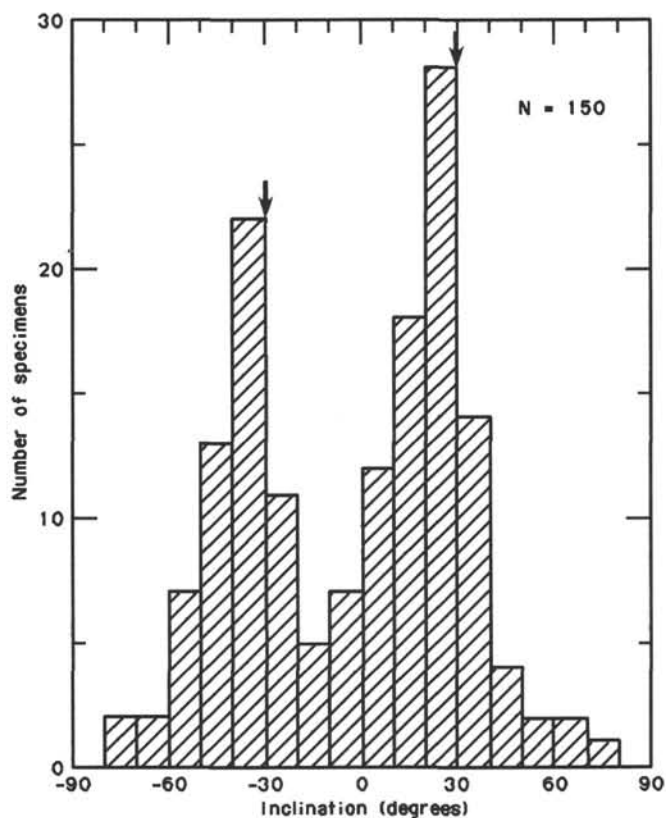


Figure 13. Histogram of the inclination values of discrete samples from Holes 722A and 722B. Arrows show the expected geocentric axial dipole inclination values for the site latitude.

bles 4 and 7). These same biohorizons are used to determine the mean sedimentation rate at other Leg 117 sites to permit the comparison of sediment accumulation of hemipelagic deposits on the Oman margin and the pelagic sediments on the Owen Ridge.

Site 722 cored the same sedimentary sequence as in nearby Site 721, and the same four lithologic units are identified at both sites. These lithologic units reflect the changing depositional environment of the site due to uplift of the Owen Ridge, and variations in surface plankton productivity. The cored section at Site 721 contains a hiatus between Units III and II and postdepositional disturbance of Units II and IB. However, these intervals appear complete and undisturbed in Site 722. Because of poor age control in the turbidite sequence of lithologic Unit IV, no estimate of sedimentation can be made at this time.

Lithologic Unit III, a nannofossil chalk deposited in the middle Miocene, is characterized by relatively low mean sedimentation rates of 8–15 m/m.y. These low rates reflect pelagic sedimentation above the zone of turbidite deposition but still in waters corrosive to calcium carbonate. The transition from Unit III to II is identified by an increase in opal and organic-carbon-rich sediments which characterize lithologic Unit II. High sedimentation rates which average 54 m/m.y. are associated with these upper Miocene opal-rich sediments (Fig. 20 and Table 7).

The nannofossil oozes/chalks of lithologic Unit I ranging from late Miocene to Holocene were deposited at rates of 17–45 m/m.y. (Fig. 20 and Table 7). These are similar to the rates at Owen Ridge Sites 721 and 731 over this same time interval and of pelagic sedimentation in other areas, but are two to five times lower than rates during comparable time intervals from hemipelagic deposits on the Oman margin.

The mass accumulation rates of calcium carbonate, noncarbonate ($100 - \text{CaCO}_3$), and organic carbon are calculated from

the average values between selected datums (Table 7 and Fig. 20). These data allow independent examination of the temporal variability in each component. The accumulation rates of calcium carbonate and noncarbonate at Site 722 mostly mirror the sedimentation rate, and calcium carbonate accumulation is generally twice that of noncarbonate in upper Miocene to Pleistocene deposits. These rates are similar to those found at carbonate-rich sites in the eastern equatorial Pacific (Theyer et al., 1985) and are characteristic of areas having a high production of calcium carbonate shells of coccolithophores and foraminifers with minimal postdepositional dissolution.

PHYSICAL PROPERTIES

Introduction

Physical properties measured on discrete samples of sediments recovered from Site 722 include index properties (wet-bulk density, porosity, water content, and grain density), compressional-wave velocity, and vane-shear strength. The properties that were determined for discrete samples from Holes 722A and 722B are listed in Tables 8 and 9, respectively. Wet-bulk density and compressional-wave velocity were measured on all whole-round sections longer than 80 cm using the GRAPE and *P*-wave logging systems. All techniques and equipment used are described in the "Explanatory Notes" chapter (this volume).

The pattern of variation of physical properties at Site 722 is very similar to the pattern recognized at Site 721. Transitions in the physical properties profiles mark the boundaries between the four lithologic units at Site 722 in a manner similar to that at Site 721. Principal differences between the sites are a greater thickness of low-density, high-porosity sediments of the opal-rich nannofossil chalk in lithologic Unit II and a thicker interval of gradational change at the top of lithologic Unit III.

Index Properties

Lithologic Unit I

The index properties of lithologic Unit I (0–221.5 mbsf) are nearly identical to those of lithologic Subunit I (0–261.2 mbsf) at Site 721. Porosity and water content averages range from 64% and 40%, respectively, near the seafloor to 59% and 35%, respectively, at the base of the unit (Fig. 21). Wet-bulk density increases from 1.65 g/cm³ near the seafloor to 1.74 g/cm³ at the base of lithologic Unit I (Fig. 21). The wet-bulk density minimum and porosity maximum between 90 to 110 mbsf at Site 722, which coincide with an increase in the clay percentage, are also present at similar depths at Site 721.

Lithologic Unit II

Lithologic Unit II (221.5–343.4 mbsf) includes sediments with anomalously high porosity and water content and low grain and bulk densities (Fig. 21) in association with an increased abundance of siliceous microfossils. The maximum porosity within Unit II is 76%, and the minimum grain and wet-bulk densities are 2.30 g/cm³ and 1.42 g/cm³, respectively. Lithologic Unit II at Site 722 is approximately 72 m thicker than the corresponding interval at Site 721. The upper 60 m of the unit maintains the porosity and density trends of lithologic Unit I, but displays more widely varying properties than Unit I.

Lithologic Unit III

Lithologic Unit III (343.4–411.1 mbsf) contains an upper interval, 40 m thick, in which porosity rapidly decreases with depth from 60% to 45% and wet-bulk density increases from 1.74 to 2.02 g/cm³ (Fig. 21). This interval of gradational change is not present at Site 721 where the top of lithologic Unit III (309.9–340.7 mbsf) is marked by an unconformity and an abrupt change

Table 5. Location and age or inferred polarity transitions at Site 722.

Hole, core, section, interval (cm)	Depth (mbsf)	Transition	Age (Ma)
722A-4H-6, 115/4H-7, 40	37.65/38.40	C1r-1 (Jaramillo) Bottom	0.98
722A-9H-4, 115/9H-5, 115	82.45/83.95	C2A (Gauss) Top	2.47
722A-11X-5, 115/12X-3, 115	103.95/110.05	C2A (Gauss) Bottom	3.40
722A-15X-5, 115/15X-6, 45	142.03/142.85	C3.2r-1 (Sidufjall) Top	4.40
722A-16X-5, 40/16X-5, 123	151.00/151.83	C3.3 (Thvera) Bottom	4.77
722A-19X-5, 113/19X-6, 115	180.73/182.25	C3A (Chronozone 5) Top	5.35
722A-22X-6, 113/23X-6, 115	211.33/221.05	C3A (Chronozone 5) Bottom	5.89
722B-5H-4, 100/5H-5, 30	39.80/40.60	C1r-1 (Jaramillo) Bottom	0.98
722B-10X-1, 110/10X-2, 100	83.80/85.20	C2A (Gauss) Top	2.47
722B-12X-2, 100/12X-3, 108	104.00/105.58	C2A (Gauss) Bottom	3.40
722B-17X-2, 100/17X-4, 100	152.40/155.40	C3.3 (Thvera) Bottom	4.77
722B-20X-2, 99/21X-1, 110	181.39/189.60	C3A (Chronozone 5) Top	5.35
722B-24X-1, 100/24X-3, 100	218.50/221.50	C3A (Chronozone 5) Bottom	5.89

Table 6. Core orientation data for Site 722: comparison of multishot and measured mean core declination estimates.

Hole and core	Multishot orientation (°)	Measured mean core declination (°)	Corrected mean core declination (°)
722A-5H	303	61 (N)	118
722A-6H	110	90 (R)	340
722A-7H	305	301 (R)	356
722B-6H	260	157 (R)	257
722B-8H	224	180 (R)	316
722B-9H	157	239 (R)	82
722B-10H	332	252 (R)	280

Note: N = normal polarity; and R = reversed polarity. Corrected mean core declination = measured mean core declination/multishot orientation. The resultant value should be 0° for normally magnetized cores and 180° for reversely magnetized cores.

in physical properties. Below 383 mbsf the index properties are nearly constant with depth.

Lithologic Unit IV

Lithologic Unit IV at Site 722 (411.1–565.6 mbsf) displays a uniform decrease in porosity and increase in wet-bulk density nearly identical to that of lithologic Unit IV at Site 721 (340.7–424.2 mbsf). Porosity decreases in Unit IV from 45% to 42%, and wet-bulk density increases from 1.95 to 2.05 g/cm³ (Fig. 21). This unit was drilled to a greater depth at Site 722, and near the depth of maximum penetration, well-lithified sandstones were recovered in Cores 117-722B-55X (517 mbsf) and 117-722B-56X (527 mbsf). Index properties were only obtained from a sample from Core 117-722B-55X. The porosity and wet-bulk density of this sample are 12% and 2.71 g/cm³, respectively.

Compressional-Wave Velocity

At Site 722 compressional-wave velocities were measured perpendicular to bedding (V_v) on discrete samples from all cores recovered from Holes 722A and 722B from which suitable samples could be prepared. Velocities were also measured parallel to bedding (V_h) on samples from Hole 722B that were sufficiently indurated to allow a cubic sample to be cut using a razor blade or rock saw. Variation in compressional-wave velocities measured in the sediments recovered from Site 722 is comparable to that found at Site 721 at all sub-bottom depths. In spite of the wide variation of the data, general trends, similar to those at Site 721, can be identified and correlated with index properties.

Within the nannofossil ooze of lithologic Unit I, V_v increases gradually with depth and with decreasing porosity (Fig. 22). Surficial values near 1500 m/s increase to about 1600 m/s at the

base of lithologic Unit I (221.5 mbsf). In the upper portion of lithologic Unit II, the gradual decrease in bulk density associated with an increasing abundance of siliceous microfossils is accompanied by a decrease in compressional-wave velocity. Velocity and bulk density minima of 1520 m/s and 1.42 g/cm³ are coincident near 315 mbsf. Near the base of lithologic Unit II, the sediments are sufficiently indurated to allow velocities to be measured parallel to bedding (Fig. 22). Within the basal sequence of Unit II, V_h averaged 2.1% higher than V_v .

The gradual reduction in abundance of the siliceous microfossils in the lower portions of lithologic Unit II is marked by an increase in velocity that continues throughout the nannofossil chalk of Unit III. Markedly higher velocities were measured in two samples of well-indurated nannofossil chalk from lithologic Unit III; Sample 117-722B-41X-1, 22–24 cm, and Sample 117-722B-43X-1, 40–42 cm, transmit compressional-waves perpendicular to bedding at 1944 m/s and 1902 m/s, respectively, and parallel to bedding at 2064 m/s and 2022 m/s, respectively (Fig. 22 and Table 9).

At Site 722, as at Site 721, velocities in lithologic Unit IV vary widely despite a relatively uniform increase in density with depth. Throughout this unit, velocities are 50 to 200 m/s less than predicted by empirical relations for similar lithofacies (Hamilton, 1978). Bedding-parallel velocities are comparably low.

Given the high variability of the velocity data at Site 722, velocity-density relations for these sediments are loosely defined (Fig. 23). The general trends displayed by the nannofossil ooze/chalk, diatomaceous-nannofossil chalk, and clay-rich turbidites are however distinct. Compressional-wave velocity increases more rapidly with density in the clay-rich units than in the more calcareous sequences. The diatomaceous-nannofossil chalks of lithologic Unit II show the weakest correlation between velocity and density, and the most gentle velocity-density gradient.

Anisotropy of the compressional-wave velocities for both the nannofossil ooze/chalk of lithologic Units I through III and the clay-rich sequences of Unit IV are displayed on a crossplot of V_v and V_h (Fig. 24). In the calcareous sediments, anisotropy tends to increase with density from an average of 2.4% in Cores 177-722B-34X to -40X to 58% in the indurated chalks of Core 117-722B-41X and -43X. It is also evident, however, as it has been to other investigators (e.g., Carlson et al., 1983), that anisotropy of calcareous sediment can vary significantly with density. In the clay-rich sequences, anisotropy shows no consistent relationship with density.

GRAPE and P-Wave Logs

GRAPE and P-wave logger records are of similar quality and character as those at Site 721. Large-scale features such as the density minimum between 90 and 110 mbsf and the transition interval at the top of lithologic Unit III are evident on the logs

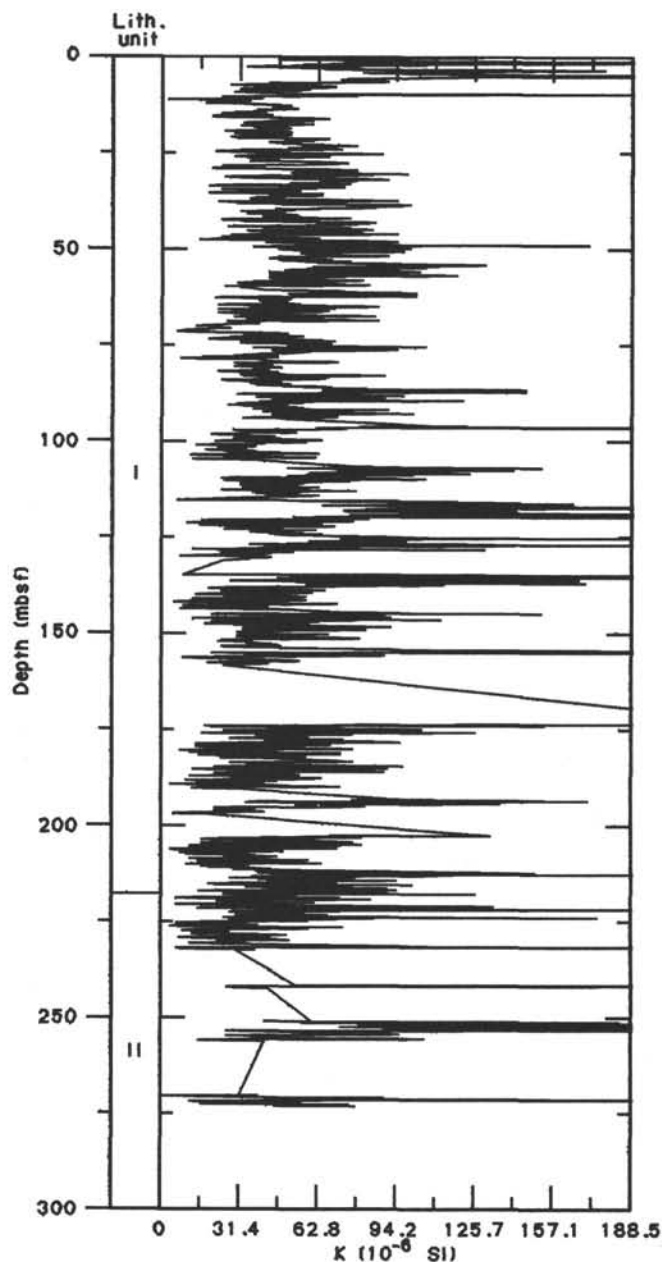


Figure 14. Hole 722A volume magnetic susceptibility data.

(Fig. 25). Smaller-scale cyclic variation, on the order of 1 m, is present in the GRAPE and *P*-wave records from lithologic Unit I. These features can be correlated between holes at Site 722 and between Site 722 and Site 721 (Fig. 26).

Vane Shear Strength

Vane shear strengths were measured in seven APC and one XCB cores from Hole 722A (Table 8). Shear strengths were comparable to those measured at Site 721, ranging from 19.1 kPa at 5.0 mbsf to 73.1 kPa at 62.5 mbsf.

SEISMIC STRATIGRAPHY

The Owen Ridge is an asymmetric linear feature in the western Arabian Sea that trends northeastward and dips gently to the west (see Fig. 1). At DSDP Site 224, the ridge is uplifted lamprophyre basement overlain by claystones, chinks, and turbiditic sequences of Eocene to Miocene that are in turn capped

by Miocene and younger pelagic sediments (Whitmarsh et al., 1974; Whitmarsh, 1979).

The seismic stratigraphy of the ridge is complex and includes irregular basement features, large-scale onlap of turbidite and other facies, numerous slump scars and large slump(?) canyons, as well as several prominent sub-bottom reflectors. To interpret the seismic stratigraphy of Site 722, we have used several single channel seismic (SCS) profiles from the Leg 117 site survey by the *Robert Conrad* (RC2704), in combination with the drilling results from Site 722 (see "Lithostratigraphy" section, this chapter). Downhole logging data from Site 722 (see "Downhole Measurements" section, this chapter), as well as the SCS data obtained during the site approaches by the *JOIDES Resolution*, were also used for this synthesis. Figure 27 shows the location of the SCS tracks used in this discussion in relation to the bathymetry of the Owen Ridge (Sea Beam data from the site survey; Prell, unpubl. data).

The sedimentary sequence at Site 722 is relatively complete with no major hiatuses. Thus, we use the results of drilling and logging at Site 722 and SCS Line 38 to define the relationship between reflector sequences and the lithologic section of the northern Owen Ridge. Here we discuss the synthetic seismogram generated from the downhole logging data and summarize the identification and lithologic significance of the important reflectors within the seismic section at Site 722.

Synthetic Seismogram

Based on sonic and density logs obtained at Site 722, a synthetic seismogram was calculated. We used a convolutional model with interbed multiples. The wavelet utilized is an estimate of the water-gun source signature of *Robert Conrad* (see "Downhole Measurements" section, "Site 720" chapter, this volume). The synthetic seismogram begins at the first open-hole log data (93 mbsf) and extends to the deepest sonic data obtained (543 mbsf). The synthetic seismogram and the acoustic impedance log, on which the synthetic was based, are shown in Figure 28.

Site 722

Correlation of the major reflectors recognized in the seismic profile (Line 38, Figs. 27, 28, and 29) with the synthetic seismogram and lithologic units at Site 722 is shown in Figure 28. The traveltimes-depth relationship of the lithologic units is shown in Figure 30. The reflectors are identified by an alpha-numeric code and are discussed in order of increasing depth below seafloor.

At Site 722, the upper 0.33 s of the seismic profile is characterized by parallel, conformable reflectors that represent the pelagic drape deposited on the Owen Ridge after the early Miocene.

Reflector A occurs at 0.33 s and is a high-amplitude return that is coincident with the top of the siliceous lithologic Unit II in Site 722 (Fig. 30). In the synthetic seismogram, the reflector corresponds to the largest peak in a triplet of peaks associated with the transition from lithologic Unit I to II (Fig. 28). It can be easily traced through Line 39 to the crest of the ridge (Line 40, Fig. 39, "Seismic Stratigraphy" section, "Site 721" chapter, this volume).

Reflector B is a series of reflectors that are associated with the siliceous and chalk units at Site 722. B₁ marks the bottom of a package of four closely spaced conformable reflectors that have a distinctive pattern and are coincident with the lower part of siliceous lithologic Unit II in Site 722 (Figs. 28 and 30). The top of this package is also observed as a reflector and is associated with a hard streak in the drilling (Fig. 30). Reflector B₁ is observed in the synthetic as a small peak that coincides with the siliceous-chalk transition and the ramp of increasing impedance (Fig. 28). B₁ was selected as a key reflector because it corre-

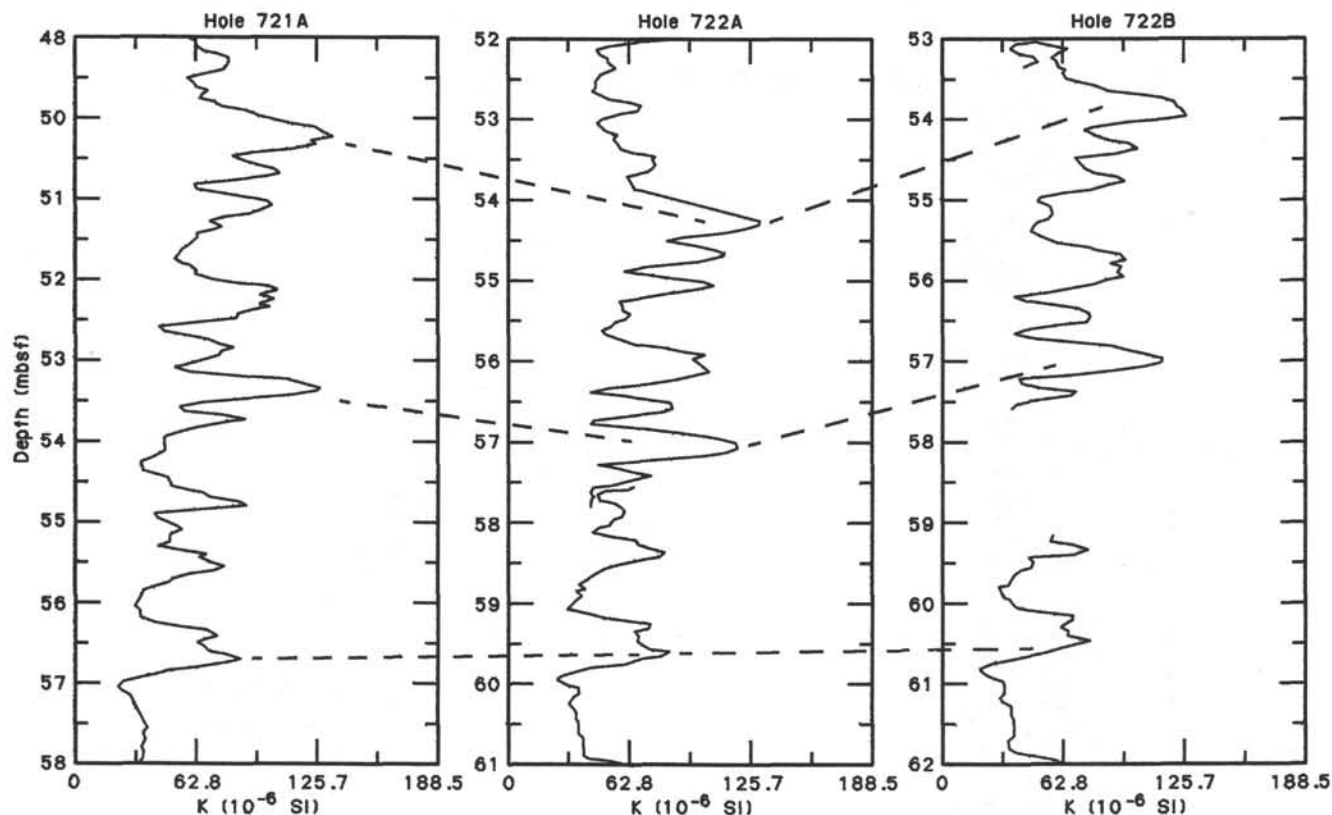


Figure 15. Intra- and intersite correlations between Holes 722A, 722B, and 721A using magnetic susceptibility.

sponds to a specific lithologic boundary. B_1 is easily traced to the crest of the ridge, but is missing at Site 721 ("Seismic Stratigraphy" section, "Site 721" chapter, this volume). B_2 is a low-amplitude reflector that correlates with the top of the chalks in the lower half of lithologic Unit III at Site 722 (Fig. 30). These chalks have higher velocity and a higher density than the surrounding lithologies, but the synthetic shows only a small peak (Fig. 28), because the two-way traveltime through the high-velocity chalks is less than the duration of the wavelet. The amplitude of seismic reflector B_2 increases between Site 722 and the crest of the ridge and is probably related to the pronounced hiatus identified at this level in Site 721, which brings lower velocity siliceous sediments in contact with the much faster lower chalk unit. As Site 722 does not contain this hiatus, the corresponding high amplitude of reflector B_2 was not found at Site 722. Reflector B_3 coincides with the boundary between the chalk (lithologic Unit III) and the turbiditic sediments of lithologic Unit IV at Site 722 (Figs. 28 and 30). It appears in the synthetic seismogram as a distinct peak/trough pair that corresponds with a sharp drop in impedance across the chalk-turbidite transition.

Seismic reflector C is the uppermost strong return of a thick series of generally parallel reflectors that are generally correlated to turbidite deposits within lithologic Unit IV at Site 722 (Figs. 28 and 30). Reflector C is not, however, the top of lithologic Unit IV, which is marked by B_3 . The synthetic seismogram shows one large peak between reflectors C and B_3 that is lower in amplitude on the seismic profile. About 0.05 s below C in the vicinity of Site 722, the reflector pattern is laterally heterogeneous, because of onlapping fill of a small topographic low.

Regional Seismic Stratigraphy

On a larger scale, the seismic stratigraphy of the sediments capping the crest of the Owen Ridge reveals that Site 722 overlies a basement high. The sediment thickness at Site 722 is about

0.82 s. The sediments overlie an irregular reflector, interpreted as basement, that dips to the west and is truncated against the eastward facing scarp of the Owen Ridge. Overlying portions of the basement (especially in the strike section, Line 38, Fig. 29) is a zone of diffuse reflections from about 0.82 to 0.67 sbsf. This diffuse zone thins and laps onto the basement peaks and is succeeded by a thick sequence of strongly reflective layers that lap onto the underlying sediments. This sequence is capped by reflector C and is interpreted as the clastic-turbidite facies of Oligocene to Miocene age that was observed at DSDP Site 224 (Whitmarsh et al., 1974) and at the base of Site 722. The surface of the turbidite facies (reflector C) dips only slightly to the north but about 4° to the west.

These new seismic data support the idea that the Owen Ridge is uplifted oceanic crust that was initially covered by flat-lying claystones and siltstones resulting from turbiditic and gravity deposition. These sediments lapped onto the basement highs and their drapes of older sediments to almost the level of the seafloor. No basement peaks are observed above reflector C. Uplift of the turbidite sequences (reflector C and below) probably began in early Miocene, because this is the last occurrence of turbidites in the sequence. However, some onlap can be observed prior to reflector C so that uplift may have begun earlier. Following the termination of the turbidite deposition, the ridge at Site 722 has been the locus of pelagic deposition since the late early Miocene. The reflectors within this pelagic cap largely reflect changes in the lithology of the pelagic sediments.

INORGANIC GEOCHEMISTRY

Introduction

Twenty interstitial water samples were collected throughout the four lithostratigraphic units at Site 722, nineteen by squeezing and one using the Barnes *in-situ* sampler. Samples were col-

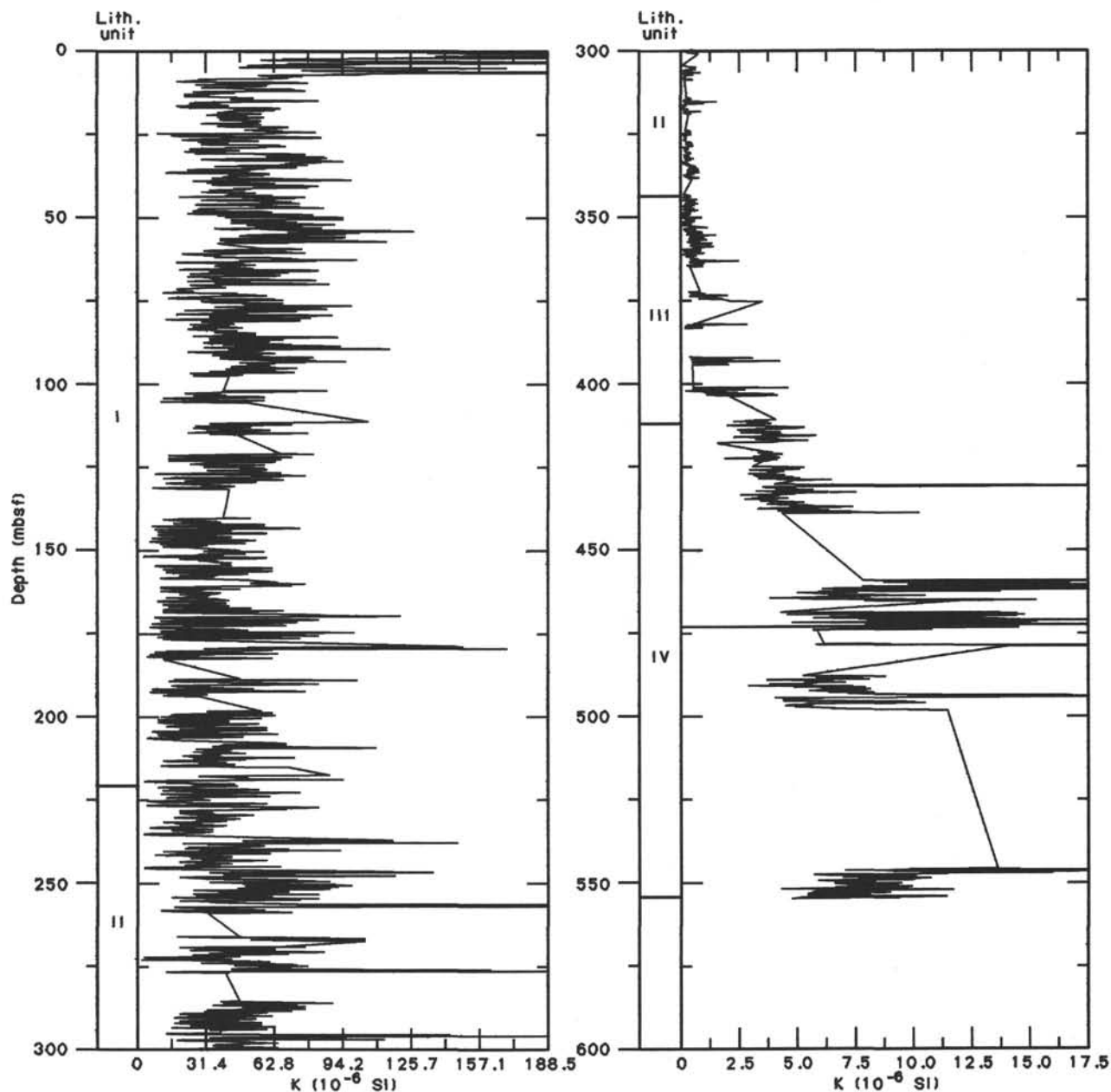


Figure 16. Hole 722B volume magnetic susceptibility data.

lected from Hole 722A down to 254 mbsf, and from the lower half of Hole 722B down to a total depth of 552 mbsf. All data are presented in Table 10, while Figure 31 combines analyses from both holes.

Salinity, Chlorinity, and pH

The concentration profiles of salinity, chloride and pH are shown in Figure 31. In comparison with Site 721, the salinity profile shows very little structure, and certainly no marked decrease over the top ~100 mbsf. In contrast, the chloride profile indicates an increase in concentration from 549 mmol/L in Core 117-722A-1H to ~570 mmol/L at 438 mbsf. This gradient of 0.048 mmol/L/m is approximately constant over lithostratigraphic Units I, II, and III. Within Unit IV (turbidites), the salinity decreases slightly, while a marked drop in interstitial chlo-

ride concentration (~20 mmol/L) indicates a very different pore water chemistry in this lithology (see discussion below). The chloride minimum at 464 mbsf is accompanied by a local minimum in salinity (Fig. 31). The reason for these relatively abrupt changes is unknown, but they do appear to be real and not analytical artifacts.

The pH ranges from 7.19 to 7.79 over the cored section and displays a vertical structure very similar to that in Hole 721. These values, which in all cases are lower than that of seawater, probably reflect release of H^+ during H_2S dissociation. The high pH value at 252 mbsf in Core 117-722B-27X-4 probably occurred as a sampling artifact as a delayed measurement allowed CO_2 to degas from the sample.

The *in-situ* sample at 276 mbsf was characterized by an anomalous salinity of 34.4 g/kg, a high magnesium level, slightly ele-

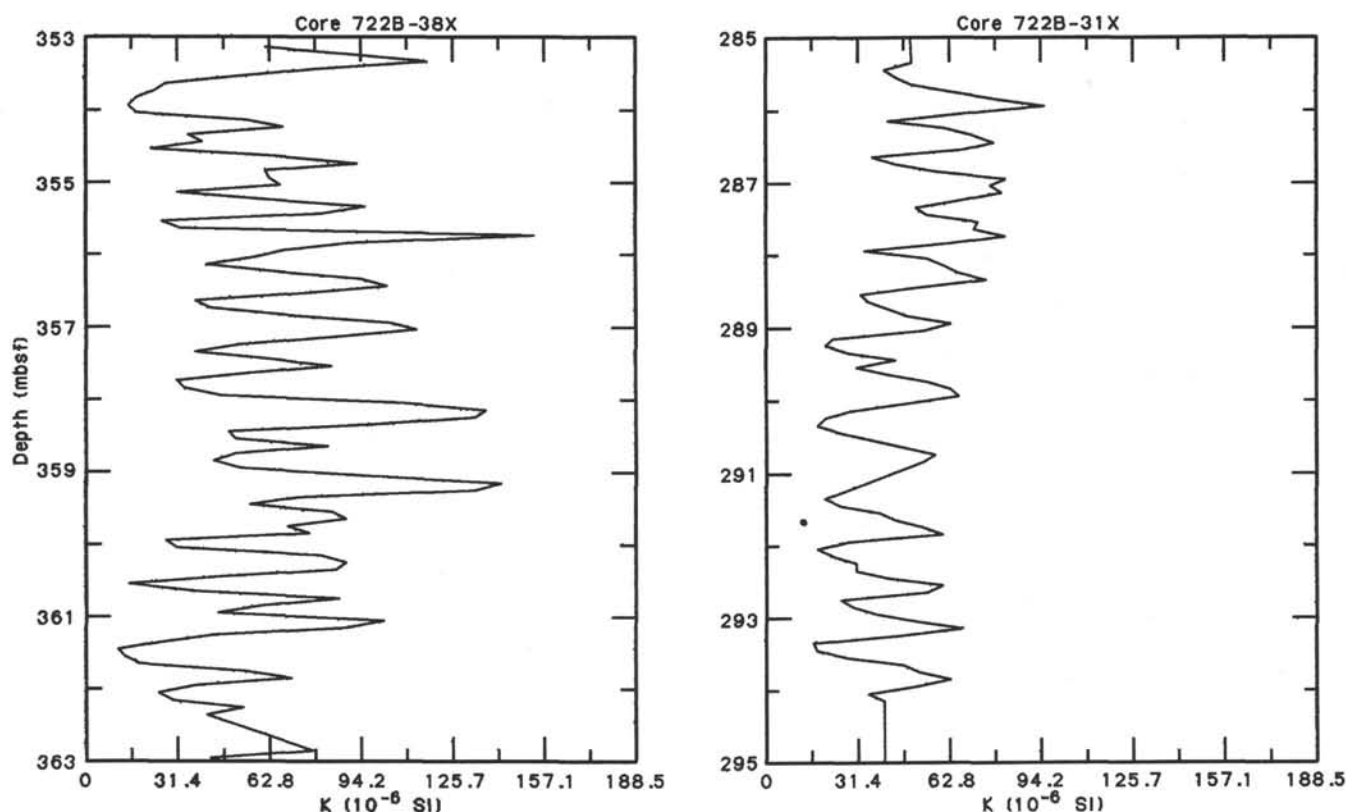


Figure 17. Susceptibility data from lithologic Unit III (Core 117-722B-38X) and lithologic Unit II (Core 117-722B-31X). Note that both lithologic units display cyclic susceptibility variations over less than 1 m. Measurement interval is 10 cm.

Table 7. Sedimentation and accumulation rate data for Site 722.

Depth interval (mbsf)	Age range (m.y.)	CaCO ₃ (\bar{x} %)	C _{org} (\bar{x} %)	Dry-bulk density (\bar{x} g/cm ³)	Sed. rate (\bar{x} m/m.y.)	CaCO ₃ acc. rate (g/cm ² /k.y.)	Non-CaCO ₃ acc. rate (g/cm ² /k.y.)	C _{org} acc. rate (mg/cm ² /k.y.)
0-6.4	0-0.19	62.7	0.35	1.017	33.7	2.15	1.28	12.0
6.4-17.7	0.19-0.49	75.4	ND	0.991	37.7	2.82	0.92	ND
17.7-32.4	0.49-0.82	69.9	0.85	0.981	44.5	3.05	1.31	37.1
32.4-53.1	0.82-1.45	66.2	ND	1.029	32.9	2.24	1.14	ND
53.1-66.4	1.45-1.90	59.2	1.13	1.094	29.6	1.92	1.32	36.6
66.4-75.1	1.90-2.40	71.5	ND	1.091	17.4	1.36	0.54	ND
75.1-120.0	2.40-4.0	70.1	1.26	1.032	27.7	2.00	0.85	36.0
120.0-251.0	4.0-7.1	70.8	1.20	1.082	42.3	3.24	1.34	54.9
251.0-305.0	7.1-8.1	52.9	1.23	1.021	54.0	2.92	2.60	67.8
305.0-380.0	8.1-13.1	49.4	1.31	1.070	15.0	0.79	0.81	21.0
380.0-392.0	13.1-14.6	91.2	ND	1.541	8.0	1.12	0.11	ND

Note: ND = no data for the interval.

vated sulfate, and a lowered silicate concentration. We believe that this sample was at least partially contaminated with seawater during sampling.

Sulfate and Alkalinity

Sulfate reduction at Site 722 is pronounced over the top ~100 meters of the core, but is measurable down to a depth of 208 mbsf. Consumption of sulfate as an oxidant during degradation of organic matter results in an increase in HCO₃⁻ and hence in alkalinity from 5.0 mmol/L in Core 117-722A-1H to 9.1 mmol/L in Core 117-722A-9H at 83 mbsf. In a fashion similar to Site 721, the alkalinity deficit is probably due to authigenic carbonate precipitation. However, assuming that similar solubility controls exist at both sites, the deeper penetration of sulfate and lower maximum alkalinity value may indicate that the content of degradable organic matter is more limited at Site 722.

Below the maximum at 83 mbsf, alkalinity decreases linearly (0.023 mmol/L/m) to a depth of ~400 mbsf. Over the remaining ~150 m of Hole 722B the alkalinity is almost constant at 1.6-1.8 mmol/L. The break in gradient at 400 mbsf coincides with the depth at which SiO₂ is consumed in diagenetic reactions (see discussion below) in the marly nannofossil chalk of Unit III. Alkalinity is consistently <2 mmol/L throughout the turbidites of Unit IV. The lack of curvature in the profile at depth suggests that diagenetic reactions involving carbonate precipitation are limited.

The sulfate increase below 317 mbsf is somewhat of an enigma. Three possibilities for the occurrence of the sulfate may be advanced (we believe no artifacts were introduced in either the sample collection or analysis): (1) seawater became "trapped" during rapid turbidite emplacement and "sealed" with a pelagic clay drape; (2) the cored section has penetrated sulfate-rich

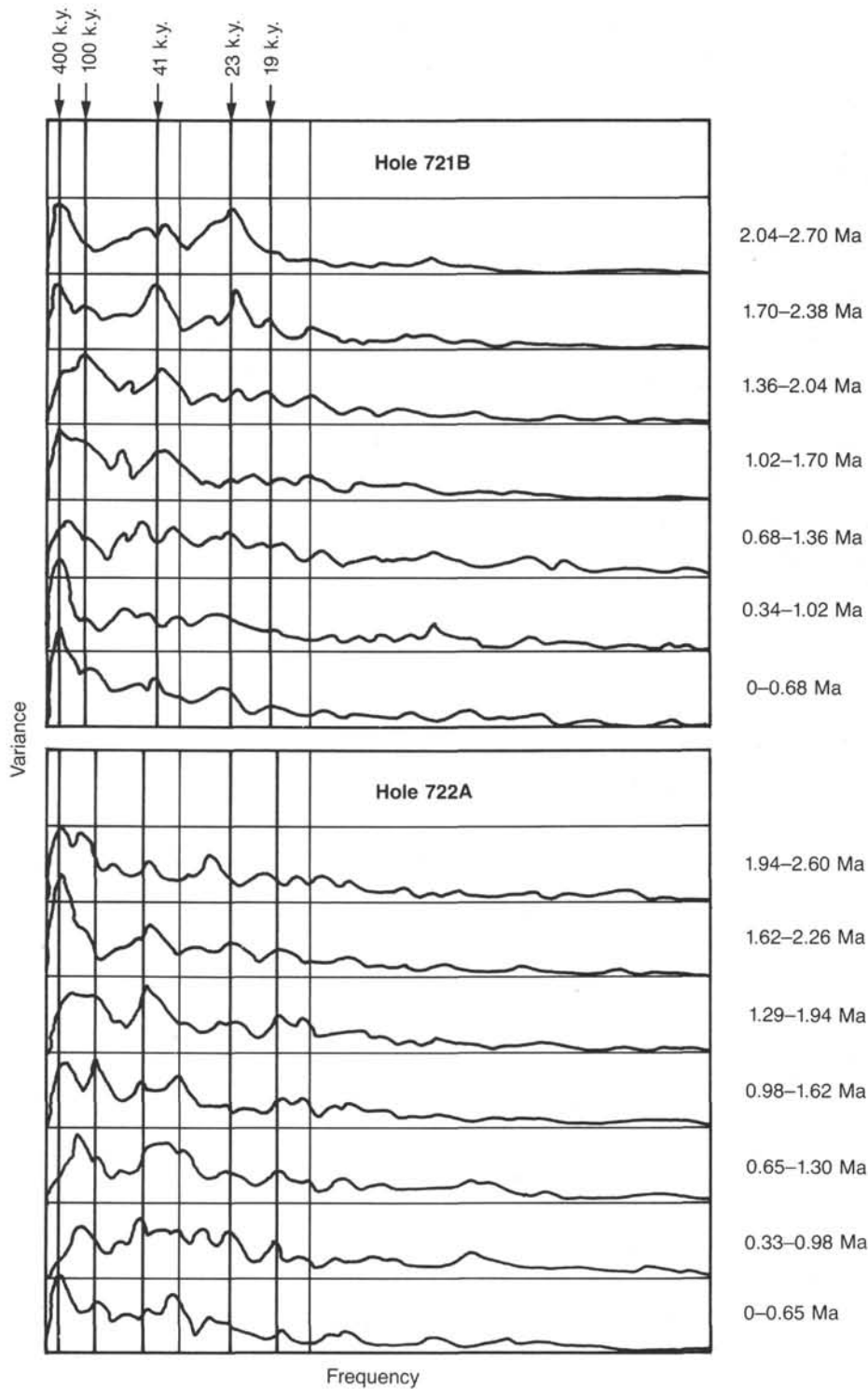


Figure 18. Spectral analysis results for Hole 721B (0-~2.7 Ma) and Hole 722A (0-~2.60 Ma) susceptibility data. Vertical lines indicate the positions of the orbital periodicities at ~400, ~100, 41, 23, and 19 k.y.

brines; or (3) dewatering during compaction and lithification of the sandstones has led to minor pyrite oxidation. Hypothesis (1) requires restricted diffusion of SO_4^{2-} over the last 15 Ma. With our present knowledge of SO_4^{2-} diffusivity and accumulation rates in Unit IV (>5 m/m.y.), the sulfate content of the trapped sea water is unlikely to be preserved (the diffusion path length would be on the order of 100 m/m.y.). The presence of brines is

also unlikely because the increase in sulfate is not matched by salinity or chloride contents (Fig. 31). Sedimentological descriptions of cores from Unit II indicate the presence of many dewatering structures but these were not seen in Unit IV. However, expulsion of interlayer water from clays during compaction might be sufficient to partly oxidize some sulfide to ferric oxyhydroxide and sulfate if an oxygen source is present. We have no evi-

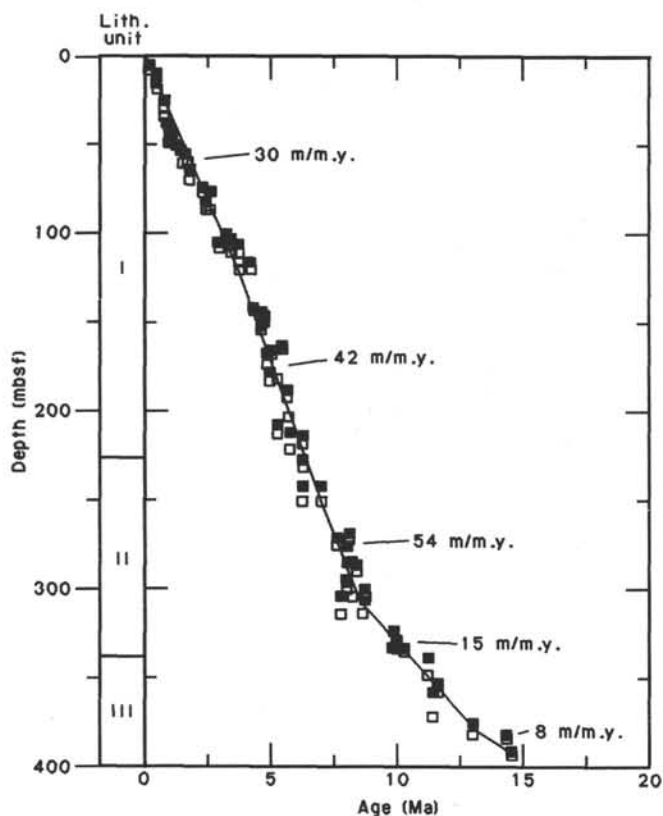


Figure 19. Age-depth plot of Site 722 stratigraphic datums listed in Table 4. The solid and open boxes are the upper and lower depths of each datum level, respectively. Indicated sedimentation rates are based on a best fit to all stratigraphic data. Sedimentation rates calculated between reliable nannofossil datum levels in the top 120 m are listed in Table 7.

dence to support this hypothesis. In addition, this reaction would tend to lower the pH of the interstitial water if the system were closed, which is not observed, and there is sedimentological evidence to support authigenic pyrite formation rather than oxidation. On balance, it would appear that the sulfate increase in depth in Units III and IV may reflect the last vestige of ongoing diffusion of sulfate from seawater originally trapped within the rapidly-accumulating, carbon-poor turbidites. It is clear that any interpretation of the sulfate increase at depth in Units III and IV is based largely on speculation.

Calcium and Magnesium

The profiles of dissolved calcium and magnesium at Site 722 are displayed in Figure 31. In all respects the decrease in Mg^{2+} and increase in Ca^{2+} are identical to Site 721, with precisely the same depth gradients. This is to be expected if the lithology of the substrate plays an important part in maintaining the mass balance of the major ions in the carbonate system. The deeper penetration of Hole 722B indicates that the concentration of Ca^{2+} is still increasing with depth while Mg^{2+} has reached an asymptote of ~ 29 mmol/L. We believe that the carbonate precipitation/dissolution reactions discussed in the Site 721 summary are equally applicable to Site 722.

Ammonia, Phosphate, and Silica

The distribution of these metabolites is displayed in Figure 31. Compared with Site 721, ammonia reaches a maximum concentration of 2.31 mmol/L at 142 mbsf, some 30 m shallower than at the previous site. This depth is consistent with the zone of near sulfate depletion. Below 142 mbsf ammonia removal oc-

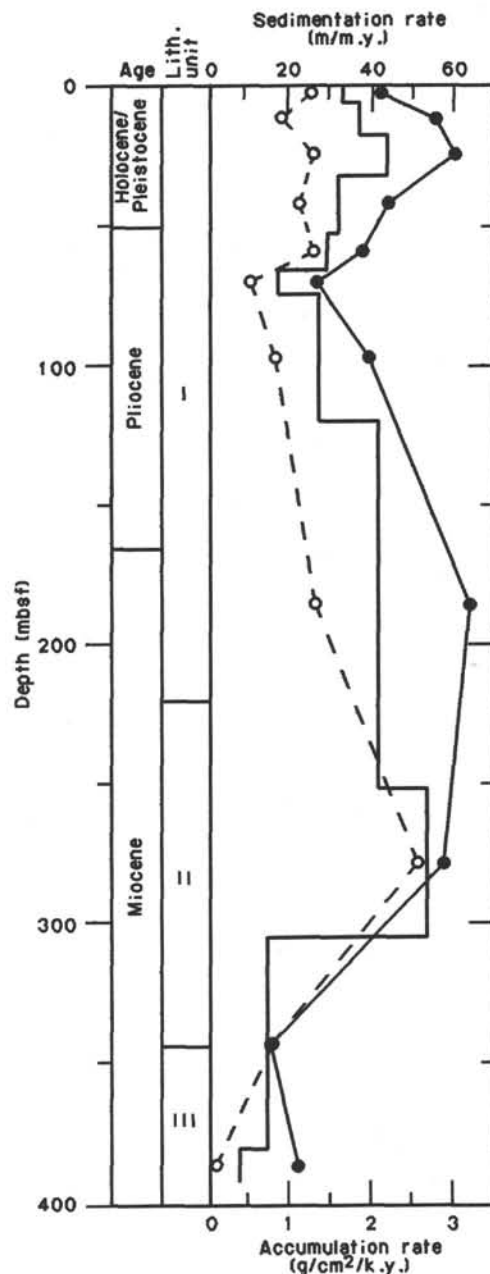


Figure 20. Sedimentation rate (m/m.y., solid line), calcium carbonate accumulation rate ($g/cm^2/k.y.$, dots), and noncarbonate accumulation rate ($g/cm^2/k.y.$, circles) vs. depth (mbsf) at Site 722. Accumulation rates are plotted at the midpoint of the respective depth intervals.

curs, possibly via clay adsorption reactions. Phosphate is rapidly released during organic matter degradation giving a maximum value of $6.49 \mu mol/L$ in Core 117-722A-3H at 25 mbsf. Sequestration of phosphate, which we attribute to apatite formation, occurs throughout the remainder of the hole.

The profile of dissolved silica is very interesting in that it appears to reflect sediment lithology extremely well. Rapid dissolution of biogenic tests occurs over the top 5 mbsf, followed by a more gradual increase to a uniform concentration of ~ 1000 – $1040 \mu mol/L$ for the remainder of Unit I. In Unit II the appearance of diatoms is matched by an increase in dissolved silica, which achieves a maximum of $1257 \mu mol/L$ at 291 mbsf. At the base of the diatom-rich pelagic ooze, silica concentrations rapidly fall to $167 \mu mol/L$ at 404 mbsf within the marly nannofos-

Table 8. Physical properties summary for Hole 722A.

Core, section, interval (cm)	Depth (mbsf)	Wet-bulk density (g/cm ³)	Porosity (%)	Water content (%)	Grain density (g/cm ³)	Dry-bulk density (g/cm ³)	Velocity ^a (m/s)	Vane shear strength (kPa)
117-722A-								
1H-2, 52-54	2.02	1.625	66.0	41.6	2.670	0.948		
1H-4, 52-54	5.02	1.725	62.4	37.1	2.754	1.086		19.1
1H-6, 52-54	8.02	1.616	63.9	40.6	2.545	0.960		
2H-2, 50-52	11.80	1.623	61.7	38.9	2.703	0.991		
2H-4, 50-52	14.80	1.674	63.7	39.0	2.670	1.022		20.4
2H-6, 50-52	17.80	1.672	60.8	37.3	2.554	1.049		
2H-6, 52-55	17.82						^a 1457	
3H-2, 50-52	21.40	1.589	65.6	42.3	2.670	0.917		
3H-4, 50-52	24.40	1.643	63.4	39.6	2.590	0.993		18.1
3H-6, 50-52	27.40	1.562	67.2	44.1	2.527	0.874		
3H-6, 52-55	27.42						^a 1501	
4H-2, 50-52	31.00	1.697	61.3	37.0	2.695	1.070		
4H-4, 50-52	34.00	1.717	60.1	35.8	2.646	1.101		28.5
4H-6, 50-52	37.00	1.611	67.1	42.7	2.642	0.924		
4H-6, 52-55	37.02						^a 1542	
5H-2, 50-52	40.60	1.649	64.5	40.1	2.653	0.988		
5H-4, 50-52	43.60	1.743	59.9	35.2	2.717	1.129		
5H-6, 50-52	46.60	1.649	64.3	40.0	2.633	0.990		
5H-6, 52-56	46.62						^a 1501	
6H-2, 50-52	50.20	1.677	62.3	38.1	2.599	1.039		
6H-4, 50-52	53.20	1.684	60.7	36.9	2.525	1.062		
6H-6, 50-52	56.20	1.733	59.6	35.3	2.599	1.122		
6H-6, 54-57	56.24						^a 1534	
7H-2, 50-52	59.50	1.686	60.1	36.5	2.532	1.070		
7H-4, 50-52	62.50	1.723	61.4	36.5	2.603	1.094		73.1
7H-6, 50-52	65.50	1.732	59.4	35.1	2.595	1.124		
7H-6, 54-57	65.54						^a 1526	
8H-2, 50-52	69.20	1.692	60.3	36.5	2.625	1.074		
8H-4, 50-52	72.20	1.701	59.4	35.8	2.567	1.093		33.8
8H-6, 50-52	75.20	1.711	59.1	35.4	2.543	1.106		
8H-6, 52-55	75.22						^a 1556	
9H-2, 50-52	78.80	1.617	65.7	41.7	2.553	0.943		
9H-4, 50-52	81.80	1.599	63.9	40.9	2.400	0.945		65.4
9H-6, 50-52	84.80	1.656	61.3	37.9	2.470	1.028		
10X-2, 50-52	88.50	1.597	64.3	41.2	2.479	0.938		
10X-4, 50-52	91.50	1.663	64.5	39.7	2.651	1.003		
11X-2, 50-52	98.20	1.661	62.7	38.7	2.503	1.019		
11X-4, 50-52	101.20	1.699	64.0	38.6	2.674	1.043		
11X-6, 50-52	104.20	1.697	61.7	37.3	2.616	1.064		
12X-2, 50-52	107.90	1.696	59.9	36.2	2.514	1.083		
12X-4, 50-52	110.90	1.751	61.5	36.0	2.654	1.121		
12X-6, 50-52	113.90	1.755	61.6	35.9	2.707	1.124		

sil chalk. We consider that the chalk represents an important locus of diagenetic reaction within the cored section. Below this depth silica concentrations increase slightly in the turbidites of Unit IV to 361 $\mu\text{mol/L}$ at the bottom of the hole.

We have attempted to quantify the mass transfer of dissolved to solid-phase silica in Unit III. Assuming a diffusivity of $5 \times 10^{-6} \text{ cm}^2 \text{ s}^{-1}$ and a path length of 50 m, about 1.9 $\text{mg cm}^{-2} \text{ k.y.}^{-1}$ of SiO_2 could be supplied by steady state diffusion. Unit III accumulates at $\sim 3 \text{ cm k.y.}^{-1}$ (see "Accumulation Rates" section, this chapter) giving a total sediment accumulation rate of $\sim 3.6 \text{ g cm}^{-2} \text{ k.y.}^{-1}$. Hence, precipitation of diagenetic silica within this unit accounts for a concentration increase of solid-phase SiO_2 of only 0.05 wt%.

Sediment Mineralogy

The mineralogy of 11 sediment residues from Holes 722A and 722B remaining after interstitial water extraction was determined by X-ray diffractometry. In all cases, CaCO_3 was removed with 10% HCl prior to analysis; the acid treatment was followed by two washes of the insoluble residue with deionized water. The calcium carbonate-free samples were then pipetted onto glass slides as a slurry in acetone and dried at low temperature on a hotplate. Two of the samples were subsequently exposed for several hours to ethylene glycol in a desiccator to check for the presence of expandable clays.

The noncarbonate fraction of the sediments at Site 722 is in general composed of the same suite of minerals found at the nearby Site 721: quartz, feldspar, chlorite (and kaolinite?), and illite and/or mica are common in all samples, while pyrite occurs in trace quantities in most, but not all, of the analyzed residues. The occurrence of pyrite in the sequence appears to be random as no clear patterns of distribution were observed. Dolomite is rare in the residues. We were unable to identify with certainty characteristic dolomite peaks in any of the insoluble residues; this is not the case for bulk carbonate-rich samples and probably reflects the destruction of finely-crystalline dolomite during the acid treatment.

The possible presence of smectite was evaluated by glycolation of samples from Core 117-722B-12X (foraminifer-bearing nannofossil ooze) and Core 117-722B-37X (marly nannofossil chalk). No shift of the $\sim 14 \text{ \AA}$ peak was observed in the nannofossil ooze but a distinct shift of a portion of the 14 \AA peak in the marly chalk to a d-spacing of $\sim 17 \text{ \AA}$ indicated that some smectite is present in lithologic Unit III (see "Lithostratigraphy" section, this chapter). Well-crystallized chlorite, indicated by the presence of sharp peaks at 14, 7, 3.5, and $\sim 2 \text{ \AA}$, is abundant in Unit IV (sandy to silty claystones and turbidites interbedded with nannofossil chalk in the upper part of the sequence). An ultraslow scan of the $24^\circ\text{--}26^\circ$ portion of the diffraction spectrum of a sample of pale-green silty clay from 438 mbsf

Table 8 (continued).

Core, section, interval (cm)	Depth (mbsf)	Wet-bulk density (g/cm ³)	Porosity (%)	Water content (%)	Grain density (g/cm ³)	Dry-bulk density (g/cm ³)	Velocity ^a (m/s)	Vane shear strength (kPa)
117-722A- (Cont.)								
13X-2, 50-52	117.60	1.706	61.7	37.0	2.682	1.074		
13X-4, 50-52	120.60	1.711	64.1	38.4	2.678	1.055		
13X-6, 50-52	123.60	1.724	58.4	34.7	2.443	1.125		
14X-2, 51-53	127.31	1.684	61.6	37.5	2.557	1.0531		
14X-3, 60-63	128.90						^a 1497	
14X-4, 51-53	130.31	1.682	60.8	37.1	2.500	1.059		
15X-2, 60-62	137.00	1.691	62.5	37.8	2.634	1.052		
15X-4, 60-62	140.00	1.703	63.1	37.9	2.717	1.057		62.5
15X-6, 10-13	142.50						^a 1561	
15X-6, 15-17	142.55	1.665	61.3	37.7	2.563	1.037		
16X-2, 52-54	146.62	1.639	62.1	38.8	2.556	1.002		
16X-4, 53-55	149.63	1.662	61.9	38.2	2.517	1.027		
16X-6, 39-42	152.49						^a 1592	
16X-6, 50-52	152.60	1.717	61.4	36.6	2.643	1.088		
17X-1, 108-110	155.38	1.656	62.5	38.7	2.605	1.016		
17X-3, 103-105	158.33	1.713	62.0	37.1	2.727	1.077		
18X-2, 58-60	165.98	1.711	58.8	35.2	2.573	1.108		
18X-2, 60-62	166.00						^a 1560	
18X-6, 58-60	170.20	1.671	63.5	39.0	2.567	1.020		
19X-2, 62-64	175.72	1.694	60.6	36.7	2.532	1.073		
19X-4, 59-61	178.69	1.700	63.1	38.0	2.684	1.053		
19X-6, 58-61	181.68						^a 1607	
19X-6, 62-64	181.72	1.735	58.9	34.8	2.576	1.132		
20X-2, 36-38	185.16	1.703	58.8	35.4	2.559	1.077		
20X-4, 60-63	188.40	1.701	61.0	36.7	2.637	1.101		
21X-1, 57-59	193.57	1.715	62.7	37.5	2.744	1.072		
21X-3, 60-63	196.60	1.690	59.5	36.1	2.543	1.080		^a 1611
22X-2, 52-54	204.72	1.727	59.3	35.2	2.590	1.120		
22X-4, 52-54	207.72	1.747	59.5	34.9	2.679	1.137		
22X-6, 52-54	210.72	1.790	59.8	34.2	2.767	1.178		^a 1594
23X-2, 50-52	214.40	1.702	52.4	31.5	2.647	1.165		
23X-4, 68-70	217.58	1.641	60.6	37.8	2.394	1.021		
23X-6, 38-40	220.28	1.721	58.3	34.7	2.523	1.124		^a 1614
24X-2, 17-19	223.67	1.740	59.1	34.8	2.631	1.135		
24X-4, 50-52	227.00	1.693	60.2	36.5	2.596	1.076		
24X-6, 50-52	230.00	1.742	58.6	34.5	2.605	1.142		^a 1548
25X-1, 50-52	232.20	1.760	58.6	34.1	2.705	1.160		
26X-1, 58-60	242.28	1.633	63.1	39.6	2.514	0.987		^a 1570
27X-2, 29-31	252.79	1.570	65.7	42.9	2.474	0.999		
27X-4, 17-19	255.67	1.662	64.8	39.9	2.574	0.897		^a 1556
29X-1, 37-40	270.77	1.781	59.5	34.3	2.709	1.171		^a 1625

^a Velocity measurement perpendicular to bedding.

showed no indication that kaolinite was present in the sample. The dearth of kaolinite and the high degree of crystallinity of the chlorite in the turbidites suggest that this clastic sequence has the same provenance as the mineralogically-similar Indus Fan deposits cored at Site 720. There is no indication from our data that the turbidites were derived from the Oman margin area.

In and above Core 117-722B-37X (corresponding to lithologic Units I and II), the sediments appear to contain some palygorskite. The diffraction pattern of this mineral is characterized by a principal reflection at about 8.4° two-theta (~10.5 Å), which has the effect of broadening the illite/mica 10 Å peak if both palygorskite and illite are present in the same sample. Most of the residues above and including that from Core 117-722B-37X show diffractograms with broadened 10 Å peaks compared to samples deeper in the hole, and we tentatively suggest that the difference can be attributed to the presence of palygorskite in lithologic Units I and II. This mineral is known to be a common constituent of soils of the Arabian Peninsula and Somali regions (Kolla et al., 1981) and indeed is common in modern sediments on the Oman margin (Kolla et al., 1981). Its apparent occurrence in Site 722 sediments may be due to eolian transport. A similar mechanism was proposed to explain the co-existence of dolomite and quartz at Site 721. The absence of palygorskite in the Unit IV turbidites, indicated by sharp, rather

than broadened, 10 Å peaks, rules out the Oman margin as a significant source area for terrigenous detritus during the early to middle Miocene. This observation is consistent with the conclusions derived above based on the distribution of chlorite.

Illite and/or mica are relatively abundant in all residues studied. We have made no attempt to differentiate between illite, muscovite, and biotite (which have similar diffraction patterns) in this study, but it is clear from the examination of smear slides that both muscovite and biotite are present in at least some samples, notably from the turbidite sequence. Earlier studies (e.g., Kolla et al., 1981) have shown that illite is a major constituent of the clay-sized fraction in the north-central Arabian Sea. It is probable that the ubiquitous 10 Å peak in the diffractograms represents largely muscovite and biotite in lithologic Unit IV and illite in Units I to III.

ORGANIC GEOCHEMISTRY

The organic geochemical parameters routinely determined on sediments of Holes 722A and 722B were the abundance of organic carbon and pyrolysis characteristics of organic matter in headspace residues. In addition, closely spaced samples (spacing of about 5 cm) were taken across two examples of cyclic sedimentation in upper Miocene nannofossil oozes and muds typical of lithologic Units I and II. Color changes in these cycles

Table 9. Physical properties summary for Hole 722B.

Core, section, interval (cm)	Depth (mbsf)	Wet-bulk density (g/cm ³)	Porosity (%)	Water content (%)	Grain density (g/cm ³)	Dry-bulk density (g/cm ³)	Velocity (m/s)
117-722-							
1H-3, 50-52	3.50	1.654	62.7	38.8	2.566	1.012	
2H-3, 50-52	9.00	1.552	70.6	46.6	2.675	0.829	
3H-3, 50-52	18.60	1.623	66.6	42.0	2.641	0.941	^a 1465
4H-3, 50-52	28.20	1.644	61.7	38.4	2.597	1.013	^a 1556
5H-3, 50-52	37.80	1.607	65.6	41.8	2.694	0.935	^a 1547
6H-3, 50-52	47.40	1.646	64.7	40.3	2.678	0.983	^a 1545
7H-3, 50-52	56.70	1.708	62.3	37.4	2.675	1.070	^a 1555
8H-3, 50-52	66.40	1.650	63.0	39.1	2.622	1.005	^a 1522
9H-3, 50-52	76.00	1.727	62.1	36.8	2.699	1.091	^a 1508
10H-3, 50-52	86.20	1.661	62.1	38.3	2.617	1.025	^a 1549
11X-3, 92-94	95.82	1.669	59.7	36.6	2.542	1.058	^a 1559
12X-3, 17-19	104.67	1.714	60.3	36.1	2.661	1.096	^a 1625
13X-3, 29-31	114.49	1.703	57.3	34.5	2.684	1.116	
14X-3, 46-48	124.36	1.707	60.2	36.1	2.583	1.091	^a 1592
16X-3, 50-52	143.70	1.668	61.0	37.5	2.480	1.043	
17X-3, 50-52	153.40	1.685	63.7	38.7	2.532	1.032	
18X-3, 52-54	163.02	1.719	61.2	36.5	2.656	1.093	^a 1604
19X-5, 112-114	176.32	1.762	59.6	34.6	2.680	1.152	^a 1612
20X-2, 74-76	181.14	1.731	59.4	35.1	2.528	1.123	^a 1625
21X-3, 66-68	192.16	1.692	60.7	36.8	2.521	1.070	^a 1626
22X-3, 51-54	201.71	1.688	59.9	36.4	2.522	1.074	^a 1616
23X-3, 45-48	211.35	1.730	59.7	35.4	2.546	1.118	^a 1535
24X-3, 50-53	221.00	1.754	60.5	35.3	2.682	1.135	^a 1529
25X-6, 43-47	235.13	1.750	58.4	34.2	2.589	1.152	^a 1597
26X-5, 21-23	243.11	1.665	64.1	39.5	2.646	1.008	^a 1601
27X-4, 40-42	251.40	1.756	61.0	35.6	2.703	1.131	^a 1571
28X-2, 47-49	258.17	1.699	60.5	36.5	2.624	1.079	
29X-3, 60-62	269.50	1.572	69.8	45.5	2.610	0.857	^a 1507
31X-2, 50-52	287.30	1.630	66.1	41.5	2.677	0.953	
31X-4, 50-52	290.30	1.670	60.5	37.1	2.506	1.051	^a 1535
31X-6, 50-52	293.30	1.730	62.0	36.7	2.696	1.095	
32X-2, 50-52	297.00	1.669	59.7	36.6	2.610	1.057	
32X-4, 50-52	300.00	1.609	64.7	41.2	2.528	0.946	
33X-2, 28-31	306.48	1.461	74.3	52.1	2.551	0.700	^a 1583
34X-2, 80-82	316.60	1.422	75.5	54.4	2.299	0.648	^a 1541
34X-2, 80-82	316.60						1614
34X-4, 40-42	319.20	1.439	70.5	50.2	2.354	0.717	
35X-2, 52-54	326.02	1.688	61.0	37.0	2.539	1.063	
35X-4, 51-53	329.01	1.568	69.1	45.2	2.722	0.860	^a 1587
35X-4, 51-53	329.01						1634
35X-6, 50-53	332.00	1.662	63.2	39.0	2.615	1.015	^a 1580
35X-6, 50-53	332.00						1611
36X-2, 48-50	335.68	1.720	62.9	37.5	2.742	1.075	^a 1600
36X-2, 48-50	335.68						1617
36X-4, 77-79	338.97	1.637	63.7	39.8	2.630	0.985	^a 1614
36X-4, 77-79	338.97						1653
37X-2, 51-53	345.41	1.796	55.9	31.9	2.747	1.224	^a 1616
37X-2, 51-53	345.41						1639
37X-4, 51-53	348.41	1.756	55.6	32.5	2.601	1.186	^a 1646
37X-4, 51-53	348.41						1710
37X-6, 50-52	351.40	1.790	58.2	33.3	2.732	1.194	^a 1605
37X-6, 50-52	351.40						1643
38X-2, 71-73	355.31	1.740	60.5	35.6	2.755	1.120	^a 1631
38X-2, 71-73	355.31						1668
38X-4, 83-85	358.43	1.781	56.0	32.2	2.648	1.207	
38X-6, 52-54	361.12	1.802	56.8	32.3	2.764	1.219	^a 1658
38X-6, 52-54	361.12						1696
39X-1, 12-14	362.92	1.855	54.2	29.9	2.762	1.300	^a 1676
39X-1, 12-14	362.92						1736
39X-CC, 8-10	365.45	1.821	53.6	30.2	2.723	1.272	^a 1673
39X-CC, 8-10	365.45						1734
40X-3, 16-18	375.66	1.912	49.6	26.6	2.737	1.404	^a 1637

(about 1 m thick) correlate with changes in abundance of major sediment components, as well as with variations in physical, magnetic, and chemical properties of the sediments (see "Lithostratigraphy," "Physical Properties," and "Paleomagnetism" sections, this chapter). By investigating detailed transects across two of these cycles, we hoped to shed light on variations in organic-matter abundance and origin, as well as on organic-matter diagenesis. Such detailed studies are a prerequisite for identifying characteristics of the cyclic sedimentation pattern, which

is presumed to be the sedimentary expression of recurring changes in monsoonal induced upwelling.

Organic Carbon Abundance and Character

Sediments of lithologic Units I, II, and III are characterized by alternating sequences of organic-carbon-rich sediments and sediments with less organic carbon (about 2% and <0.5% organic carbon by weight, respectively; see Table 3). Organic-carbon-rich layers coincide with dark green coloration and lower

Table 9 (continued).

Core, section, interval (cm)	Depth (mbsf)	Wet-bulk density (g/cm ³)	Porosity (%)	Water content (%)	Grain density (g/cm ³)	Dry-bulk density (g/cm ³)	Velocity (m/s)
117-722- (Cont.)							
40X-3, 16-18	375.66						1649
41X-2, 29-31	383.99	2.023	44.6	22.6	2.710	1.566	^a 1943
41X-2, 29-31	383.99						2063
42X-1, 22-24	392.02	1.972	44.6	23.2	2.675	1.515	^a 1761
42X-1, 22-24	392.02						1859
42X-3, 33-35	395.13	1.920	48.3	25.8	2.803	1.425	^a 1627
42X-3, 33-35	395.13						1643
43X-1, 40-42	401.80	1.981	44.3	22.9	2.634	1.527	^a 1902
43X-1, 40-42	401.80						2022
43X-3, 23-25	404.63	1.847	44.8	24.8	2.723	1.388	^a 1648
43X-3, 23-25	404.63						1677
44X-2, 38-40	412.98	2.135	39.8	19.1	2.796	1.727	^a 1759
44X-2, 38-40	412.98						1768
44X-4, 17-19	415.77	1.862	38.2	21.0	2.832	1.470	^a 1701
44X-4, 17-19	415.77						1744
45X-2, 23-25	422.53	1.980	46.9	24.3	2.748	1.499	^a 1564
45X-2, 23-25	422.53						1577
45X-4, 27-29	425.57	2.003	45.3	23.2	2.683	1.538	^a 1713
45X-4, 27-29	425.57						1751
45X-6, 138-140	429.68	1.990	47.1	24.2	2.729	1.508	^a 1703
45X-6, 138-140	429.68	1.990					1706
46X-2, 2-4	432.02	1.970	42.8	22.3	2.735	1.531	^a 1748
46X-2, 2-4	432.02						1692
46X-4, 141-143	436.41	1.970	46.8	24.4	2.685	1.490	^a 1651
46X-4, 141-143	436.41						1688
46X-6, 132-134	439.32	2.002	57.1	29.2	2.624	1.417	^a 1771
46X-6, 132-134	439.32						1706
48X-1, 33-35	450.13	2.008	47.7	24.4	2.802	1.519	^a 1614
48X-1, 33-35	450.13						1633
49X-1, 40-43	459.80	1.957	48.7	25.5	2.753	1.458	^a 1598
49X-1, 40-43	459.80						1586
49X-4, 40-43	464.30	2.000	46.4	23.8	2.788	1.525	^a 1579
49X-4, 40-43	464.30						1577
50X-2, 39-41	470.89	1.884	43.3	23.6	2.781	1.440	^a 1589
50X-2, 39-41	470.89						1617
50X-4, 30-32	473.80	1.976	45.2	23.4	2.701	1.513	^a 1612
50X-4, 30-32	473.80						1635
51X-1, 68-70	479.28				2.793		
52X-2, 79-81	490.49	2.023	45.1	22.9	2.796	1.560	
52X-5, 54-56	494.74	1.793	36.7	21.0	2.719	1.417	^a 1647
52X-5, 54-56	494.74						1666
52X-7, 8-10	497.28	2.041	42.2	21.2	2.694	1.609	^a 1689
52X-7, 8-10	497.28						1810
53X-1, 41-43	498.31	2.049	43.8	21.9	2.752	1.600	^a 1609
53X-1, 41-43	498.31						1607
55X-1, 4-6	517.24	2.714	11.6	4.4	2.794	2.595	^a 3620
55X-1, 4-6	517.24						4093
56X-CC, 20-22	527.10						^a 3852
56X-CC, 20-22	527.10						4139
57X-1, 79-81	537.39	2.070	41.3	20.4	2.784	1.647	^a 1683
57X-1, 79-81	537.39						1699
58X-1, 134-136	547.54	2.090	38.1	18.7	2.663	1.700	^a 1743
58X-1, 134-136	547.54						1730
58X-3, 74-76	549.94	2.063	42.1	20.9	2.740	1.631	
58X-5, 76-78	552.96	2.009	43.9	22.4	2.683	1.560	^a 1697
58X-5, 76-78	552.96						1808
59X-CC, 12-14	556.86	2.042	42.4	21.3	2.691	1.607	^a 1676
59X-CC, 12-14	556.86						1723

^a Velocity measurement perpendicular to bedding; others measured parallel to bedding

carbonate concentrations, even though direct correlation of CaCO₃ and organic carbon yields a statistically insignificant correlation coefficient of only -0.32. Average organic carbon concentration in the pelagic sediments of sedimentary Units I-III is 1.2% by weight, with a rather large standard deviation of about ± 0.9%. As will be shown below, these large variations occur within individual couplets of dark green and light sediments. Sediments from lithologic Unit IV are lean in organic carbon (average 0.15 with ± 0.1%), with the exception of a distinct coal layer in the core catcher of Core 117-722B-51X, an allochthonous component of a turbidite layer.

The organic matter is immature as shown by the uniformly low temperatures of maximum pyrolysis release of hydrocarbons, T_{max} < 435°C (Table 11). Most samples plot in the field of immature marine organic matter on the hydrogen index/oxygen index diagram (Fig. 32), but show a considerable scatter. A similar kind of scatter was also noticed in Site 721. Samples with a low organic carbon content (< 0.5%) show unusually high oxygen indices (Table 11), which may either be an attribute of immature organic carbon with abundant oxygen-bearing functional groups, or, more likely, due to an artifact of calculating the index (see "Explanatory Notes" chapter, this volume). Even

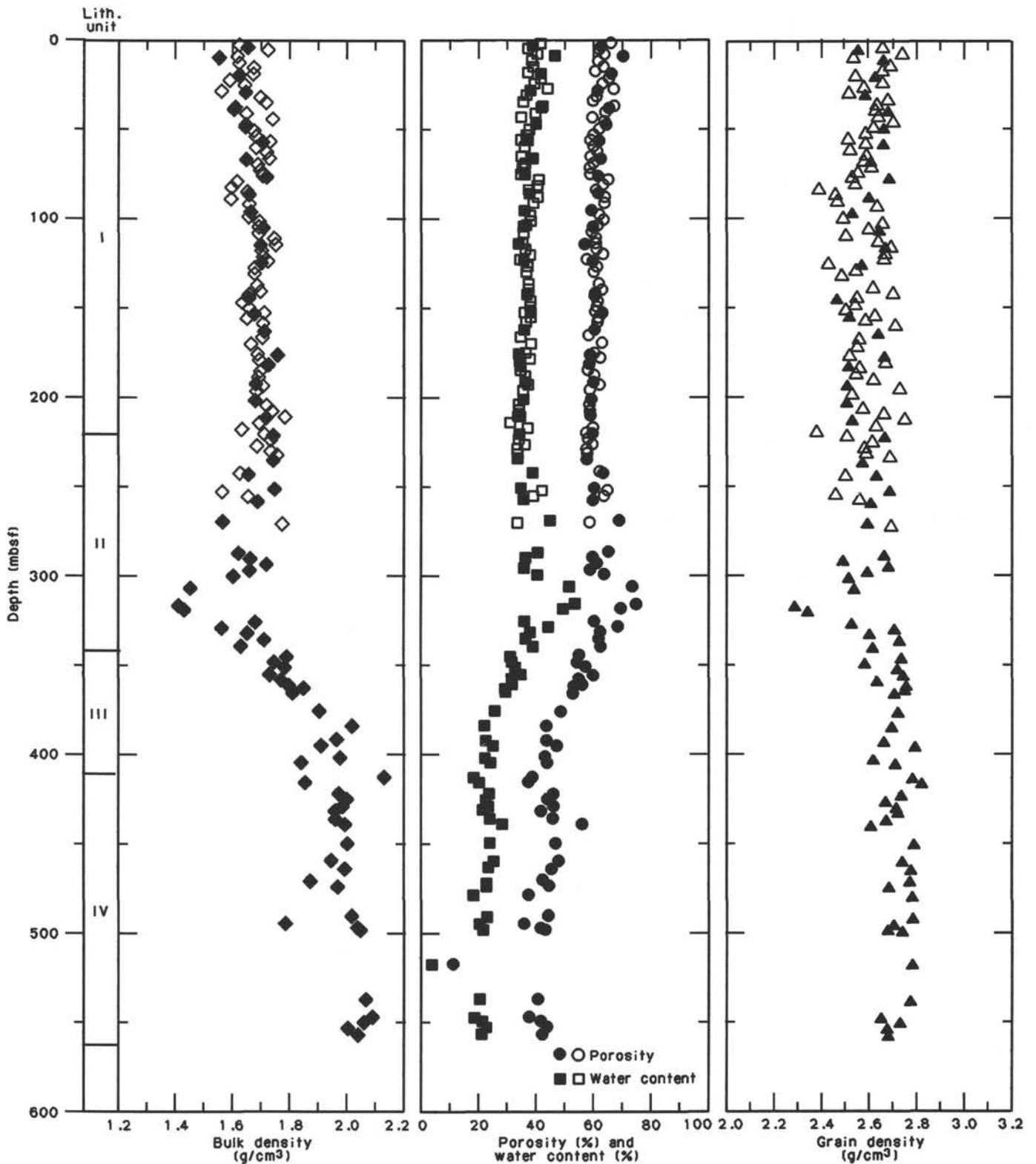


Figure 21. Index properties (wet-bulk density, porosity, water content, and grain density) measured on discrete samples for Holes 722A (open symbols) and 722B (solid symbols).

though we are aware that traditional evolutionary paths given in the van-Krevelen-type (Tissot and Welte, 1984) diagram depicted in Figure 32. do not apply for immature marine organic matter rich in lipids—they were established for kerogens of different provenance—results of S₂, S₃, and TOC as well as derived pa-

rameters may well be meaningful and are suitable to describe properties of immature and lipid-rich sedimentary organic matter.

If samples of Core 117-722A-16X and 117-722B-29X for instance are plotted on the HI/OI diagram (Fig. 32), they cluster

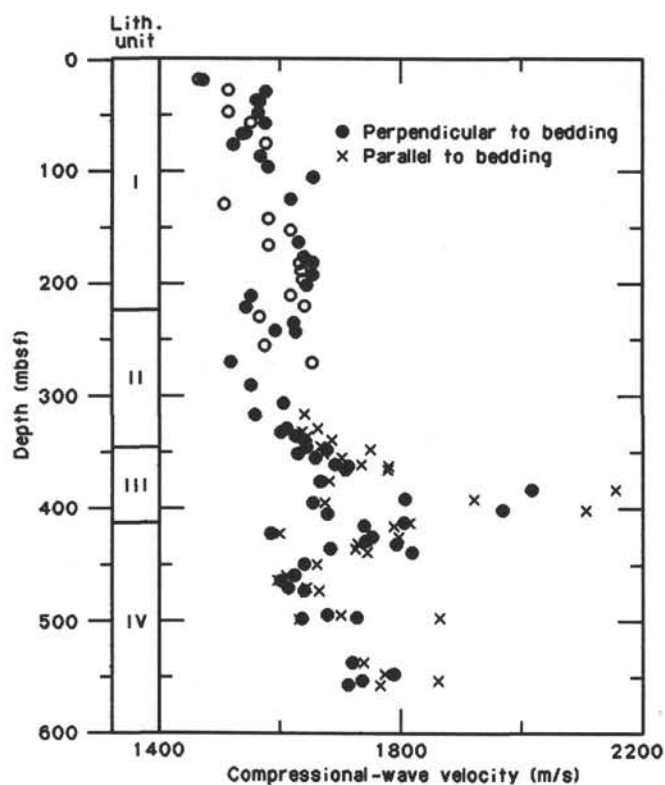


Figure 22. Compressional-wave velocity as measured on discrete samples in the Hamilton Frame Velocimeter in Holes 722A (open symbols) and 722B (solid symbols).

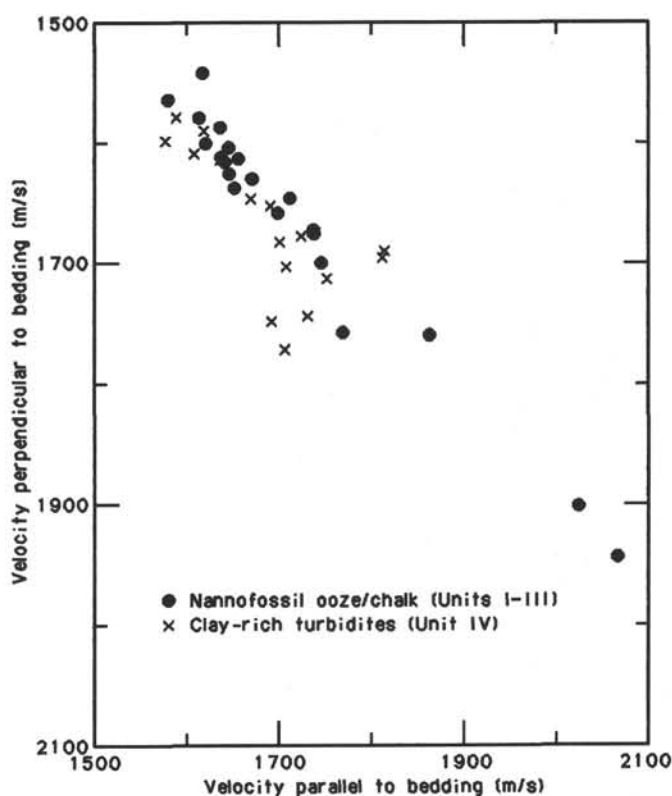


Figure 24. Crossplot of compressional-wave velocity measured perpendicular and parallel to bedding on discrete samples from Hole 722B.

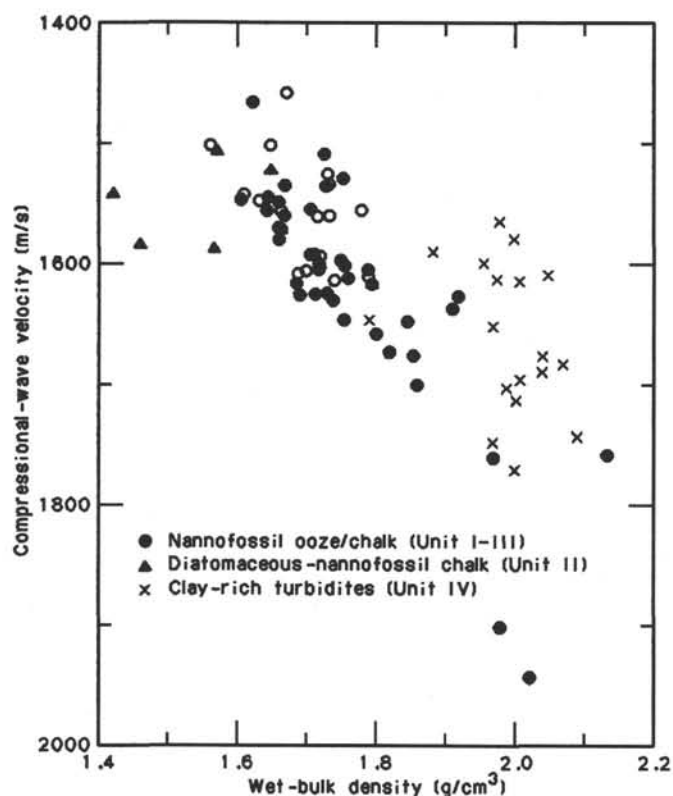


Figure 23. Wet-bulk density vs. compressional-wave velocity measured on discrete samples of nannofossil ooze/chalk, diatomaceous-nannofossil chalk, and clay-rich turbidites in Holes 722A (open symbols) and 722B (solid symbols).

in two distinct areas of the diagram. The only exception is a data point of Core 117-722A-16X that may be dubious because of an unusually high (and possibly false) organic carbon value (and therefore a low hydrogen and oxygen index). With increasing maturation—loss of functional groups and increasing polycondensation either by thermal or diagenetic processes—organic matter releases progressively less hydrocarbons (S_2) and CO_2 (S_3). It is conceivable that samples from Core 117-722A-16X, from approximately 150 mbsf and an age of approximately 6 Ma, contain more oxygenated compounds than those of Core 117-722A-29X at 270 mbsf and several million years older. In the older samples, diagenesis may be more advanced and may have stripped the organic matter of oxygenated components. Another explanation could be that the dominant type of input changed from more hydrogen-rich (proteins, lipids) to more oxygen-rich (sugars) material. In both cases, the organic matter is primarily of marine origin. Two analyses of the same coal sample from sedimentary Unit IV are denoted "C" in Figure 32.

Detailed Sample Series across Sections 117-722A-16X-2 and 117-722B-29X-3, -4

A strong negative correlation was observed for calcium carbonate vs. organic carbon abundances in the two detailed sample series (Figs. 33 and 34). While the two signals follow each other closely in Core 117-722A-16X (Fig. 33), they show a considerable time lag in Core 117-722B-29X (Fig. 34). In the case of samples from Core 117-722A-16X, the response of the carbonate preservation or production to a postulated change in the sedimentary environment appears to precede enhanced production or preservation of the organic matter (compare Figs. 33 and 34). A good correlation was observed between the organic carbon content and the HI of the organic matter in both sample suites. The absolute values of the HI, however, are slightly higher in Core 117-722B-29X as compared to Core 117-722A-16X.

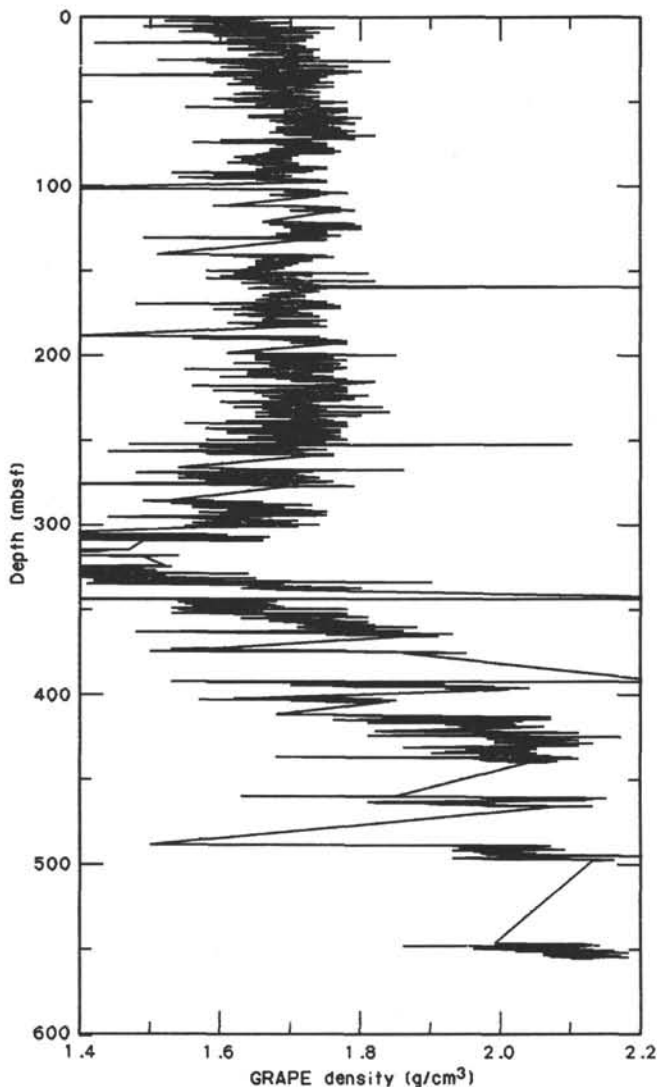


Figure 25. GRAPE wet-bulk density for Hole 722B. The profile is based on 10-cm-block averages of the data.

Enhanced primary productivity of relatively lipid- and therefore hydrogen-rich marine tissue seems to be a likely reason for the observed pattern. A puzzle remains the nature of the dominating primary producer in times corresponding to the organic-rich, carbonate-poor intervals, because neither diatoms nor coccolithophorids are likely candidates for lack of both opal and carbonate in the sediments. If input of organic carbon was constant and from the same source organisms, the higher HI in the deeper samples implies that preservation of organic matter was better during time of deposition.

Hydrocarbon Gases

Abundance of interstitial gas was determined in sediments adjacent to routine organic geochemical samples following the procedure outlined in the "Explanatory Notes" chapter (this volume). Gas concentrations, when compared to the previous site on the Owen Ridge, are extremely low (< 800 µL/L sediment). If the data are to be trusted, then biogenic methane is the dominating hydrocarbon gas, with only trace quantities of ethane (<5 µL/L sediment) occurring in three samples (see Table 12). A viable reason for low rates of bacterial methane production may be the fact that interstitial sulfate, a limiting factor for bac-

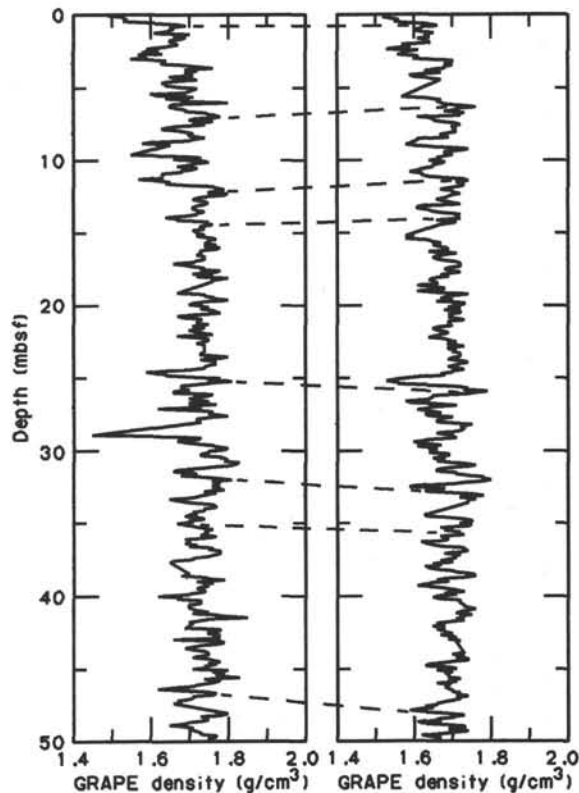


Figure 26. GRAPE wet-bulk density for 0–50 mbsf in Holes 721B (left) and 722B (right). The profiles are based on 10-cm-block averages of the data.

terial methane production, is not completely depleted throughout most of the section. In the deepest samples (see "Inorganic Geochemistry" section, this chapter), sulfate concentrations even appear to increase. The persistent occurrence of sulfate, except in samples between approximately 250 and 290 mbsf, may thus be the reason for the abnormally low methane abundances. Thermal maturity of the organic matter in all sedimentary units is low, so that thermogenic gas was not expected. The occurrence of coal layers in sedimentary Unit IV, in particular of a thick seam in Section 117-722B-51X-CC, is attributable to the turbiditic nature of the sediments in this unit. The coal was most likely redeposited after exhumation from a nearshore or shelf sediment.

DOWNHOLE MEASUREMENTS

Operations

Logging operations at Hole 722B began at 1314 on 11 September, with a hole conditioning program similar to that used at Site 720. The Schlumberger seismic stratigraphic combination, wireline heave compensator, and sidewall entry sub (SES) were rigged up between 2215 and 0200 on September 12. The SES was used because tests of capillary suction time (CST) indicated a moderate to high potential for clay swelling in the bottom 150 m of the hole (CST values of 80 to 150 s for mud salinity of 29 g/kg). The drill-pipe heave compensator was used during logging to reduce the possibility of pipe bending.

The seismic stratigraphic combination was run between 0200 and 0545. At Site 722 this tool string consisted of the analog borehole-compensated sonic tool, gamma ray tool, and dual induction resistivity (see "Explanatory Notes" chapter, this volume). Logs were obtained both downgoing and upcoming, from

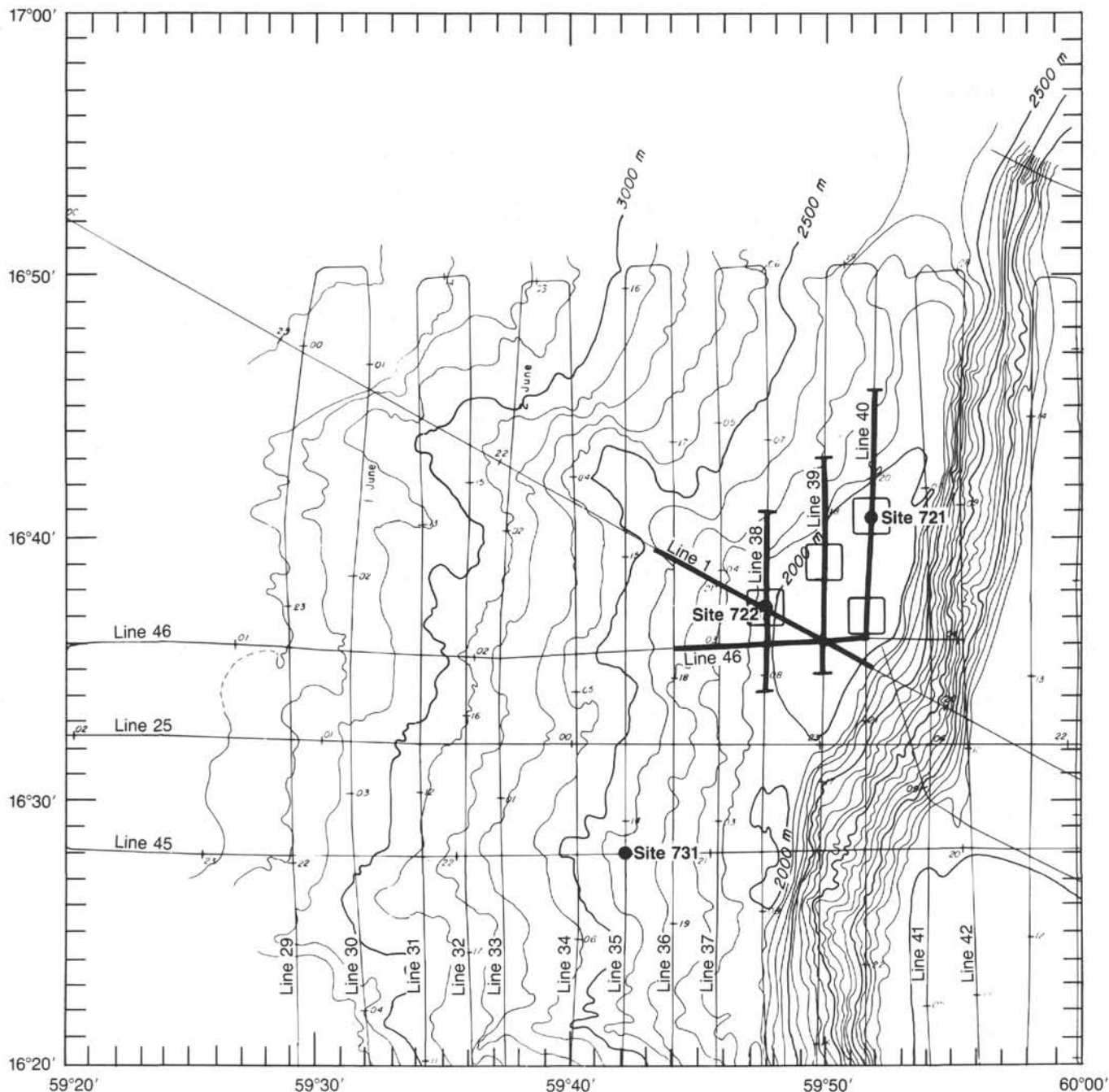


Figure 27. The location of Sites 721 and 722 and the SCS tracks used to establish the seismic stratigraphy of the Owen Ridge. Intervals used are shown as heavy lines and the boxes indicate portions of the tracks shown in Figures 28 and 29. The bathymetry is based on Sea Beam data from the Leg 117 site survey (RC2704, 1986).

just beneath the base of pipe (94.3 mbsf) to 555.5 mbsf. Very little fill was found at the bottom of the hole (total drilled depth 565.1 mbsf), and no bridges were encountered. The wireline heave compensator failed and was shut off shortly after beginning logging up.

The second tool string run was the Schlumberger lithoporosity combination. At Site 722 this tool string consisted of the spectral gamma ray, neutron porosity, lithodensity, and GPIT accelerometer tools (see "Explanatory Notes" chapter, this volume). At 0915 this tool string started down for the first time, but the run was aborted because of an electrical short only 300 m below the ship. Upon rigdown, the cause of the short was found to be a badly twisted pigtail at the cable head. This twisting was caused by rotating the SES to connect it to pipe; the bowspring

on the density tool prevented the tool string from rotating along with the SES. The pigtail was replaced, and a swivel was installed in the tool string to prevent a recurrence of the twisting problem. However, the second run of the tool string downhole failed at 700 m below the ship, due to a short in the swivel. The swivel was removed, the SES was rigged down, and a wiper trip was made to break up any possible bridges.

The third run of the lithoporosity combination, from 1900 to 2325, was much more successful. Nearly the entire open-hole interval (94.2–539.9 mbsf) was logged going down. While logging up, pipe was raised 20 m, so that open-hole logs were obtained between 71.4 and 550.9 mbsf. However, the upper bowspring on the density tool would not collapse sufficiently to enter the pipe. Therefore it was necessary to deploy the crimper and cutter

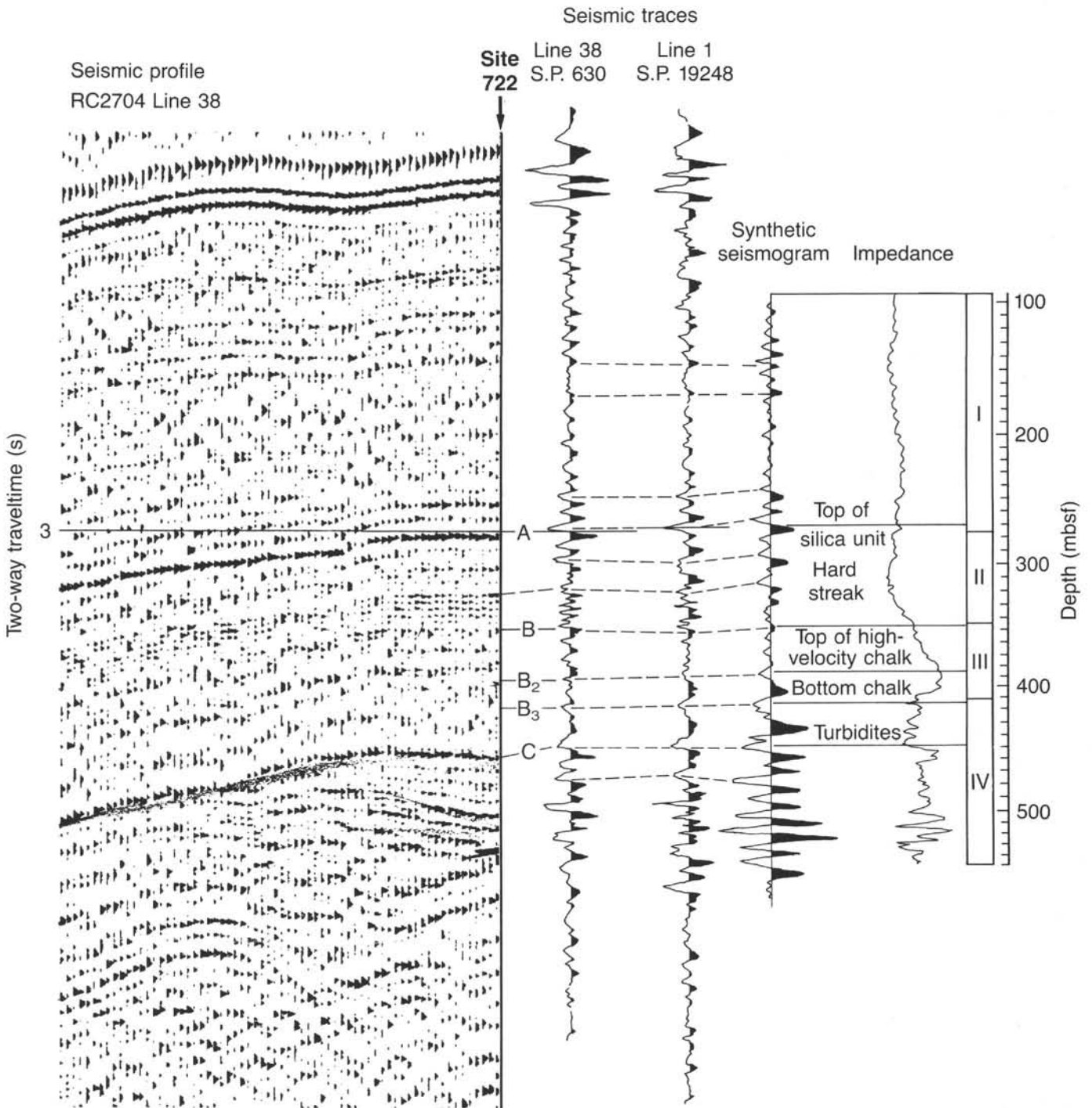


Figure 28. Correlation of reflectors (see text for discussion) between seismic profiles and with the synthetic seismogram, which is based on logging data from Site 722 (see "Downhole Measurements" section, this chapter). Synthetic seismogram is scaled in mbsf and seismic profiles are in two-way traveltme (s).

tools, to cut the wireline. A minicone was made up and dropped, to permit reentry and cementing of the hole in case the tool string was not retrieved. The crimper and cutter worked successfully; after the drill string was pulled, the tool string was retrieved with the bottom-hole assembly.

Log Quality and Editing

Several logs from Site 722 required a substantial amount of editing to improve their initially fair-to-poor quality. Editing or reprocessing was undertaken for sonic, resistivity, density, and

gamma ray logs. After editing, the quality of nearly all logs was very good.

Sonic logging at Site 722 utilized a borehole compensated tool (BHC). This backup tool is less reliable in high-porosity sediments than the normal long-spaced sonic (LSS) because of its short source-receiver spacing. At each depth, two short-spaced (0.9 m) and two medium-spaced (1.5 m) source-receiver combinations are used. The upcoming log had only one cycle skip on one short-spaced pair, but this shift at 179 mbsf causes a substantial baseline shift in sonic transit times (Fig. 35). The down-

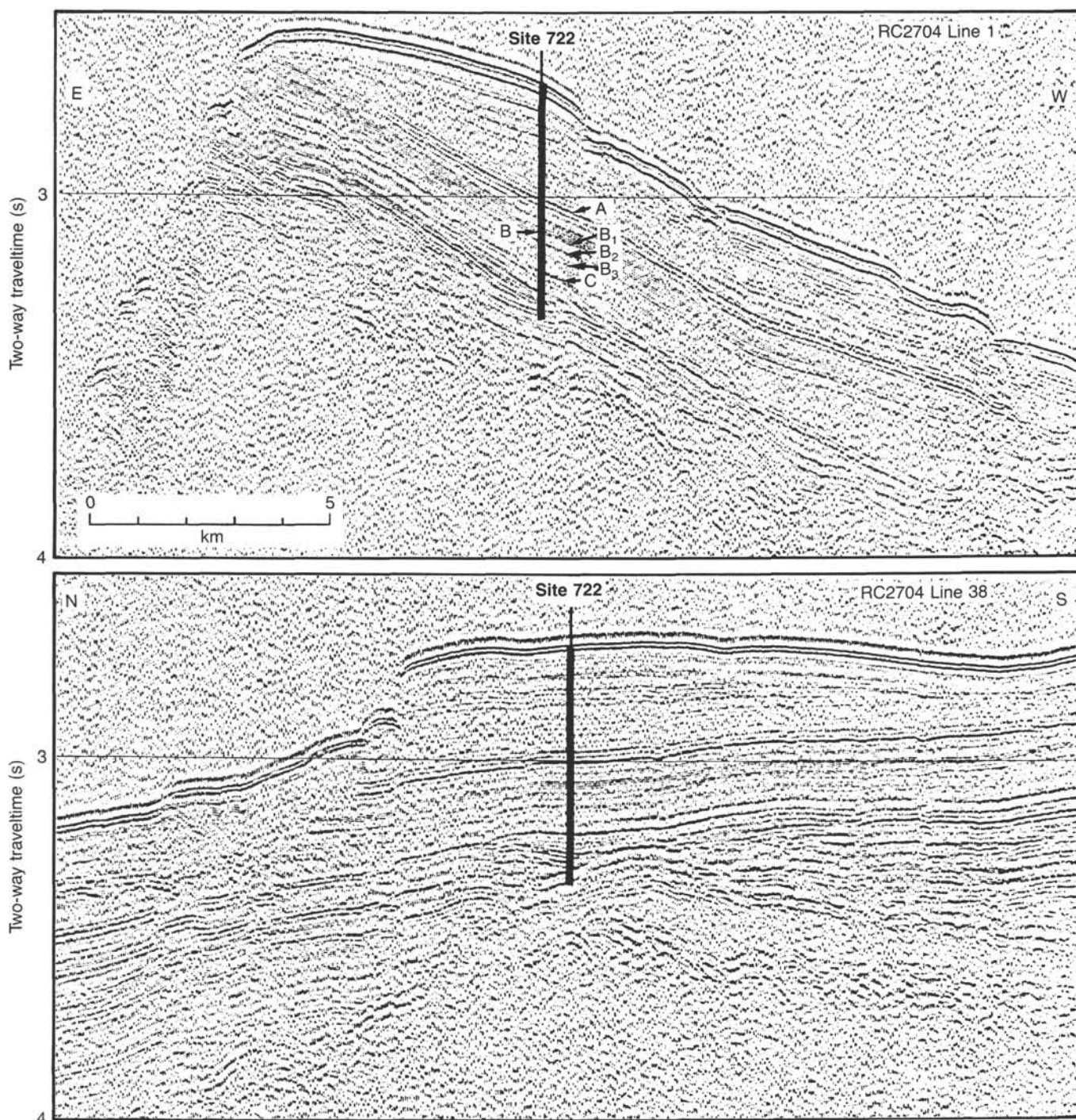


Figure 29. Seismic reflection profile (Lines 1 and 38, Fig. 27) across Site 722 to the crest of the Owen Ridge. The location and recovered interval of Site 722 are shown, along with the reflector identifications.

going log was much less reliable, with cycle skips on all channels, probably because of the much faster logging speed. Raw sonic transit times for the downgoing log are much slower than in water in the interval above 163 mbsf (Fig. 35). No cycle skipping is observed in either log below 275 mbsf.

Cycle skips were removed from both downgoing and upcoming source-receiver transit times, by simply removing all sudden baseline shifts. The edited transit times were then reprocessed, to increase vertical resolution to 0.6 m and exclude unreliable data according to an algorithm described by Shipboard Scientific Party (1987). Figure 35 shows an overlay of the downgoing

and upcoming reprocessed sonic logs. The two agree quite well throughout the depth range. Comparing the reprocessed logs to the raw logs, very little change is observed below 275 mbsf, but the interval above this depth is substantially revised. In particular, the slowest values are now $193 \mu\text{s}/\text{ft}$ ($1.58 \text{ km}/\text{s}$), in contrast to raw sonic values slower than $210 \mu\text{s}/\text{ft}$ ($1.45 \text{ km}/\text{s}$). For comparison, an empirical curve of velocity as a function of depth for calcareous sediments predicts velocities of about $1.7 \text{ km}/\text{s}$ at 100 mbsf (Hamilton, 1979).

Downhole resistivity log calibrations were poor prior to resistivity logging. Because of time constraints, resistivity logging

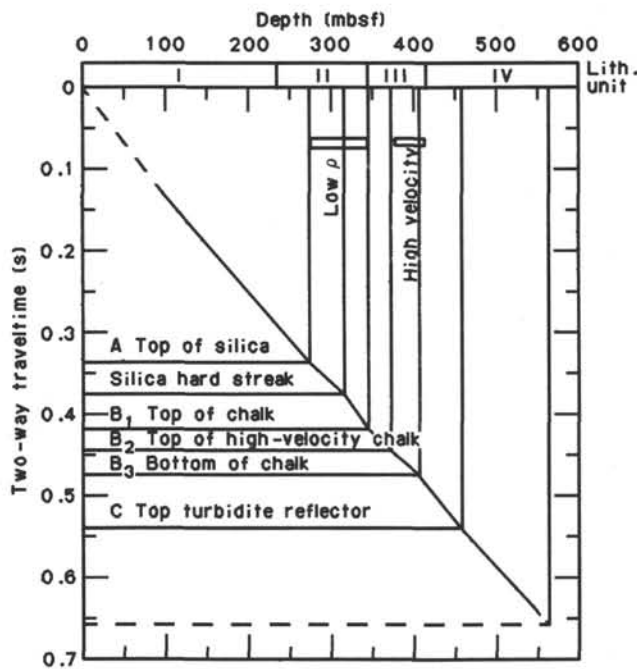


Figure 30. Plot of two-way traveltime (from SCS line 38, see Figs. 28 and 29) and depth (mbsf) of lithologic features at Site 722. Reflectors are indicated on the traveltime axis, and lithologic units and facies are shown on the depth axis.

was undertaken anyway. During downgoing logging, the gain of the spherically-focused resistivity was adjusted twice, and the gains of medium and deep resistivity logs were each adjusted once. At the conclusion of upcoming logging, the resistivity calibration was good. The gain adjustments apparently solved the calibration problem, while causing step-function changes in the downgoing logs which we have subsequently removed.

The upgoing and downgoing resistivity logs are very similar except in one aspect: the spherically-focused resistivity in the chalks (above 400 mbsf) is relatively constant as a function of depth in the downgoing log, but higher and increasing uphole in the upcoming log. We do not know why this log reads much higher than the two other resistivity logs in the chalks, yet similar to them in the turbidites. We suspect that the spherically-focused log is not properly calibrating in the chalks; at Site 731 this log agreed with the other resistivity logs in this same formation (see "Downhole Measurements" section, "Site 731" chapter, this volume). The higher variance in the spherically-focused log is expected, because it has both higher vertical resolution and lower signal-to-noise ratio than the deeper resistivity logs.

The only editing applied to the gamma ray log was the removal of pipe attenuation effects from the portion of downgoing log obtained through the bottom-hole assembly, 57–91 mbsf. Based on comparison of the mean gamma ray response for a 10-m interval inside pipe with a 10-m interval just below the gamma ray spike at 92–93 mbsf, a gain factor of 4.4 was applied to the through-pipe log (Fig. 36). Comparison of this edited log with the reprocessed spectral gamma ray log shows a fair agreement in the open-hole interval and poor match in the portion for which the gamma ray log was obtained through pipe. The assumption of similar true means above and below the gamma ray spike at 92 mbsf, though appropriate when editing a log independent of other logs, is shown to be invalid by the spectral gamma ray log. In the open-hole interval below 91 mbsf, a character match of large-scale features is found between gamma ray and spectral gamma ray, but the smallest-scale features are not replicated. The open-hole upcoming gamma ray log is similar to

the other two logs, with greatest similarity of small-scale features to the spectral gamma ray log. In the interval for which gamma ray data were collected through pipe and spectral gamma ray data were collected in the open hole, no character match at all is found.

These differences between gamma ray logs are largely attributable to logging speeds. The downgoing gamma ray log was obtained at 1200 m/hr, the upcoming log at 550 m/hr, and the spectral gamma ray log at 300 m/hr. With faster logging speed, the counting statistics of natural gamma radiation decrease in accuracy. With the fastest logging speed, the accuracy is apparently about 2–5 API units, comparable in magnitude to the formation variations in signal strength for through-pipe logging at this site. Much higher replicability of repeat runs was obtained for gamma ray logs obtained at lower logging speeds in more radioactive formations at Site 723 (see "Downhole Measurements" section, "Site 723" chapter, this volume).

The density log for Site 722 was adversely affected by voltage fluctuations in the neutron tool. "Corrected" density values, based on the difference between signal strength at two receivers, were nearly all negative. However, after removal of the extremely large hole-size correction (DRHO) that had been applied by the acquisition software and removal of a 0.4-g/cm³ baseline shift at 265 mbsf in the downgoing log, resulting density values exhibited reasonable replication of downgoing and upcoming runs (Fig. 37). An exception is the upper turbidite interval, 410–545 mbsf. In general, these density logs are consistent with laboratory measurements of density (see "Physical Properties" section, this chapter). Unfortunately, this omitted DRHO correction is normally useful in removing the adverse effects of variations in quality of tool padding against the borehole wall. Thus the "uncorrected" density log that we must use for Site 722 is sensitive to washouts, enlarged portions of the hole.

An extreme example of this sensitivity is shown in Figures 37 and 38. The upcoming density log exhibits low densities and a strong cyclicity in the interval 130–230 mbsf. This cyclicity is not found in any other log (Figs. 37 and 38), including the downgoing density log. Calculation of apparent matrix (or grain) density from the density and neutron logs yields excursions of matrix density to unrealistically low values of 2.0–2.2 in the cyclical density lows. In contrast, the cyclical density highs give matrix densities that are both more reasonable (2.6–2.7) and more similar to the flanking depth intervals. The cyclical density lows are unreliable, because of borehole enlargement. The periodicity of the density cycles is about 9.2 m, very close to the 9.4 m interval at which cores are taken. Further, the core breaks occur at the density minima (Fig. 38). These density lows are probably caused by the circulation that is used to pump the core barrel down the pipe, while the pipe is stationary. Below 230 mbsf the formation is apparently strong enough to prevent hole washout associated with this pumping. We do not know why this cyclical pattern of apparent density fluctuations is not evident on the downgoing density log.

Post-cruise reprocessing of the density logs yielded logs even less reliable than the corrected logs of Figure 37. Our best estimate of density variations at Site 722 is a composite log consisting of the downgoing log above 231 mbsf and upcoming log below that depth. The reliability of this log is judged to be fair.

A log of photoelectric effect was obtained from the same tool as the density log. This log was also severely affected by the invalid density "correction," and neither shipboard nor post-cruise reprocessing of this log has yielded any useful data.

Log Responses of Lithologic Units

Lithologic Unit I (0–221.5 mbsf) consists of nannofossil ooze and marly nannofossil ooze. Alternation of light and dark beds, associated with fluctuations in relative amounts of calcium car-

Table 10. Summary of interstitial water geochemical data, Site 722.

Hole, core, section, interval (cm)	Depth (mbsf)	Vol. (mL)	pH	Alk. (mmol/L)	Sal. (g/kg)	Mg (mmol/L)	Ca (mmol/L)	Cl (mmol/L)	SO ₄ (mmol/L)	PO ₄ (μmol/L)	NH ₄ (mmol/L)	SiO ₂ (μmol/L)	Mg/Ca
722A-1H-4, 145-150	5.95	68	7.48	5.00	33.0	49.90	8.22	549	23.0	7.2	0.51	678	6.07
722A-3H-4, 145-150	25.35	45	7.61	6.75	33.0	44.64	6.88	555	14.8	9.9	1.20	893	6.49
722A-6H-4, 145-150	54.15	50	7.73	8.05	32.5	37.04	6.10	554	8.1	8.8	1.82	1044	6.07
722A-9H-4, 145-150	82.75	56	7.79	9.11	32.3	34.36	6.18	556	3.5	7.8	1.92	1032	5.56
722A-12X-4, 145-150	111.85	39	7.61	7.94	32.2	30.81	7.15	555	1.0	7.4	2.14	1042	4.31
722A-15X-5, 145-150	142.35	42	7.56	6.91	32.0	28.99	7.48	559	0.7	4.5	2.31	1012	3.88
722A-19X-4, 145-150	179.55	41	7.49	6.25	32.0	29.17	8.71	556	0.7	3.2	2.13	916	3.35
722A-22X-4, 145-150	208.65	34	7.33	5.63	31.8	27.86	9.55	558	1.0	2.7	2.15	1014	2.92
722A-27X-2, 140-150	253.90	60	7.32	4.91	32.3	27.31	10.10	562	0.0	2.4	2.08	1190	2.7
722B-27X-4, 140-150	252.40	55	7.67	4.85	31.8	27.14	10.14	563	0.0	2.0	1.93	1190	2.68
722B-30X-1, 0-1	275.60	15	7.35	4.02	34.4	39.42	11.47	566	1.0	2.3	1.59	846	3.44
722B-31X-4, 140-150	291.20	67	7.38	4.16	32.0	27.26	11.21	565	0.0	1.5	1.92	1257	2.43
722B-34X-2, 140-150	317.20	95	7.48	3.68	32.5	29.21	11.98	563	1.0	1.5	1.56	1161	2.44
722B-37X-5, 140-150	350.80	56	7.19	3.02	32.4	27.15	12.88	566	1.0	0.7	1.51	1208	2.11
722B-40X-2, 140-150	375.40	33	7.44	2.11	32.6	27.70	13.41	568	2.4	0.7	1.19	646	2.07
722B-43X-2, 140-150	404.30	10	7.49	1.49	32.8	28.00	13.58	570	2.4	0.0	1.21	167	2.06
722B-46X-5, 140-150	437.90	42	7.53	1.83	33.0	29.20	15.48	569	3.5	0.9	0.63	320	1.89
722B-49X-1, 140-150	463.80	31	7.58	1.81	32.0	28.17	15.58	548	3.9	0.3	0.61	226	1.81
722B-52X-5, 140-150	495.60	27	7.66	1.62	32.8	29.08	17.15	558	4.6	0.3	0.43	322	1.70
722B-58X-4, 140-150	552.10	15	7.63	1.69	33.0	28.94	18.69	562	3.5	0.4	0.41	361	1.55

bonate and silty clay, is present on a scale of 0.05–1.0 m. Calcium carbonate ranges from 50% to 89% and clay content ranges from 10% to 30% (see “Lithostratigraphy” section, this chapter).

The fine-scale cyclicity is largely beyond the vertical resolution of the logs. However, it does cause a fine-scale variation in neutron porosity (Fig. 37), resistivity (Fig. 37), gamma ray (Fig. 36), potassium, thorium, and uranium (Fig. 39) that occasionally defines individual beds but more often looks like noise because of undersampling. Clay content, as indicated by K and Th logs (Fig. 39), shows little overall change in the portion of Unit I for which openhole logs are available (73–221.5 mbsf). The K and Th do suggest a subtle and gradual downhole decrease in clay from 63 to 130–160 mbsf, followed by a slight increase down to the base of Unit I. A similar pattern is more obvious in the neutron porosity (Fig. 37), but the apparent correlation of highest porosities with lowest clay in the interval 130–160 mbsf is the opposite of the expected effect of clay on porosity.

The largest log response in Unit I is a major uranium peak at 91–94 mbsf (Fig. 39). This peak dominates the gamma ray response for Unit I (Fig. 36). Two possible causes for this peak are: (1) precipitation of uranium at a redox front, probably associated with high organic matter, or (2) a phosphorite layer, probably associated with a hiatus. Log responses do not indicate clearly which explanation is more likely. Immediately below the uranium spike is a pronounced uranium minimum at 99–104 mbsf, possibly implying local uranium leaching. This minimum is a slightly clay-rich layer, based on Th and K. From 104 mbsf to the base of Unit I, uranium exhibits a substantial overall decrease, with high-frequency oscillations. This decrease is not echoed by K and Th decreases, and high-frequency variations in U are out of phase with K and Th variations. Thus the U is dominantly not in the clays but in a component that is richest in the low-clay layers. Nannofossils are very low in U, and the component carrying the U is not known.

Sonic velocities exhibit a single substantial change in the logged interval of Unit I: a sudden downhole velocity increase from 1.62 km/s to 1.75 km/s (slowness decrease from 188 to 174 μs/ft; Fig. 35) in the interval 150–159 mbsf. This change is not caused by a change in clay mineral content (Fig. 39) or porosity (Figs. 37 and 38).

Lithologic Unit II (221.5–343.4 mbsf) includes nannofossil chalks and marly nannofossil chalks similar to Unit I. Based on log responses, the top of Unit II is probably the 218 mbsf up-

ward increase in uranium and decrease in thorium (Fig. 39). Unlike Unit I, diatoms are often abundant in Unit II. Based on examination of smear slides, biogenic silica component gradually increases downhole from trace amounts in basal Unit I to a maximum of 20% in the interval 245–330 mbsf. Between 330 mbsf and 343.4 mbsf, the biogenic silica component decreases rapidly to zero (see “Lithostratigraphy” section, this chapter).

Diatoms have a very large impact on many log responses, because even a small diatom content greatly increases porosity (e.g., Hamilton, 1976; Shipboard Scientific Party, 1987). The same overall pattern of diatom variations seen in smear slides is detected in log responses, but the log responses suggest some refinements to the depth distribution of diatoms in Unit II. From 221.5 mbsf to 298 mbsf, variations in relative abundance of diatoms and nannofossils undergo at least four major cycles, with a periodicity that fluctuates but averages about 15 m. This cyclicity is most obvious on the velocity log (Fig. 35), which is very sensitive to porosity variations at high porosities. The cyclicity is also present but is less obvious on density, neutron porosity resistivity (Fig. 37), and potassium (Fig. 39) logs. The log response to the diatom-rich intervals is a decrease in velocity, density, and resistivity, and an increase in neutron porosity. Potassium here is positively correlated with diatom abundance indications from other logs, indicating that the diatom-rich zones are also more clay-rich than the adjacent, presumably carbonate-rich, zones. Smaller-scale cycles, with periods of 3–4 m, are superimposed on the four large cycles.

Between 298 and 320 mbsf, diatom abundance is probably at a maximum, because this interval encompasses the lowest velocities, densities, grain densities, and resistivities, and highest neutron porosities of Unit II. Grain densities (calculated from density and neutron porosity) fluctuate between 2.0 and 2.4, very close to the 2.2 g/cm³ grain density of opal. This depth interval is consistent with smear slides but is much narrower than the 245–330 mbsf interval of maximum diatoms from smear slides. Almost the entire interval 248–341 mbsf is rich in diatoms based on log responses (exceptions are lows at 253–260, 268–275, and 332–336 mbsf), but the richest and most constant interval is 298–320 mbsf. Core recovery was unusually low in this short interval.

Both smear slides and logs indicate that the base of the diatom-rich zone is rather sharp. Velocity, density, grain density, and resistivity increase and porosity decreases through the interval 320–343 mbsf. A single cycle to high porosity and clay con-

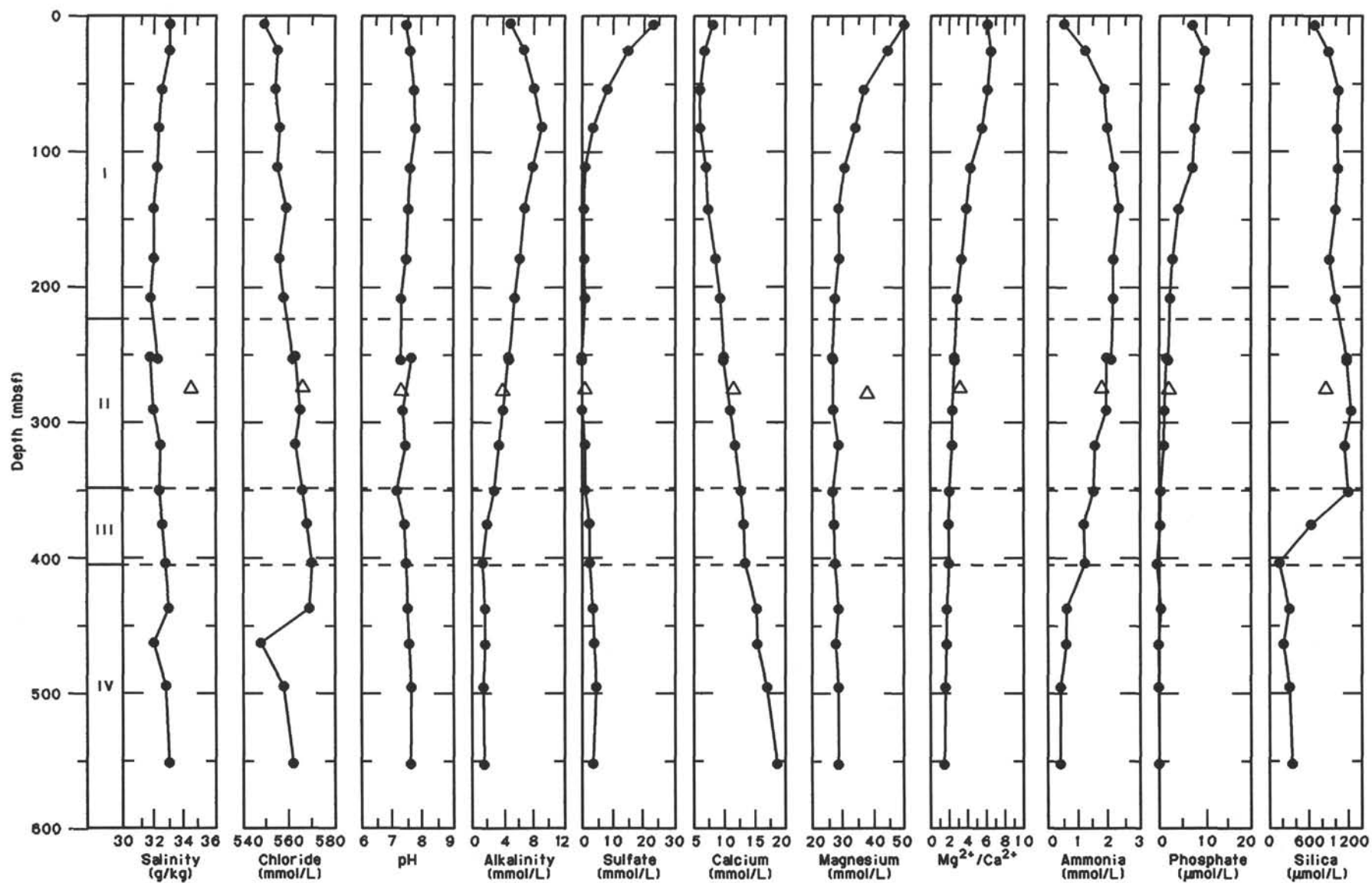


Figure 31. Concentration profiles vs. depth for Site 722. Dots = squeezed pore waters, triangles = *in-situ* pore-water samples. The dashed lines and numerals refer to the lithostratigraphic units.

Table 11. Results of Rock-Eval pyrolysis of samples from Holes 722A and 722B.

Core, section, interval (cm)	Depth (mbsf)	T _{max} (°C)	S ₁	S ₂	S ₃	S ₂ /S ₃	TOC	HI	OI
117-722A-									
1H-4, 144-145	5.94	421	0.21	0.78	4.54	0.17	0.35	222	1297
3H-4, 114-115	25.04	428	0.30	1.94	4.87	0.39	0.83	233	586
6H-4, 114-115	53.84	425	0.29	2.06	4.99	0.41	1.13	182	441
9H-4, 119-120	82.48	421	0.82	5.82	6.38	0.91	2.10	277	303
12X-4, 119-120	111.59	417	0.26	0.63	3.67	0.17	0.41	153	895
16X-2, 25-26	146.35	418	0.14	0.69	2.91	0.23	0.44	157	661
16X-2, 29-30	146.39	422	0.17	1.09	3.36	0.32	0.58	188	579
16X-2, 34-35	146.44	424	0.27	2.33	3.87	0.60	1.03	226	376
16X-2, 39-40	146.49	417	0.58	5.08	5.40	0.94	1.66	306	325
16X-2, 42-43	146.53	418	0.67	5.00	5.44	0.91	1.94	258	280
16X-2, 48-49	146.53	420	0.52	5.29	5.56	0.95	1.93	274	288
16X-2, 56-57	146.66	420	0.65	5.28	5.81	0.90	1.93	274	301
16X-2, 60-61	146.70	418	0.67	5.34	5.71	0.93	1.94	275	294
16X-2, 65-66	146.75	418	0.55	4.69	5.43	0.86	1.88	250	289
16X-2, 69-70	146.79	424	0.62	6.01	6.01	1.00	2.06	292	292
16X-2, 75-76	146.85	468	0.47	3.57	5.08	0.70	2.97	120	171
16X-2, 80-81	146.90	423	0.50	3.42	5.03	0.67	1.12	305	449
16X-2, 85-86	146.95	421	0.30	2.01	4.43	0.45	0.94	214	471
16X-2, 90-91	147.00	420	0.25	0.93	3.72	0.25	0.47	193	791
16X-2, 95-96	147.05	418	0.19	0.57	3.22	0.17	0.45	127	716
19X-4, 119-120	179.29	417	0.43	3.03	5.03	0.60	1.31	231	383
22X-4, 119-120	208.39	422	0.26	1.21	3.76	0.32	0.60	201	626
29X-3, 39-40	273.79	418	2.93	13.26	7.07	1.87	4.16	319	170
117-722B-									
29X-3, 120-121	270.10	442	0.27	2.03	1.86	1.09	0.72	282	258
29X-3, 125-126	270.15	412	0.70	5.25	2.57	2.04	1.79	293	144
29X-3, 130-131	270.20	417	1.20	7.49	2.93	2.55	2.23	336	131
29X-3, 135-136	270.25	409	1.05	7.44	2.93	2.53	2.22	335	132
29X-3, 140-141	270.30	413	0.98	8.00	3.00	2.66	2.17	369	138
29X-3, 145-146	270.35	418	1.16	8.37	2.95	2.83	2.26	370	131
29X-3, 149-150	270.39	412	1.00	7.84	2.97	2.63	2.23	362	133
29X-4, 5-6	270.45	416	0.77	6.35	2.62	2.42	1.84	345	142
29X-4, 10-11	270.50	413	0.62	4.34	2.50	1.73	1.51	287	166
29X-4, 15-16	270.55	411	0.47	3.07	2.47	1.24	1.30	235	190
29X-4, 20-21	270.60	416	0.31	2.82	2.31	1.22	1.10	256	210
29X-4, 25-26	270.65	410	0.35	1.78	2.12	0.83	0.97	184	219
29X-4, 30-31	270.70	410	0.23	1.31	2.06	0.63	0.83	158	248
29X-4, 35-36	270.75	403	0.28	0.98	2.29	0.42	0.80	123	286
29X-4, 40-41	270.80	403	0.39	0.84	2.06	0.40	0.49	171	420
29X-4, 47-48	270.87	408	0.20	0.44	1.48	0.29	0.74	58	200
29X-4, 52-53	270.92	403	0.10	0.29	1.38	0.21	0.28	103	493
29X-4, 60-61	271.00	421	0.17	0.54	1.52	0.35	0.27	200	562
31X-2, 114-115	290.94	422	0.46	2.94	4.84	0.60	0.91	323	531
51X-CC, 0-1	479.39	360	12.15	21.07	23.30	0.90	41.81	51	56
51X-CC, 2-3	479.40	354	13.86	29.77	17.12	1.73	53.78	55	31

Note: HI = hydrogen index and OI = oxygen index. For a detailed description of parameters, see "Explanatory Notes" chapter (this volume). The organic carbon data are measured by difference (total carbon minus inorganic carbon).

tent (and probably high diatoms) occurs within this interval at 337-339 mbsf, and much of the overall drop in diatoms probably occurs in the two short intervals 331-333 and 341-342 mbsf. Based on log responses, the base of Unit II is at 342 mbsf, very close to the 343.4 mbsf identification from lithostratigraphy.

Unit III (343.4-411.1 mbsf) consists of nanofossil chalk and marly nanofossil chalk, with only trace amounts of biogenic silica. Unit III is very similar to Unit I, except that porosities are much lower (see "Lithostratigraphy" and "Physical Properties" sections, this chapter).

Based on log responses, Unit III could be divided into two subunits. In the upper subunit (342-376 mbsf), both compaction and clay content gradually increase, based on increases in velocity, density, grain density, resistivity, potassium, and thorium, and decrease in neutron porosity. The lower subunit (376-405 mbsf) appears to be a relatively uniform chalk with low clay content, based on high velocity, density, and resistivity and low potassium, thorium, and porosity. The 50% neutron porosity of this interval is lower than any other pelagic interval at Site 722,

but about 5% higher than core measurements (see "Physical Properties" section, this chapter) because of the bound water in clays.

Unit IV (411.1-565.6 mbsf) consists of turbidites. In the interval 411-506 mbsf, the turbidites fine upward from silty claystone to nanofossil chalk or marly nanofossil chalk. Carbonate content gradually decreases downhole, to near zero below 495 mbsf. The interval 506-565.6 mbsf appears to consist of micaceous sands fining upward into silty clays and clays, though core recovery was only 22% below 497.9 mbsf (see "Lithostratigraphy" section, this chapter).

The transition from Unit III to Unit IV is obvious on all of the logs, but it is most pronounced on the K and Th logs because both the terrigenous and biogenous turbidites are much higher in clay minerals and mica than are the pelagic units above. A complex log response results from the complex and variable mineralogy of the turbidites, and it is not possible to determine lithology unambiguously without a formal log inversion. For example, in the interval 407-448 mbsf, velocity increases down-

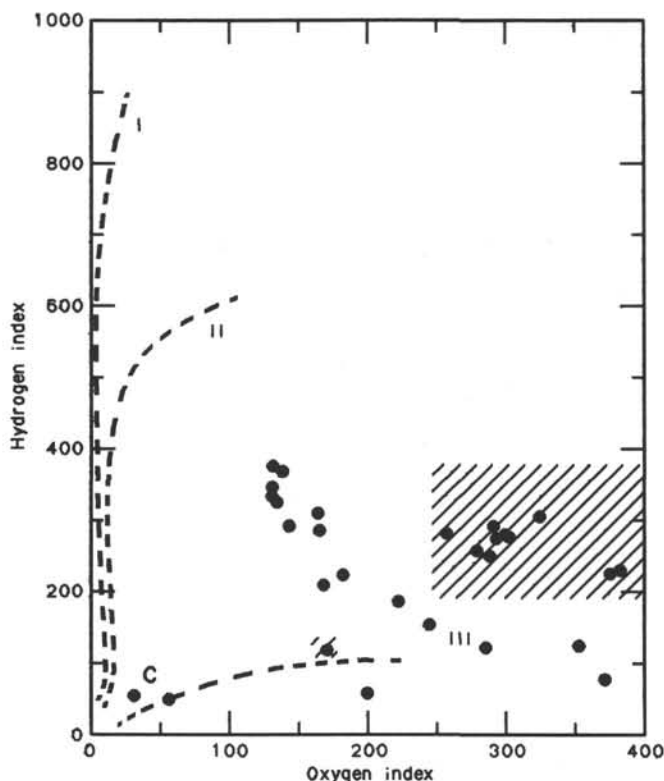


Figure 32. Plot of the hydrogen index vs. oxygen index of samples from Holes 722A and 722B. Samples plot mainly in the section for immature marine organic matter rich in relatively labile oxygen-rich functional groups. Samples from Core 117-722A-16X plot in the patterned area of the figure, while most samples from Core 117-722B-29X plot in the middle. C denotes two analyses of the coal sample.

hole, with a pronounced 10-m cyclicity that may represent variations in relative abundance of calcite and clay. However, the lowest-velocity intervals, which would normally be associated with clay, are lower in K and Th than the higher-velocity intervals. Further, mica in the sandier units can be higher in Th and K than the clays. This may explain the observation that most uranium variations are opposite in sign to K and Th variations, which requires that U be present in a different component than clay. These complexities can be unraveled by a quantitative log inversion for mineralogy; such a shore-based study is planned.

Borehole Deviation and Downhole Magnetometer

The GPIT accelerometer, which was included on the second logging run at Site 722, measures borehole deviation and magnetic moment. Because this run is padded against the borehole wall, neither measurement is adversely affected by the tool wobble which degrades the quality of GPIT logs run with free-swinging tools (e.g., "Downhole Measurements" section, "Site 723" chapter, this volume). The borehole deviation of Site 722 is a relatively constant 2.5° to the northeast (Fig. 40).

The GPIT uses three perpendicular fluxgate magnetometers to measure magnetic moment. The tool was designed for obtaining the azimuthal orientation of dipmeter logs, so no attempt was made to magnetically insulate the tool from the magnetic influence of the tool string itself. Tool-string magnetization is substantial: the measured inclination in the "nonmagnetic" chalks at Site 722 is 18.5° – 19.0° (Fig. 40), in contrast to the inclination of about 30° for the earth's magnetic field at this latitude. Tool magnetization can be removed, as was done when this tool was used to log the magnetization of the oceanic crust at Hole 504B (Shipboard Scientific Party, 1988). However, this correction has

not been applied yet at Site 722, because the tilt of the tool is relatively constant and has little effect on the character of the log record. To our knowledge, Site 722 is the first oceanic sediment section to be logged with a downhole magnetometer. Two logging runs were obtained, by recording during both logging down and logging up.

The total moment log exhibits long wavelength variations which are not reproduced in the two logging runs (Fig. 40). These gradual changes are probably caused by the high daily variation (S_q) at low latitudes. An approximate removal of daily variation effects is possible, based on average daily variation at this latitude or observatory records. However, a more reliable correction would require suspending a magnetometer beneath the ship, as was subsequently done at Sites 723 and 728 (see "Downhole Measurements" sections, "Site 723" and "Site 728" chapters, this volume). This daily variation has primarily a subtle long-term effect on the inclination logs (Fig. 40), perhaps causing the offset of upgoing and downgoing logs. However, some finer-scale effects are also present, such as the inclination low in the upcoming log at 263 mbsf and the inclination shift in the downgoing log at 451 mbsf. Thus only the inclination features which replicate well on two logging passes should be attributed to changes in formation magnetization, and even replication is not a fail-safe indicator of formation changes (e.g., the shifts in both inclination and moment for both downgoing and upcoming logs at 187 mbsf).

The inclination records in the chalks of Units I to III are relatively flat, with little coherent variation on the two logging runs. A baseline shift in inclination at 270–280 mbsf may indicate a real change in magnetic properties of the formation, but, in general, the magnetic log exhibits the lack of formation response that would be expected from the very low susceptibility and intensity of magnetization of these sediments (see "Paleomagnetism" section, this chapter). Even the increased susceptibility of Unit III, in comparison to Unit II (see "Paleomagnetism" section, this chapter), is subtle or absent in the inclination records.

In contrast to the chalks, the turbidites of Unit IV do have a detectable formation magnetization. Magnetic inclination increases from 391 mbsf, just above the top of Unit IV (411.1 mbsf), to 466 mbsf. Several of the fine-scale fluctuations in this interval of increase are present on both logs. Below 466 mbsf the two logs overlay very closely (Fig. 40).

The source of the changes in formation magnetization detected by the downhole magnetometer is probably susceptibility. Viscous magnetization and remanent magnetization also contribute to the magnetization, but their magnitudes are probably much lower.

INTERHOLE CORRELATION

At Site 722, the two holes are located west and slightly down-dip of the crest of the Owen Ridge and are aligned in a north-northeast direction. Hole 722B is 20 m northwest of Hole 722A. Hole 722A was drilled to 86.5 mbsf with the APC and to 280.0 m with the XCB, while Hole 722B was drilled to 91.9 m with the APC and to 565.1 m with the XCB. The recovery of the APC was almost perfect in both holes. The top of Hole 722B obtained the mud line, which was not recognized in Core 117-722A-1H. The age range of the sedimentary sequence is Pleistocene to the early Miocene.

Here we provide detailed correlations within lithologic Unit I at Site 722. Lithologic Unit I has an age range from Pleistocene to the late Miocene, 0–7.5 Ma, and is characterized by cyclic changes in the nature of sediments that can be identified by visual observation and by variations of magnetic susceptibility and CaCO_3 content. Correlation of the sedimentary cycles of layers among these holes provides valuable information on the relative rate of sedimentation, which is necessary information for any

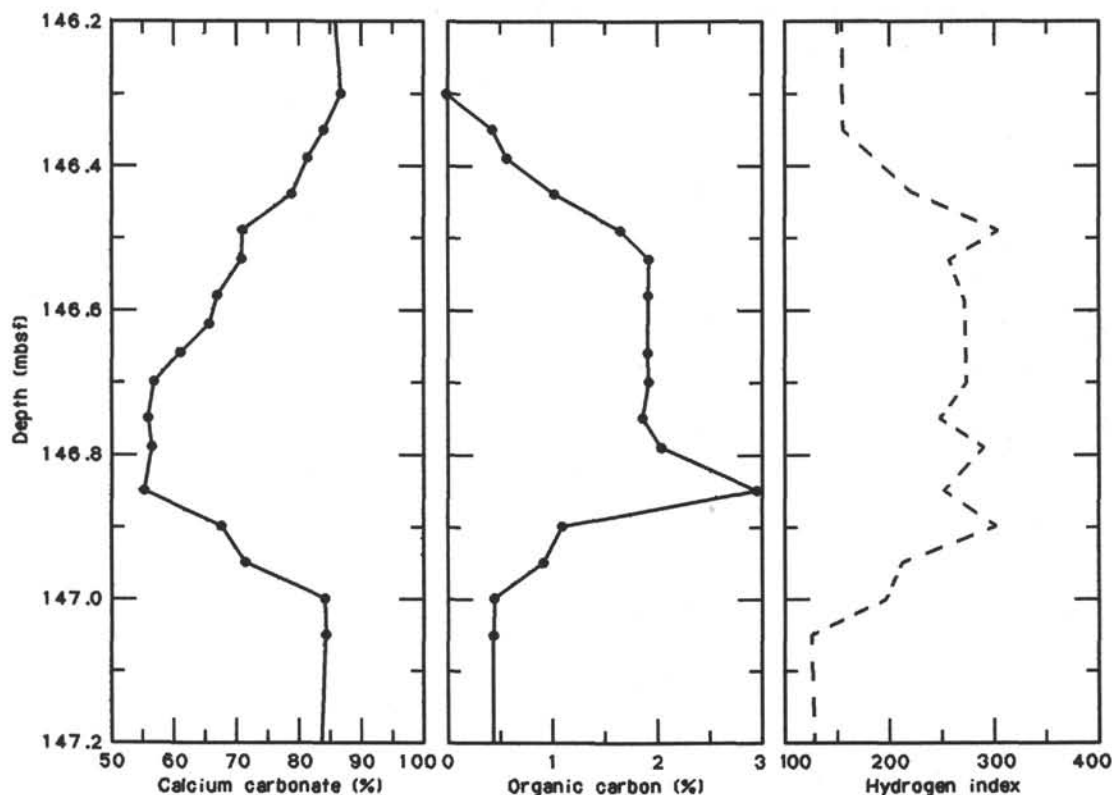


Figure 33. Downhole plot of the calcium carbonate and organic-carbon content and the hydrogen index in Section 117-722A-16X-2.

high-resolution study of depositional environments. The essence of the correlation procedure is discussed in the "Explanatory Notes" chapter (this volume).

Hole-to-hole correlations were made on the basis of visual identification of distinctive layers, as well as on physical and magnetic properties. The GRAPE density and magnetic susceptibility were measured continuously and at 5-cm intervals, respectively, on whole core sections. Lithologic descriptions and photographs were made on the split cores.

The visual correlation of the cores relied primarily on the core photographs. Several distinct and traceable layers have been determined in the upper 140 m interval of the correlatable sedimentary sequence at Site 721 and have been notated as a_0 , a_1 , ..., n_2 , and n_3 , based on the correlation between Holes 721A, 721B, and 721C. The letter code (i.e., a, b, c, ...) refers to the sequence of cores, and the number code indicates the number of marker layers in each core. For example, the notation " a_3 " corresponds to the third marker layer defined in Core 117-721A-1H, and " b_1 " denotes the second marker layer in Core 117-721A-2H. The marker layers a_0 to i_4 were defined on the cored sediments of Hole 721A above 91.7 mbsf and i_5 to n_3 on Hole 721B below 94.25 mbsf. The criterion to define a marker layer is that the layer is distinct enough to trace it in the sedimentary sequence of the other holes and that the character does not change. The useful criteria for recognizing the marker are color boundaries, distinctly colored layers, shape of bioturbations, and sequence of color change in surrounding sediments. The marker layers were based mainly on the sedimentary sequence initially described at Hole 721B. Two new marker layers, k_2 and t_3 , were defined in Hole 722A. Table 13 lists the depth of the marker layers in the two holes of Site 722.

Figure 41 shows the magnetic susceptibility curve and positions of individual, visually correlatable layers. The pattern of

the susceptibility and the positions of layers match very well, not only among the two holes, but also between Sites 721 and 722. The stratigraphy of the magnetic susceptibility data and the visually identified layers are extremely consistent in that a particular visually characteristic layer always coincides in depth with a distinct feature in the magnetic susceptibility curve. In this way the lithologic correlations have been verified using the magnetic susceptibility data, which are quantitative. The reliability of any given correlation is bounded by the interval of susceptibility measurement, which is ± 5 cm.

The results of the layer-by-layer correlation allow us to calculate true thickness between the layers that coincide with and are separated by core boundaries. Occasionally core tops were expanded by water uptake during drilling. In this case, the apparent thickness of the disturbed sediment layer is observed to be thicker than the original thickness. In some instances, the top part of the core was missing; in this case apparent thickness is observed to be thinner than the original thickness. Fortunately, the two holes were staggered in depth, so that they have different horizons at core boundaries (Table 13). The original thickness of layers coinciding with core tops or bottoms can be obtained by comparing thickness of the correlative layer in the continuous section of the other holes. The calculation of the amount of the difference can be achieved by the differences in the depths of marker layers between the holes (last column in Table 13). The differences of marker layers a_0 and a_1 are -1.85 and -1.65 m. The differences were caused by the missing of the mudline in Hole 722A. The differences a_2 , a_3 and a_4 are -1.40 , -1.55 , and -1.35 m, respectively, which are significantly different from that of a_0 and a_1 . Marker layers a_0 to a_4 are identified within Core 117-722A-1H; however, they are separated into Cores 117-722B-2H and -3H. Because the core boundary of Cores 722B-1H to -2H is located between a_1 and a_2 , the changes

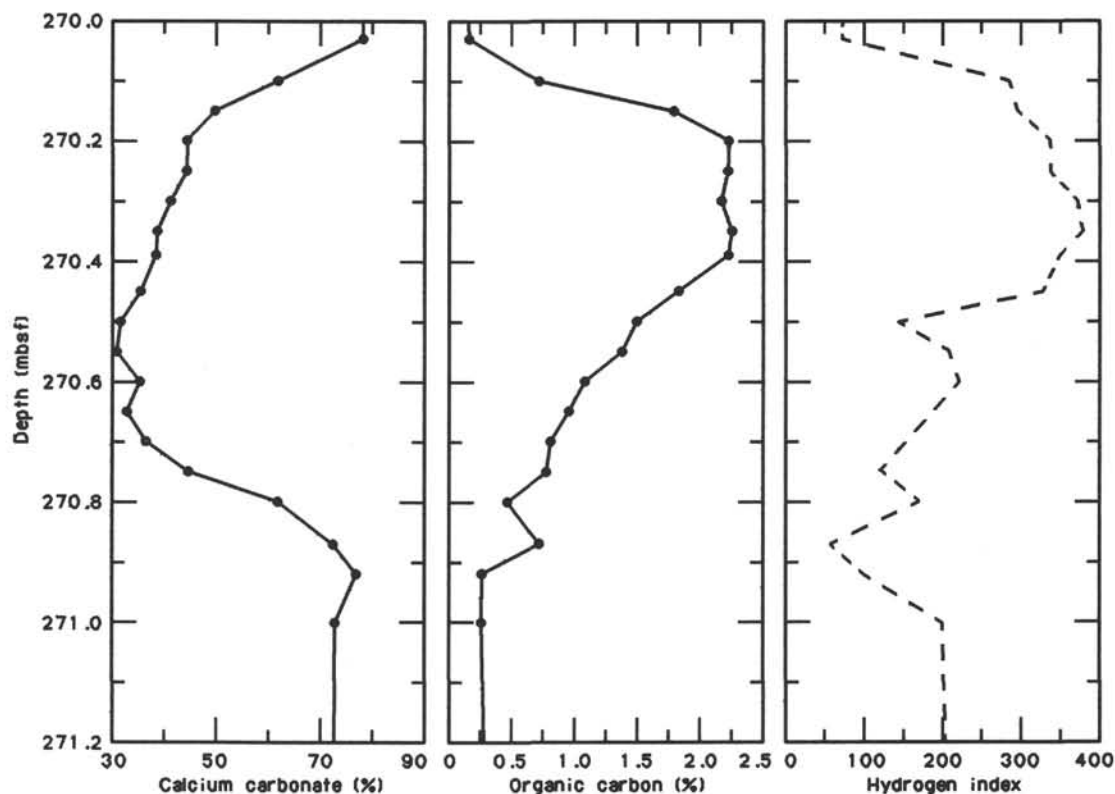


Figure 34. Downhole plot of the calcium carbonate and organic-carbon content and the hydrogen index in Sections 117-722B-29X-3 and -4.

Table 12. Concentrations of methane (C_1) and ethane (C_2) per liter of wet sediment in cores of Holes 722A and 722B.

Core, section, interval (cm)	Depth (mbsf)	C_1 ($\mu\text{L/L}$)	C_2 ($\mu\text{L/L}$)
117-722A-			
1H-4, 144-145	5.94	732	
3H-4, 119-120	25.09	76	
6H-4, 119-120	53.89	110	
9H-4, 119-120	82.49	95	2
12X-4, 119-120	111.59	246	3
27X-2, 114-115	253.64	94	
117-722B-			
27X-4, 114-115	252.14	107	
31X-4, 114-115	290.94	128	2
43X-2, 114-115	404.04	23	
46X-5, 114-115	437.64	17	
49X-3, 114-115	463.54	12	
58X-4, 114-115	551.84	13	

Note: Values are expressed in $\mu\text{L/L}$ (volume gas/volume wet sediment).

in the depth differences can be explained by the lack of about 20 cm missing in Core 117-722B-3H. Table 14 gives the differences between the depth (mbsf) calculated by the ODP CORELOG computer program data and the corrected depth (mbsf) calculated by the layer-by-layer correlation method.

The layer-by-layer method on the double- or triple-cored sedimentary sequences gives us true stratigraphic thickness after the correction for core-boundary disturbance. Table 15 shows the stratigraphic thickness at Site 721, where most of the marker layers were defined, and Holes 722A and 722B. The corrected

depths in Hole 722A and 722B agree well with each other. The intersite correlation of the marker layers shows clearly the existence of a hiatus at Site 722 in the interval from I_4 to n_1 .

SUMMARY AND CONCLUSIONS

The primary reason for coring at Site 722 was to recover a continuous high-resolution section of pelagic sediments of late Neogene age from another area of the crest of the Owen Ridge to complement the records obtained at Site 721. The seismic stratigraphy at Site 722 revealed that it had a more complete section than did Site 721. The sediments on the ridge have been deposited well above the carbonate lysocline and beyond the zone of lateral bottom transport from the continental margin for much of the Neogene. Study of the sedimentary sequences obtained at Sites 721, 722, and 730 will provide information on the initiation, variability, and history of monsoonal upwelling in the Arabian Sea. The detailed biotic, chemical, and sedimentologic records obtained at this site also will provide data on monsoonal upwelling that, combined with data from the Oman margin Sites 723 to 730, will be used to test the hypothesis that much of the short-term variability (10^3 yr) of monsoonal upwelling is forced by changes in solar radiation related to variations in the shape of the earth's orbit (the Milankovitch mechanism). Long-term trends of the intensity of the monsoon related to the uplift of the Himalaya may also be imprinted on the long paleoenvironmental record from the ridge. The combined record of Sites 722 and 721 insures that a complete record of the upper Neogene sediments have been recovered from the Owen Ridge. In addition, the age and character of the sediments at Site 722 will be used to investigate the depositional and tectonic uplift history of the Owen Ridge.

The preliminary shipboard findings at Site 722 parallel the findings at Site 721. Here, we summarize the new information

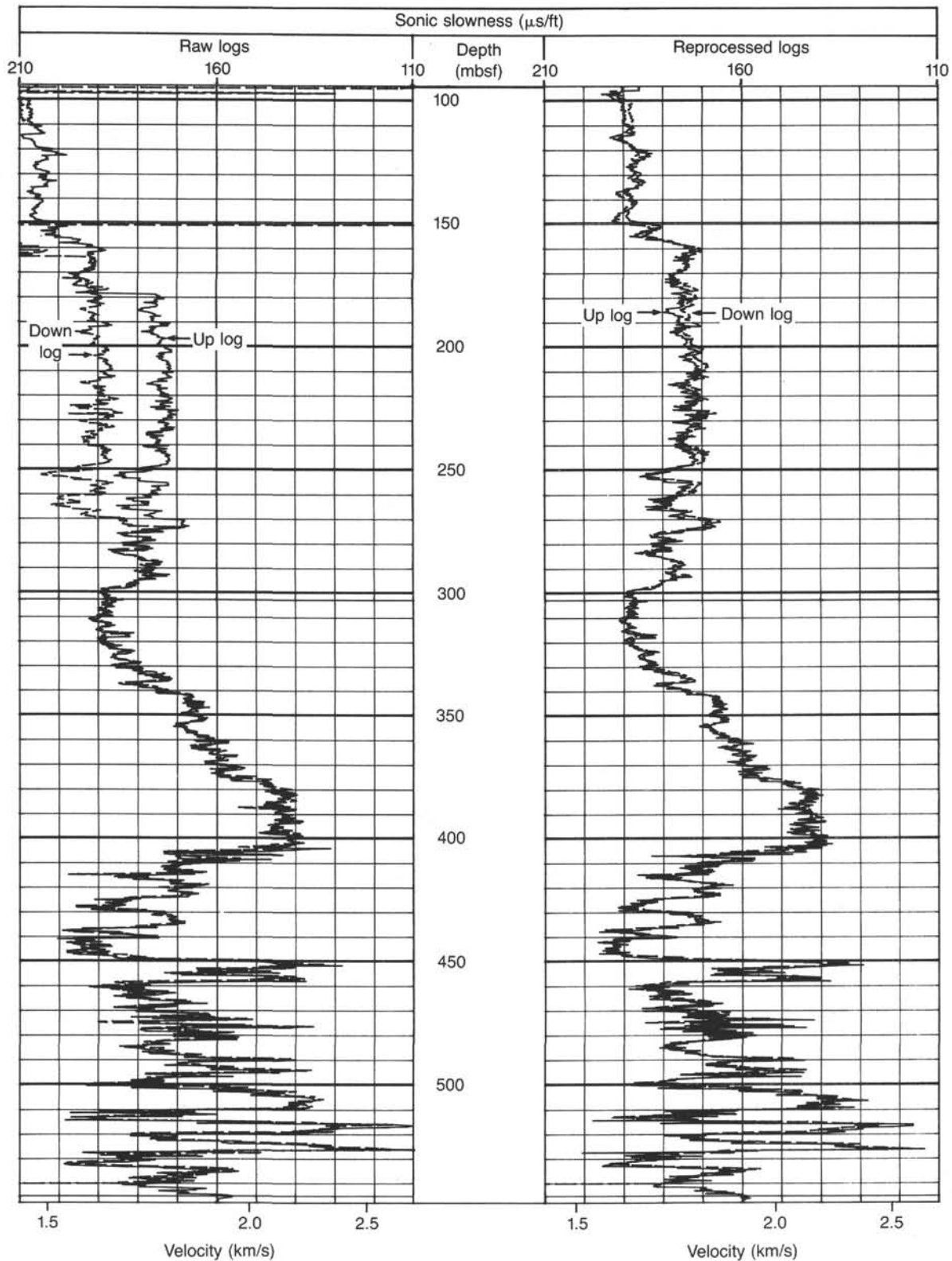


Figure 35. Comparison of the raw (left) and reprocessed (right) sonic logs from Site 722. Sonic slowness, the inverse of velocity, is in microseconds per foot. Both downgoing (dashed) and upcoming (solid) logs are shown.

pertinent to the above objectives (Fig. 42). These findings include the identification of:

1. A complete stratigraphic section from early Miocene to the Holocene.

2. The appearance of siliceous facies in the middle Miocene.
3. The sequential appearance of cold "upwelling" faunas in the upper Miocene and Pliocene.

4. Well-defined sedimentary cycles that are defined by changes in sediment color, magnetic susceptibility, and physical

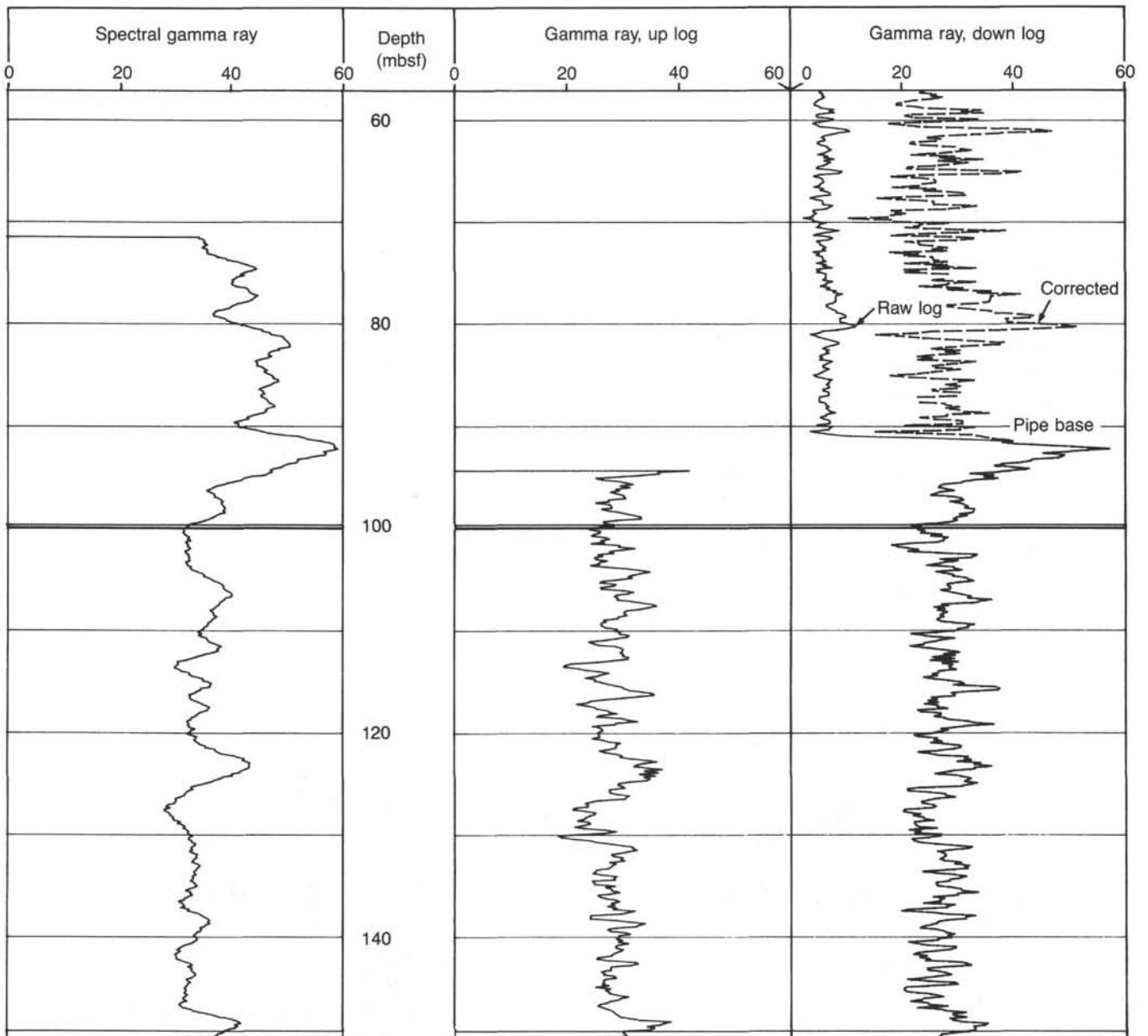


Figure 36. Comparison of three gamma ray logs for part of the upper portion of Site 722. The spectral gamma-ray log (left) was obtained from a different logging tool than the upcoming (center) and downgoing (right) gamma ray logs. Horizontal heavy lines indicate the varying depth of pipe for the different runs. The attenuation of gamma ray signal in through-pipe logs is evident on the downgoing log. An attempt to correct this portion of log (dashed line) by applying a gain factor yields results inconsistent with the spectral gamma ray log (left).

properties and that can be correlated between holes and between Sites 722 and 721. The cycles have distinct periodicities, which are consistent with the Milankovitch frequencies.

5. A threefold increase in carbonate and noncarbonate accumulation rates in the middle and lower upper Miocene. The high rates are followed by low rates in the lower Pliocene, and increasing rates during the Pliocene-Pleistocene.

6. The cessation of turbidite deposition on the ridge crest in the lower Miocene.

7. The occurrence of vein structures in the siliceous Unit II, which appears to be coincident with the slumped section in Site 721.

8. Generally high values of marine-derived organic carbon within phases of high sediment accumulation.

9. The presence of chlorite and absence of kaolinite in the noncarbonate mineral fraction, which was similar to the mineralogy of the Indus Fan Site 720.

The major themes that are relevant to the interpretation of the depositional history of Site 722 are the same as at Site 721 and emphasize the uplift of the Owen Ridge, the onset and preservation of siliceous fossils and the appearance of distinct upwelling faunas, and the pattern of high-frequency variability in the abundance of various sedimentary components. Below, we briefly address these themes.

Uplift of the Owen Ridge

The uplift history of Owen Ridge at Site 722 is indicated by the gradational transition from a turbiditic to a pelagic facies in the latest early Miocene, as was the case at Site 721. On the basis of mineralogy, we infer that the provenance of the turbiditic sediments on the Owen Ridge was probably the same source as for the Indus Fan. This inference is based on the presence of well-crystallized chlorite and the absence of kaolinite; an associ-

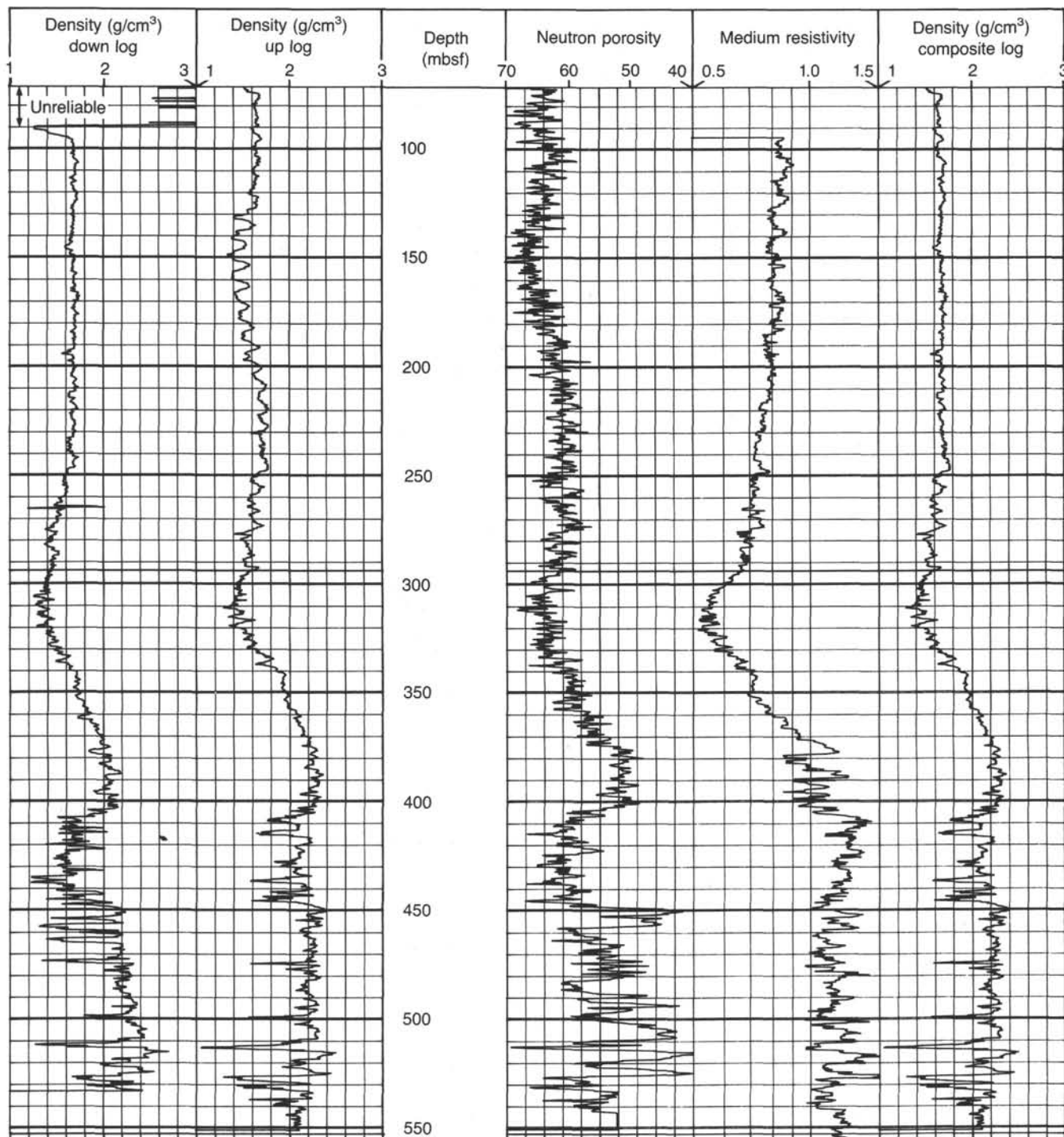


Figure 37. Logs of density, neutron porosity, and resistivity for Site 722. The density log at far right is a composite of the more reliable portions of the two density logs at far left.

ation that is identical to the mineralogy of the Indus Fan deposits recovered at Site 720. The upper boundary of the turbiditic sequence at Site 722 is marked by a prominent seismic reflector (C) that onlaps onto a basement peak near the site.

The lower Miocene turbidites at Site 722 are overlain by pelagic nanofossil chinks of lithologic Unit III that are middle Miocene in age (Fig. 42). The chinks are characterized by high carbonate content (76%) and poor opal preservation. The chalk

unit is about 68 m thick and is succeeded by 122 m of siliceous nanofossil chinks of lithologic Unit II that are middle and late Miocene age. This sequence exhibits distinct trends in its physical properties as it grades from low porosity and high densities and velocity at the base of the chalk unit to high porosity and low density and velocity in the middle of the siliceous unit (Fig. 42). These gradients in physical properties give the chalk and siliceous units a distinctive seismic reflection signature that can be

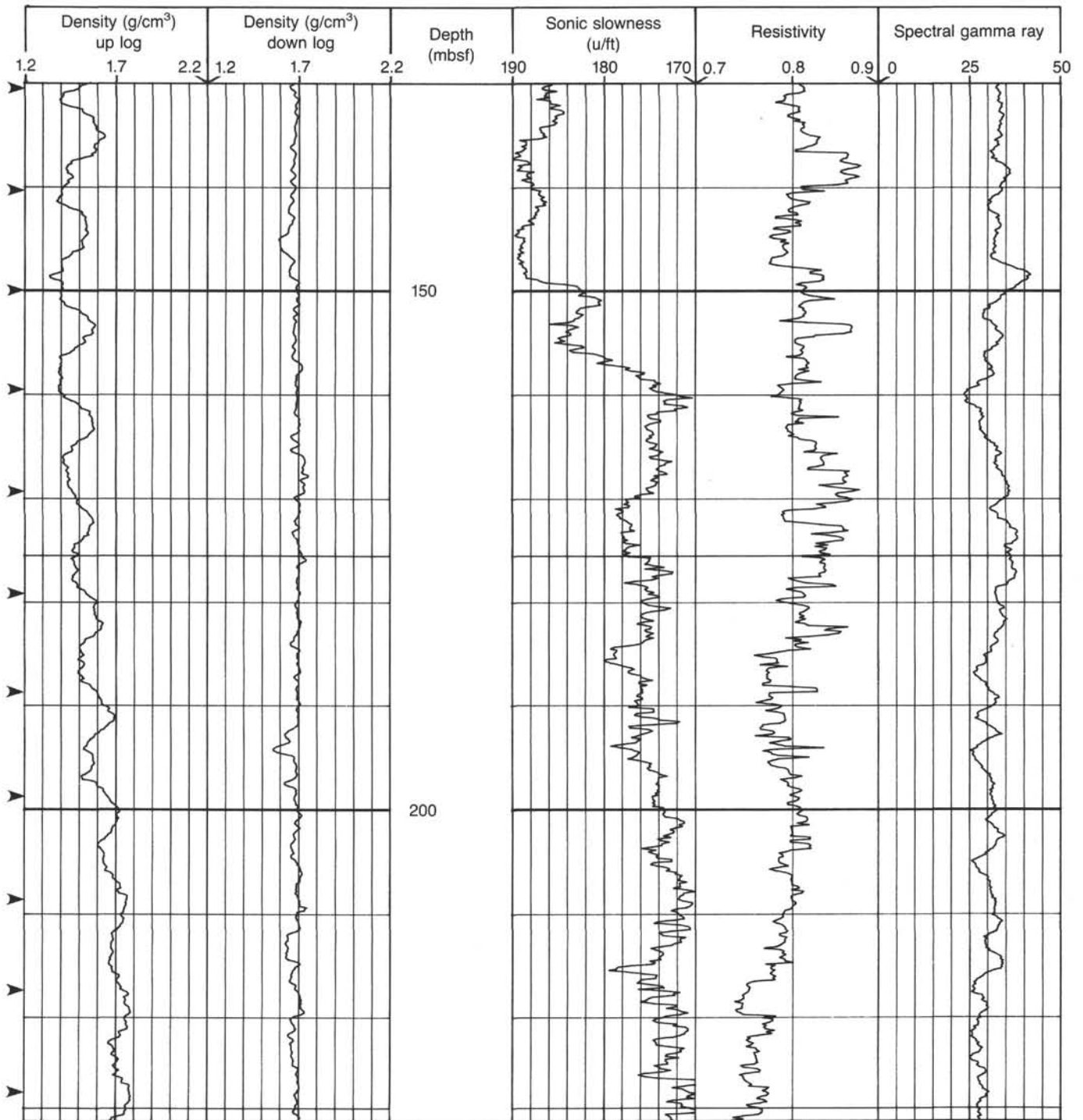


Figure 38. Expanded plot of the strong cyclicity in upcoming density log data for 130–230 mbsf (see also Fig. 37), showing that the cycles are present in sonic, resistivity, gamma-ray, or upcoming density logs. The cycles do correlate strongly with drill-pipe position at the times cores were taken; they are an artifact associated with the effects of circulating during coring on borehole diameter.

mapped over much of the Owen Ridge. The stratigraphic and seismic data indicate that much of this middle Miocene section is missing at Site 721. Comparison of the sections at Sites 721 and 722 indicate that about 30 m of the chalk unit and 90 m of the siliceous unit are missing at Site 721.

The interval of the siliceous sediments in lithologic Unit II with the highest porosity and lowest density also displays distinctive sigmoidal vein structures. The vein structures are perpendicular to bedding and occur preferentially in the darker

bands. Similar structures have been observed in accretionary prisms (Suess, von Huene, et al., 1988) and have been ascribed to both hydrofracturing by dewatering mechanisms, and dilation as a result of applied deviatoric stresses. The significance of these structures at Site 722 is not clear, but we note their association with the low-density sediments that failed by slumping at Site 721. Possibly the slump event caused a decrease of lateral stress at Site 722, which is about 10 km away. However, the vein structures have only about 300 m of overburden at present and

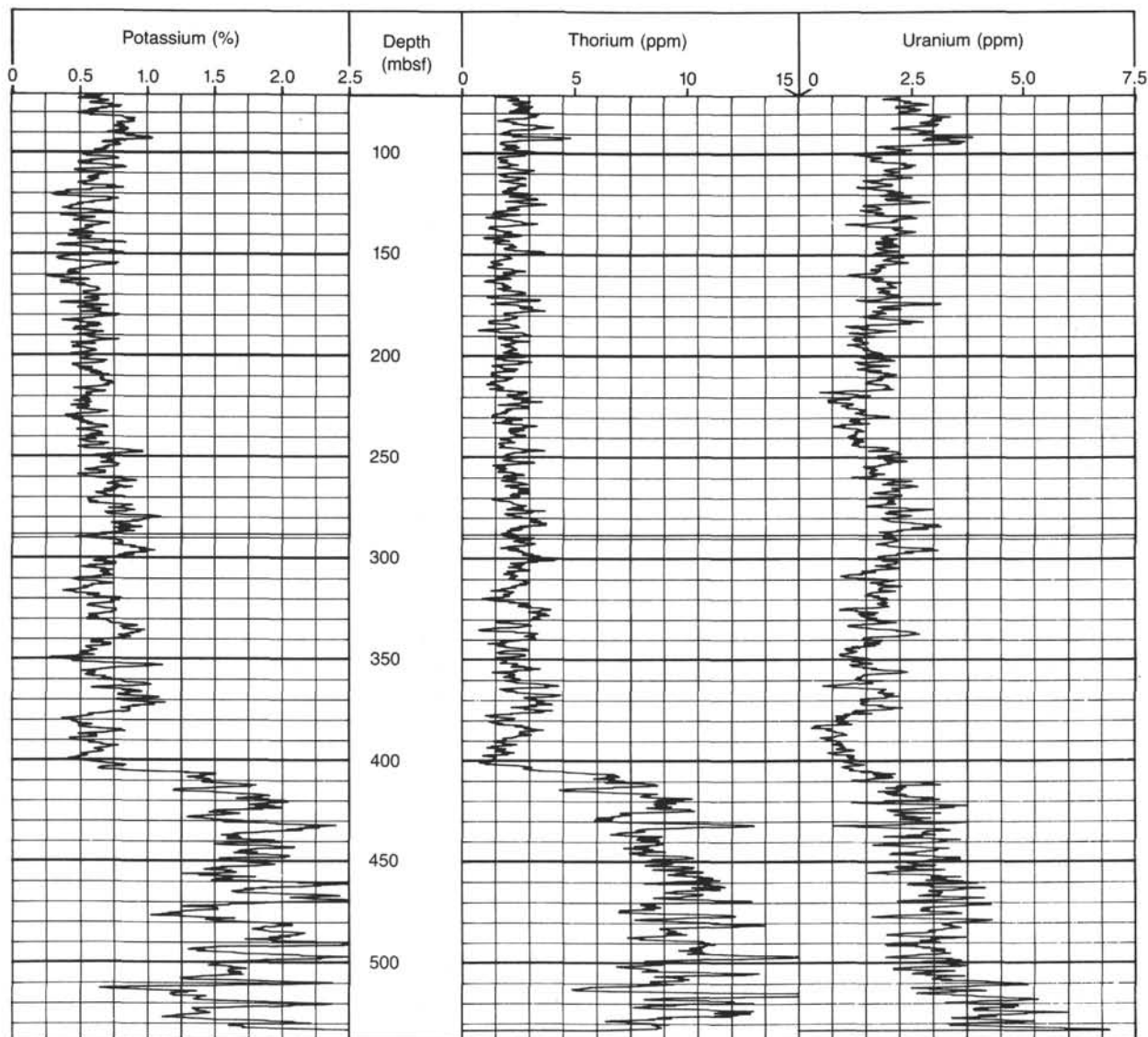


Figure 39. Reprocessed logs of potassium, thorium, and uranium at Site 722.

may have had less at the time of vein formation, which is unknown at this time. The structural features may reflect the tectonic processes that caused the uplift of the Owen Ridge, but the specific relationship cannot yet be identified.

The Onset of Upwelling Faunas and Opal Deposition

The western Arabian Sea is presently characterized by large seasonal or monsoonal variations in atmospheric and oceanic circulation. During the southwest summer monsoon (June-July-August), the winds blow strongly from the southwest and cause intense upwelling along the continental margin of Oman. This upwelling causes significant changes in the properties of the oceanic mixed-layer. For example, in the western Arabian Sea, sea-surface temperatures decrease, and nutrient content and productivity increase. In the modern and late Pleistocene ocean, these changes are recorded by the response of planktonic organisms to changing environments (i.e., carbonate and opal productivity and species composition), by the composition and input of eolian dust, and by the relative proportions of pollen species. On the basis of such paleoceanographic reconstructions, several hypotheses have been put forward concerning the mech-

anisms that control the strength of the monsoon and how it is related to changes in global climate. Two of the potential causes for changes in monsoonal intensity are changes in the topography of Tibet-Himalaya complex and variations in the seasonal distribution of solar radiation due to changes in the earth's orbit; i.e., the Milankovitch mechanism. Both higher elevations of the Tibet-Himalaya complex and increased summer solar radiation produce stronger monsoonal circulation.

If late Neogene uplift and orbital changes affect the intensity of the monsoon, the sediments at Site 722 should record both changes in productivity and variations in distinct biotic assemblages due to the variations of upwelling. The sediments should also reflect increased eolian transport, although much of the transport may occur during the winter season. Furthermore, variations in source area of the eolian components may result in differing mineralogy and chemistry. Thus, the cyclic variations in sediment composition related to changes in solar radiation should have specific frequencies, the "Milankovitch spectrum," that may be quantitatively identified in the sediments of Site 722.

At Site 722, we recognized a dramatic change in the sediment facies in the upper middle Miocene. Prior to this time, biogenic

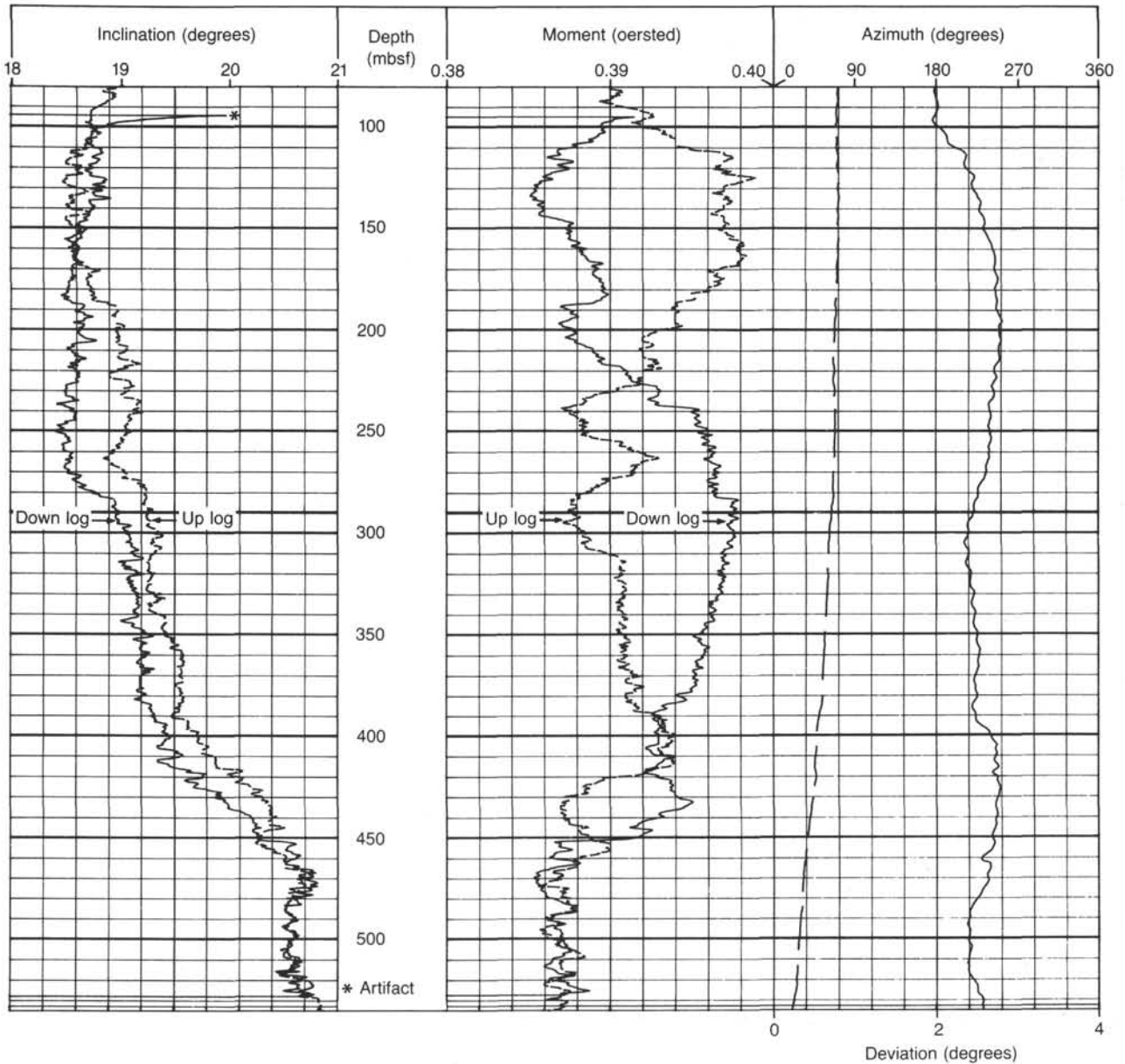


Figure 40. Logs of magnetic inclination (degrees), magnetic field strength (oersteds), borehole deviation (degrees), and deviation azimuth (degrees) at Site 722.

opal was absent from the sediments and carbonate was poorly preserved. The opal appears suddenly (between two cores) in the top of chalk Unit III in the upper middle Miocene (Fig. 42). Both radiolarians and diatoms are abundant and the species are tropical in nature. However, the associated planktonic foraminifer fauna contains species (rare, but well-preserved) that are indicative of upwelling. Preliminary analyses indicates that this early phase of opal accumulation on the ridge is not associated with particularly high accumulation rates. The upper middle and lower upper Miocene interval has carbonate and noncarbonate (including opal) accumulation rates of 1–3 g/cm²/k.y. (Fig. 42). The remainder of the upper Miocene is characterized by high rates of carbonate (over 3 g/cm²/k.y.) and moderate noncarbonate (about 1 g/cm²/k.y.) accumulation. The radiolarian assemblage is a mix of tropical and upwelling species, while the nannofossil floras have low diversity (Fig. 42). Although not all of these biotic and sedimentologic indicators of high produc-

tivity are in accord, the latter half of the late Miocene was clearly an interval of higher pelagic influx to the sediments at Site 722. This pattern does not seem to be caused merely by better preservation, because changes in the preservation of foraminifers and nannofossils do not coincide with changes in rates.

The carbonate accumulation rate decreases to about 1.5 g/cm²/k.y. in the lower Pliocene and the decrease appears independent of any change in carbonate preservation. From the upper Pliocene to the Present, both carbonate and noncarbonate accumulation rates show a continuous long-term increase (Fig. 42). The exact relationships between the biotic assemblages, accumulation rates, monsoonal upwelling, and global climate change will have to be clarified during post-cruise research.

Short-term Variability and Sedimentary Cycles

The cyclic character of the Pliocene and Pleistocene sediments at Site 722 is identical to that of Site 721. The alternation

of foraminifer-bearing, foraminifer-nannofossil, and nannofossil ooze (Unit I) is paralleled by changes in sediment color, magnetic susceptibility, bulk density, and carbonate content. The strong cyclicity of these sediments is shown by detailed measurements of magnetic susceptibility that reveal a distinct and dominant periodicities. Using paleomagnetic boundaries for age control, power spectra of the magnetic susceptibility time series give periodicities near 19 k.y., 23 k.y., 41 k.y., and 400 k.y. Some intervals show power near 100 k.y. These periodicities match those expected for the Milankovitch mechanism, which is suspected to be a major cause of variations in monsoon intensity. The sediment cycles observed in Site 722 are thought to reflect changes in pelagic productivity, in the preservation of opal and carbonate, and in the input of eolian material. Again, we emphasize that these periodicities are not unique to the monsoon mechanism and that much post-cruise research is needed to identify the true monsoon signature and its spectrum.

REFERENCES

- Barron, J. A., Keller, G., and Dunn, D. A., 1985. A multiple microfossil biochronology for the Miocene. *Geol. Soc. Am. Mem.*, 163:21-36.
- Berggren, W. A., Kent, D. V., and Van Couvering, J. A., 1985. The Neogene: Part 2, Neogene geochronology and chronostratigraphy. In Snelling, N. J. (Ed.), *The Chronology of the Geological Record: Geol. Soc. Mem.* (London), 10:211-260.
- Carlson, R. L., Schaftenaar, C. H., and Moore, R. P., 1979. Causes of compressional-wave anisotropy in calcareous sediments from the Rio Grand Rise. In Barker, P. F., Carlson, R. L., Johnson, D. A., et al., *Init. Repts. DSDP*, 72: Washington (U.S. Govt. Printing Office), 565-576.
- Hamilton, E. L., 1976. Variations of density and porosity with depth in deep-sea sediments. *J. Sediment. Petrol.*, 46:280-300.
- , 1978. Sound velocity-density relations in sea-floor sediments and rocks. *J. Acoust. Soc. Am.*, 63:366-377.
- , 1979. Sound velocity gradients in marine sediments. *J. Acoust. Soc. Am.*, 65:909-922.
- Johnson, D. A., and Nigrini, C. A., 1985. Synchronous and time-transgressive Neogene radiolarian datum levels in the equatorial Indian and Pacific Oceans. *Mar. Micropaleontol.*, 9:489-523.
- Johnson, D. A., Nigrini, C. A., Caulet, J.-P., Schneider, D., and Kent, D., in press. Pliocene-Pleistocene radiolarian events and magnetostratigraphic calibrations for the tropical Indian Ocean. *Mar. Micropaleontol.*
- Kennett, J. P., 1982. *Marine Geology*: Englewood Cliffs, N.J. (Prentice-Hall).
- Kolla, V., Kostecki, J. A., Robinson, F., and Biscaye, P. E., 1981. Distribution and origins of clay minerals and quartz in surface sediments of the Arabian Sea. *J. Sediment. Petrol.*, 51:563-569.
- Pisias, N. J., and Moore, T. C., 1981. The evolution of Pleistocene climate: a time-series approach. *Earth Planet. Sci. Lett.*, 52:450-458.
- Prell, W. L., and Van Campo, E., 1986. Coherent response of Arabian Sea upwelling and pollen transport to late Quaternary monsoonal winds. *Nature*, 323:526-528.
- Sato, T., Takayama, T., Kato, M., Kudo, T., and Kameo, K., in press. Calcareous microfossil biostratigraphy of the uppermost Cenozoic formations distributed in the coast of the Japan Sea. Part 4: Conclusion. *Sekiyu Gijutsu Kyokaiishi*.
- Shipboard Scientific Party, 1987. Site 645. In Srivastava, S., Arthur, M. A., et al., *Proc. ODP, Init. Repts.*, 105: College Station, TX (Ocean Drilling Program), 61-418.
- , 1988. Site 504. In Becker, K., Sakai, H., et al., *Proc. ODP, Init. Repts.*, 111: College Station, TX (Ocean Drilling Program), 35-251.
- Suess, E., von Huene, R., et al., 1988. *Proc. ODP, Init. Repts.*, 112: College Station, TX (Ocean Drilling Program).
- Takayama, T., and Sato, T., 1987. Coccolith biostratigraphy of the North Atlantic Ocean, Deep Sea Drilling Project Leg 94. In Ruddiman, W. F., Kidd, R. B., Thomas, E., et al., *Init. Repts. DSDP*, 94, Pt. 2: Washington (U.S. Govt. Printing Office), 651-702.
- Theyer, F., Mayer, L. A., Barron, J. A., and Thomas, E., 1985. The equatorial Pacific high-productivity belt: elements for a synthesis of Deep Sea Drilling Project Leg 85 results. In Mayer, L., Theyer, F., et al., *Init. Repts. DSDP*, 85: Washington (U.S. Govt. Printing Office), 971-985.
- Tissot, B. P., and Welte, D. H., 1984. *Petroleum Formation and Occurrence* (2nd Ed.): Berlin (Springer-Verlag).
- van Gorsel, J. T., and Troelstra, S. R., 1981. Late Neogene planktonic foraminiferal biostratigraphy and climatostratigraphy of the Solo River section (Java, Indonesia). *Mar. Micropaleontol.*, 6:183-209.
- Whitmarsh, R. B., 1974. Summary of general features of Arabian Sea and Red Sea Cenozoic history based on Leg 23 cores. In Whitmarsh, R. B., Weser, O. E., Ross, D. A., et al., *Init. Repts. DSDP*, 23: Washington (U.S. Govt. Printing Office), 1115-1123.
- , 1979. The Owen Basin off the southeast margin of Arabia and the evolution of the Owen Fracture Zone. *Geophys. J. R. Astron. Soc.*, 58:441-470.
- Whitmarsh, R. B., Weser, O. E., Ross, D. A., et al., 1974. *Init. Repts. DSDP*, 23: Washington (U.S. Govt. Printing Office).

Ms 117A-107

Table 13. Stratigraphic depths of the marker layers at Site 722.

	Hole 722A		Hole 722B		Holes 722A-722B
	Core, section, interval (cm)	Depth (mbsf)	Core, section interval (cm)	Depth (mbsf)	
OR-a ₀	1H-1, 50	0.50	1H-2, 85	2.35	-1.85
a ₁	1H-2, 35	1.85	1H-3, 50	3.50	-1.65
a ₂	1H-3, 135	4.35	2H-1, 25	5.75	-1.40
a ₃	1H-4, 115	5.65	2H-2, 20	7.20	-1.55
a ₄	1H-7, 30	9.30	2H-4, 65	10.65	-1.35
b ₁	2H-3, 20	13.00			
b ₂	2H-5, 95	16.75	3H-2, 105	17.65	-0.90
b ₃	2H-6, 30	17.60	3H-3, 45	18.55	-0.95
b ₄	3H-1, 60	20.00	3H-5, 10	21.20	-1.20
c ₁	3H-3, 85	23.25	3H-7, 15	24.25	-1.00
c ₂	3H-4, 115	25.05	4H-1, 85	25.55	-0.50
c ₃	3H-5, 85	26.25	4H-2, 60	26.80	-0.55
c ₄	3H-6, 100	27.90	4H-3, 85	28.55	-0.65
c ₅	3H-7, 40	28.80	4H-4, 40	29.60	-0.80
c ₆	4H-1, 30	29.30	4H-5, 5	30.75	-1.20
c ₇	4H-1, 140	30.40	4H-5, 100	31.70	-1.30
d ₁	4H-3, 65	32.65	4H-6, 140	33.60	-0.90
d ₁	4H-4, 5	33.35			
d ₂	4H-4, 65	33.95	5H-1, 70	35.00	-1.05
d ₂	4H-4, 150	34.80	5H-2, 10	35.90	-1.10
d ₃	4H-6, 80	37.10	5H-3, 100	38.30	-1.20
d ₃	4H-7, 25	38.05	5H-4, 30	39.10	-1.05
d ₄	5H-1, 90	39.50	5H-5, 20	40.50	-1.00
e ₁	5H-6, 115	47.25	6H-3, 130	48.20	-0.95
e ₂	6H-1, 105	49.25	6H-5, 60	50.50	-1.25
e ₃	6H-3, 40	51.60	6H-6, 130	52.70	-1.10
f ₁	6H-4, 120	53.90	7H-1, 45	53.65	0.25
f ₂	6H-5, 55	54.75	7H-1, 140	54.60	0.15
f ₃	6H-6, 130	57.00	7H-3, 85	57.05	-0.05
f ₄	7H-2, 45	59.45	7H-5, 100	60.20	-0.80
f ₅	7H-3, 50	61.00	7H-6, 120	61.90	-0.90
g ₁	7H-4, 40	62.40			
g ₂	7H-6, 90	65.90	8H-3, 75	66.65	-0.75
g ₃	8H-1, 30	67.50	8H-4, 120	68.60	-1.10
g ₄	8H-2, 45	69.15	8H-5, 140	70.30	-1.15
h ₁	8H-6, 60	75.30	9H-3, 50	76.00	-0.70
h ₂	8H-6, 110	75.80	9H-3, 110	76.60	-0.80
h ₃			9H-4, 110	78.10	
h ₄			9H-6, 60	80.60	
i ₁	9H-3, 90	80.70	9H-7, 50	82.00	-1.30
i ₂	9H-4, 100	82.30	10H-2, 60	84.30	-2.00
i ₃	9H-5, 70	83.50	10H-3, 75	85.95	-2.45
i ₄	10X-1, 5	86.55	10H-5, 40	88.60	-2.05
i ₅	10X-1, 125	87.75	10H-5, 135	89.55	-1.80
j ₁	10X-3, 25	89.75			
j ₁	10X-4, 60	91.60	11X-2, 5	93.45	-1.85
j ₂	10X-5, 60	93.10	11X-3, 35	95.25	-2.15
j ₃	10X-5, 120	93.70	11X-3, 80	95.70	-2.00

Table 13 (continued).

	Hole 722A		Hole 722B		Holes 722A-722B
	Core, section, interval (cm)	Depth (mbsf)	Core, section, interval (cm)	Depth (mbsf)	
OR-j ₄	11X-1, 50	96.70	11X-4, 50	96.90	-0.20
j ₅	11X-2, 95	98.65			
k ₁	11X-3, 100	100.20			
k ₂	11X-6, 100	104.70	12X-3, 45	104.95	-0.25
l ₁	12X-1, 45	106.35			
l ₂	12X-2, 45	107.85			
l ₃	12X-4, 10	110.50	13X-1, 65	111.85	-1.35
l ₄	12X-5, 115	113.05	13X-3, 45	114.65	-1.60
m ₁	13X-1, 50	116.10			
m ₂	13X-2, 90	118.00			
m ₃	13X-3, 35	118.95			
n ₁	13X-6, 95	124.05	14X-3, 90	124.80	-0.75
n ₂			14X-4, 65	126.05	
n ₃			14X-5, 20	127.10	
n ₄	14X-3, 45	128.75	15X-1, 95	131.45	-2.70
o ₁	14X-4, 100	130.80			
o ₂	14X-5, 15	131.45			
p ₁	15X-2, 120	137.60			
p ₂	15X-3, 65	138.55			
p ₃	15X-4, 45	139.85			
p ₄	15X-5, 40	141.30	16X-2, 35	142.05	-0.75
p ₅	15X-6, 70	143.10	16X-3, 75	143.95	-0.85
p ₆	15X-7, 20	144.10	16X-4, 15	144.85	-0.75
q ₁	16X-1, 65	145.25	16X-5, 35	146.55	-1.30
q ₂	16X-2, 30	146.40	16X-5, 130	147.50	-1.10
q ₃	16X-2, 110	147.20	16X-6, 60	148.30	-1.10
q ₄	16X-3, 100	148.60			
q ₅	16X-4, 30	149.40			
q ₆	16X-5, 15	150.75	17X-2, 5	151.45	-0.70
r ₁	17X-1, 125	155.55	17X-4, 145	155.85	-0.30
r ₂	17X-2, 110	156.90	17X-5, 75	156.65	0.20
r ₃			17X-C, 20	159.30	
r ₄			18X-1, 125	160.75	
s ₁			18X-4, 130	165.30	
s ₂			18X-6, 50	167.50	
s ₃			18X-7, 5	168.55	
s ₄	19X-1, 75	174.35	19X-1, 90	170.10	4.25
t ₁	19X-5, 30	179.90	19X-5, 90	176.10	3.80
t ₂	19X-6, 95	182.05	20X-1, 110	180.00	2.05
u ₁	20X-2, 65	185.45			
u ₂	20X-3, 75	187.05			
v ₁			21X-2, 40	190.40	
v ₂	21X-1, 150	194.50	21X-3, 90	192.40	2.10
w ₁	22X-3, 45	206.15	22X-6, 50	206.20	-0.05
w ₂	22X-4, 120	208.40			
x ₁			23X-3, 130	212.20	
x ₂	23X-2, 120	215.10	23X-5, 45	214.35	0.75
y ₁	23X-6, 55	220.45	24X-3, 45	220.95	-0.50
y ₂	23X-C, 40	222.20	24X-4, 75	222.75	-0.55

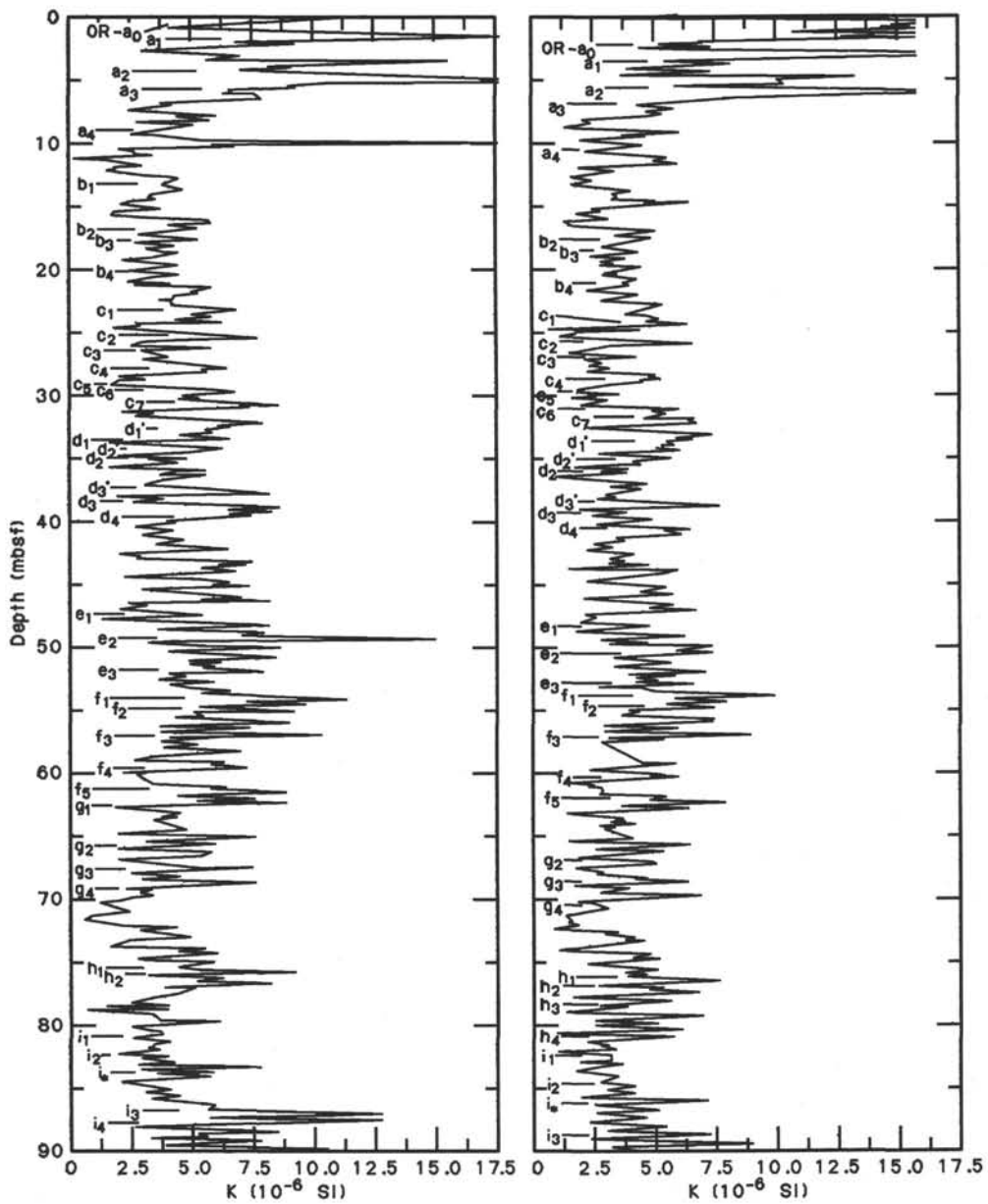


Figure 41. Volume magnetic susceptibility curve and positions of the marker layers in Hole 722A (left) and 722B (right).

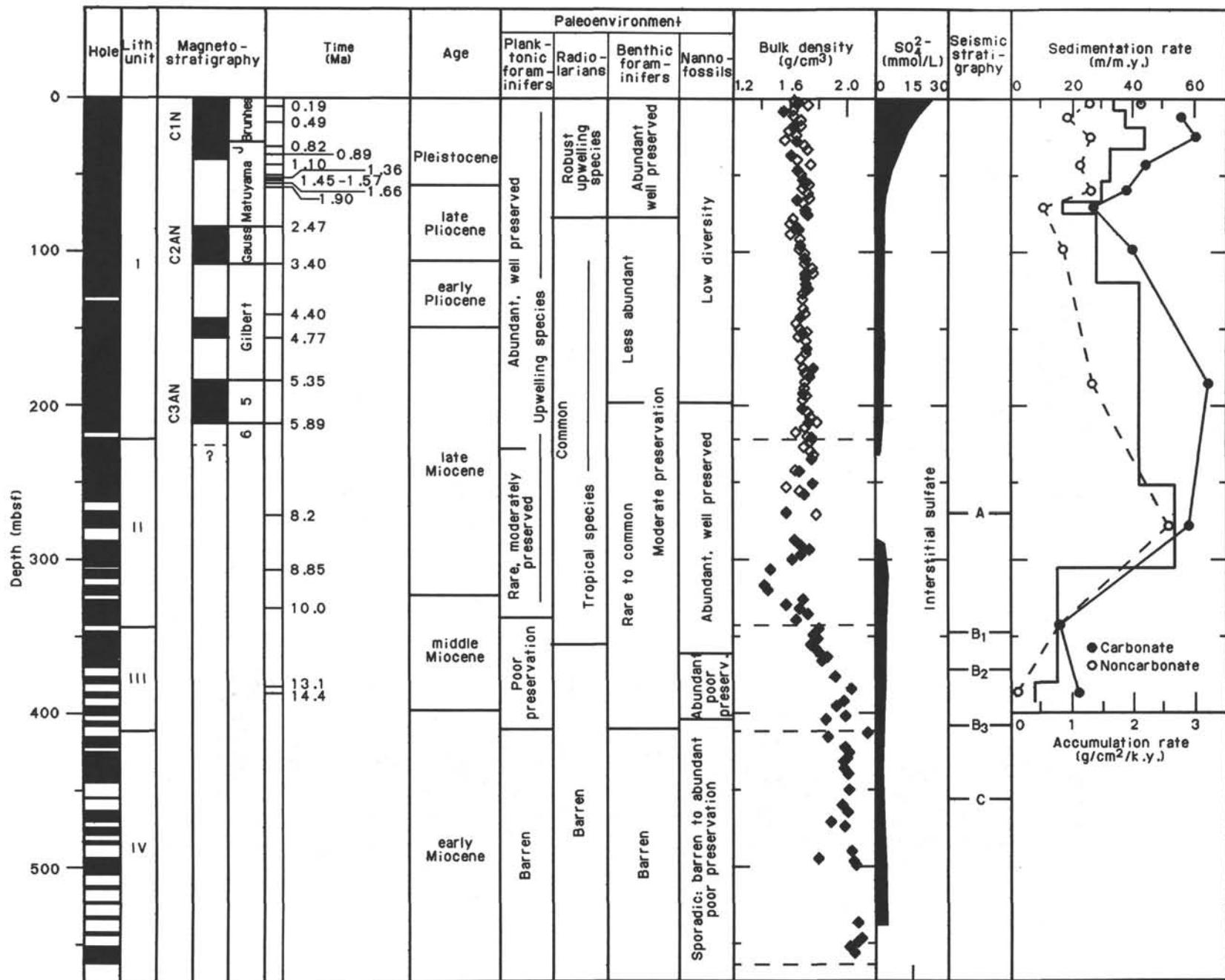


Figure 42. Summary chart outlining preliminary shipboard findings at Site 722.

Table 14. Corrected depth of core top for stratigraphic sub-bottom depth calculation.

Core	Hole 722A			Hole 722B		
	ODP top depth (mbsf)	Difference	Corrected top depth (mbsf)	ODP top depth (mbsf)	Difference	Corrected top depth (mbsf)
1	0.0	1.8	1.8	0.0	0.0	0.0
2	9.8	-0.6	11.0	5.5	0.3	5.8
3	19.4	0.2	20.8	15.1		15.4
4	29.0	0.7	31.1	24.7	0.5	25.5
5	38.6	-0.1	40.6	34.3	0.2	35.3
6	48.2	0.3	50.5	43.9	0.1	45.0
7	57.5	1.0	60.8	53.2	1.3	55.6
8	67.2	0.4	70.9	62.9	0.2	65.5
9	76.8	0.6	81.1	72.5	0.4	75.5
10	86.5	-0.1	90.7	82.2	-0.9	84.3
11	96.2	-1.8	98.6	91.9	0.1	94.1
12	105.9	1.2	109.5	101.5	-0.1	103.6
13	115.6	-0.7	118.5	111.2		113.3
14	125.3	1.8	129.1	120.9		123.0
15	134.9	-1.8	137.8	130.5		132.6
16	144.6	0.4	147.9	140.2		142.3
17	154.3	-0.6	157.0	149.9	0.5	152.5
18	163.9		166.6	159.5		162.1
19	173.6		176.3	169.2	4.1	175.9
20	183.3		186.0	178.9	-1.9	183.7
21	193.0		195.7	188.5		193.3
22	202.7	2.2	207.6	198.2		203.0
23	212.4	-0.8	216.5	207.9		212.7
24				217.5	-1.3	221.0

Note: ODP top depth = depth (mbsf) of core top calculated by the ODP CORELOG program data. Difference = difference in meters between the depth calculated by the ODP CORELOG data and the depth calculated by the layer-by-layer correlation method. Corrected top depth = depth (mbsf) of core top calculated by the layer-by-layer correlation method.

Table 15. Stratigraphic depths of the marker layers in Sites 722 and 721.

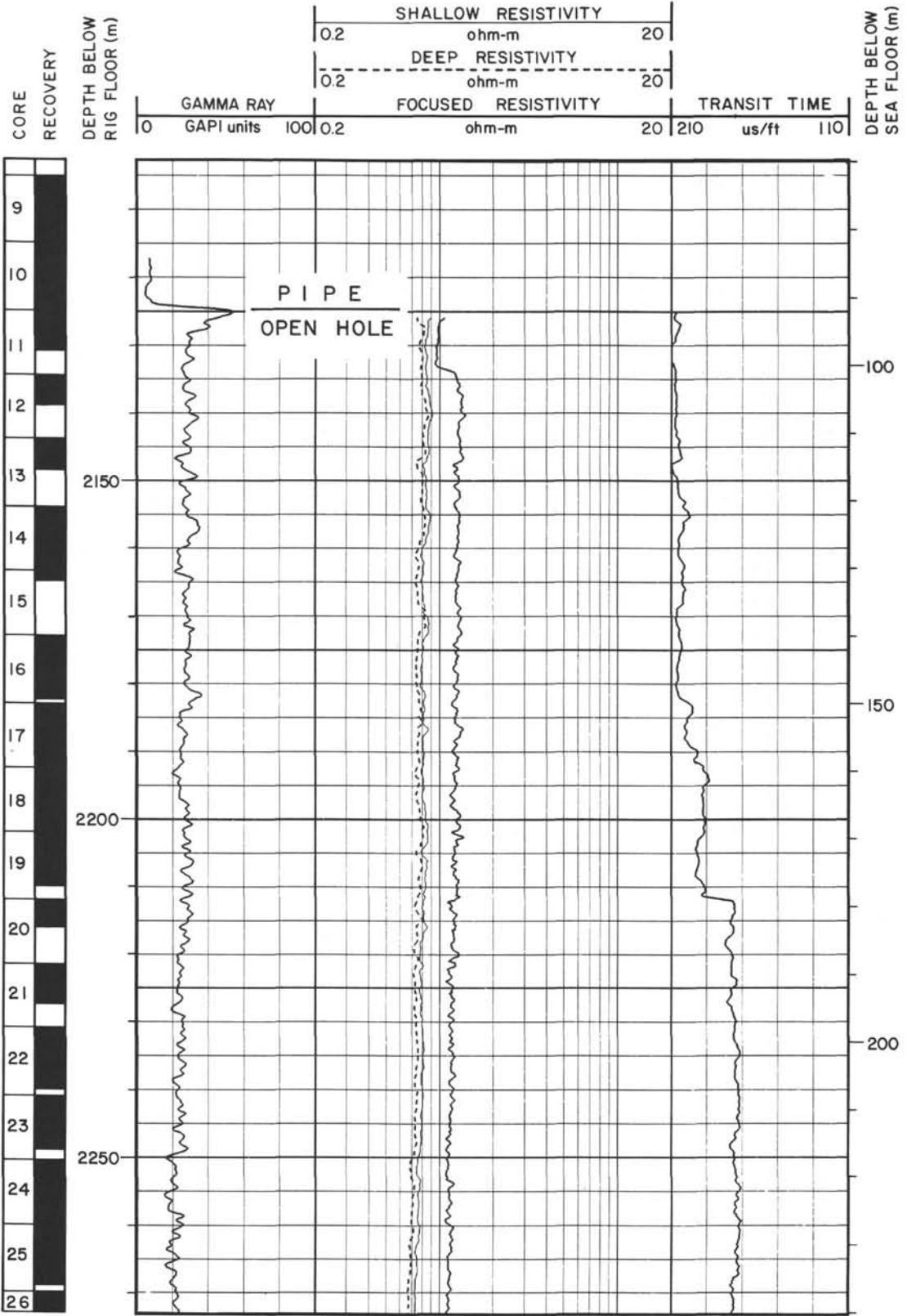
	Hole 721B		Hole 722A			Hole 722B		
	Core, section, interval (cm)	Corrected depth (mbsf)	Core, section, interval (cm)	ODP depth (mbsf)	Corrected depth (mbsf)	Core, section, interval (cm)	ODP depth (mbsf)	Corrected depth (mbsf)
OR-a ₀	1H-2, 105	2.55	1H-1, 50	0.50	2.30	1H-2, 85	2.35	2.35
a ₁	1H-3, 90	3.90	1H-2, 35	1.85	3.65	1H-3, 50	3.50	3.50
a ₂	1H-5, 45	6.45	1H-3, 135	4.35	6.15	2H-1, 25	5.75	6.05
a ₃	1H-6, 32	7.82	1H-4, 115	5.65	7.45	2H-2, 20	7.20	7.50
a ₄	2H-2, 25	11.15	1H-7, 30	9.30	11.10	2H-4, 65	10.65	10.95
b ₁	2H-4, 135	15.25	2H-3, 20	13.00	14.20			
b ₂	2H-6, 115	18.05	2H-5, 95	16.75	17.95	3H-2, 105	17.65	17.95
b ₃	2H-7, 40	18.80	2H-6, 30	17.60	18.80	3H-3, 45	18.55	18.85
b ₄	3H-1, 140	21.00	3H-1, 60	20.00	21.40	3H-5, 10	21.20	21.50
c ₁	3H-3, 130	23.90	3H-3, 85	23.25	24.65	3H-7, 15	24.25	24.55
c ₂	3H-4, 130	25.40	3H-4, 115	25.05	26.45	4H-1, 85	25.55	26.35
c ₃	3H-5, 105	26.65	3H-5, 85	26.25	27.65	4H-2, 60	26.80	27.60
c ₄	3H-6, 110	28.20	3H-6, 100	27.90	29.30	4H-3, 85	28.55	29.35
c ₅	3H-7, 50	29.10	3H-7, 40	28.80	30.20	4H-4, 40	29.60	30.40
c ₆	4H-1, 75	30.25	4H-1, 30	29.30	31.40	4H-5, 5	30.75	31.55
c ₇	4H-2, 20	31.20	4H-1, 140	30.40	32.50	4H-5, 100	31.70	32.50
d ₁	4H-3, 70	33.20	4H-3, 65	32.65	34.75	4H-6, 140	33.60	34.40
d ₁	4H-4, 0	34.00	4H-4, 5	33.35	35.45			
d ₂	4H-4, 70	34.70	4H-4, 65	33.95	36.05	5H-1, 70	35.00	36.00
d ₂	4H-4, 145	35.45	4H-4, 150	34.80	36.90	5H-2, 10	35.90	36.90
d ₃	4H-6, 85	37.85	4H-6, 80	37.10	39.20	5H-3, 100	38.30	39.30
d ₃	4H-7, 30	38.80	4H-7, 25	38.05	40.15	5H-4, 30	39.10	40.10
d ₄	5H-1, 125	41.35	5H-1, 90	39.50	41.50	5H-5, 20	40.50	41.50
e ₁	5H-6, 75	48.35	5H-6, 115	47.25	49.25	6H-3, 130	48.20	49.30
e ₂	6H-1, 35	50.45	6H-1, 105	49.25	51.55	6H-5, 60	50.50	51.60
e ₃	6H-2, 130	52.90	6H-3, 40	51.60	53.90	6H-6, 130	52.70	53.80
f ₁	6H-4, 115	55.75	6H-4, 120	53.90	56.20	7H-1 45	53.65	56.05
f ₂	6H-5, 60	56.70	6H-5, 55	54.75	57.05	7H-1, 140	54.60	57.00
f ₃	6H-7, 15	59.25	6H-6, 130	57.00	59.30	7H-3, 85	57.05	59.45
f ₄	7H-3, 45	62.55	7H-2, 45	59.45	62.75	7H-5, 100	60.20	62.60
f ₅	7H-4, 65	64.25	7H-3, 50	61.00	64.30	7H-6, 120	61.90	64.40
g ₁	7H-5, 45	65.55	7H-4, 40	62.40	65.70			
g ₂	8H-1, 85	69.05	7H-6, 90	65.90	69.20	8H-3, 75	66.65	69.25
g ₃	8H-2, 50	70.20	8H-1, 30	67.50	71.20	8H-4, 120	68.60	71.20
g ₄	8H-3, 70	71.90	8H-2, 45	69.15	72.85	8H-5, 140	70.30	72.90
h ₁	8H-7, 50	77.70	8H-6, 60	75.30	79.00	9H-3, 50	76.00	79.00
h ₂	9H-1, 35	78.25	8H-6, 110	75.80	79.50	9H-3, 110	76.60	79.60
h ₃	9H-2, 60	80.00				9H-4, 110	78.10	81.10
h ₄	9H-4, 40	82.80				9H-6, 60	80.60	83.60
i ₁	9H-5, 45	84.35	9H-3, 90	80.70	85.00	9H-7, 50	82.00	85.00
i ₂	9H-7, 40	87.30	9H-4, 100	82.30	86.60	10H-2, 60	84.30	86.40
i ₂	10X-2, 50	89.80	9H-5, 70	83.50	87.80	10H-3, 75	85.95	88.05
i ₃	10X-4, 25	92.55	10X-1, 5	86.55	90.75	10H-5, 40	88.60	90.70
i ₄	10X-4, 120	93.50	10X-1, 125	87.75	91.95	10H-5, 135	89.55	91.65
i ₅	10X-6, 75	96.05	10X-3, 25	89.75	93.95			
j ₁	11X-1, 120	98.20	10X-4, 60	91.60	95.80	11X-2, 5	93.45	95.65
j ₂	11X-2, 130	99.80	10X-5, 60	93.10	97.30	11X-3, 35	95.25	97.45
j ₃	11X-3, 70	100.70	10X-5, 120	93.70	97.90	11X-3, 80	95.70	97.90
j ₄	11X-4, 65	102.15	11X-1, 50	96.70	99.10	11X-4, 50	96.90	99.10

Table 15 (continued).

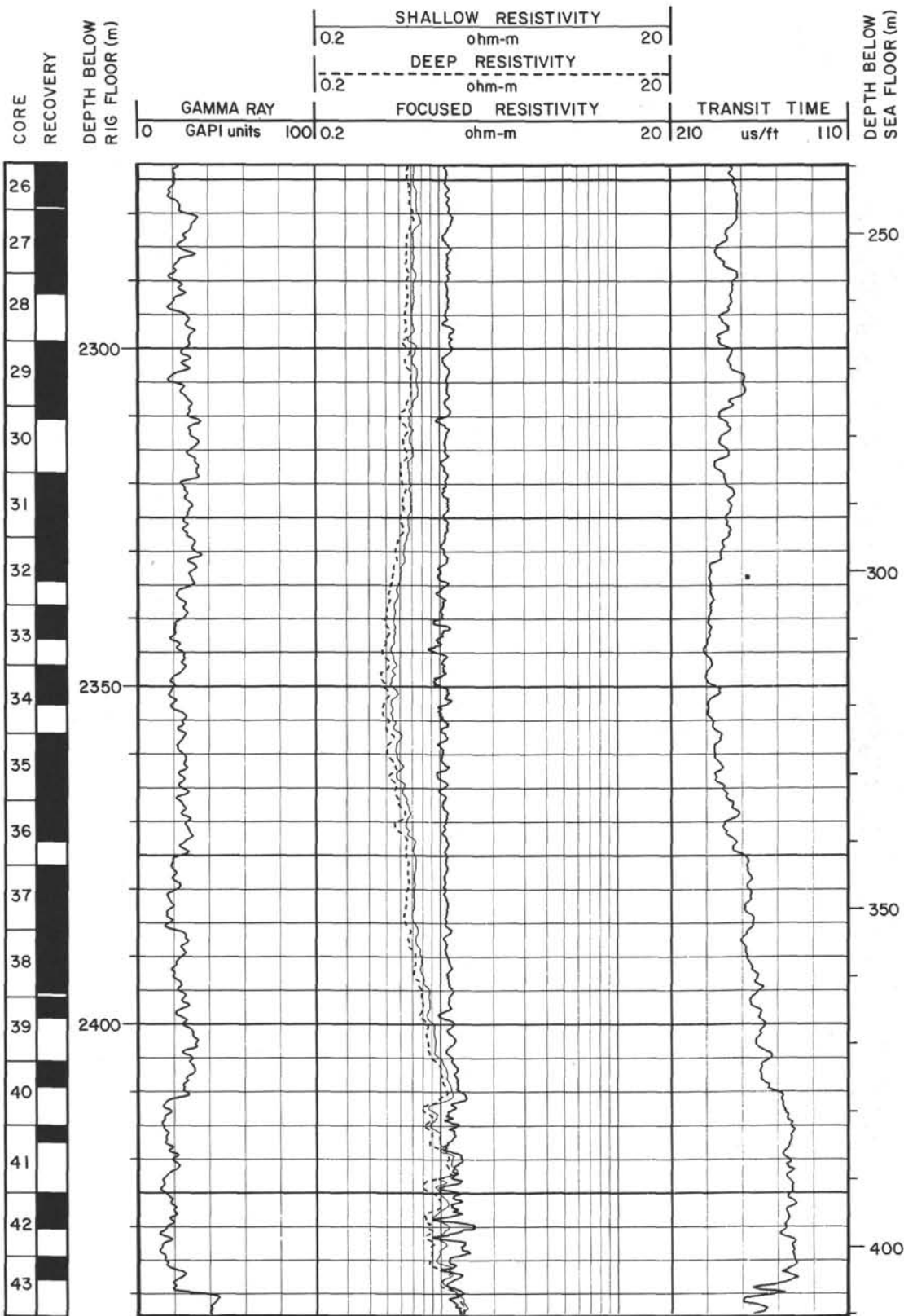
	Hole 721B		Hole 722A			Hole 722B		
	Core, section, interval (cm)	Corrected depth (mbsf)	Core, section, interval (cm)	ODP depth (mbsf)	Corrected depth (mbsf)	Core, section, interval (cm)	ODP depth (mbsf)	Corrected depth (mbsf)
OR-j ₅	11X-5, 90	103.90	11X-2, 95	98.65	101.05			
k ₁	12X-1, 55	105.45	11X-3, 100	100.20	102.60			
k ₂			11X-6, 100	104.70	107.10	12X-3, 45	104.95	107.05
l ₁	13X-1, 60	109.70	12X-1, 45	106.35	109.95			
l ₂	13X-2, 60	111.20	12X-2, 45	107.85	111.45			
l ₃	13X-4, 40	114.00	12X-4, 10	110.50	114.10	13X-1, 65	111.85	113.95
l ₄	13X-6, 30	116.90	12X-5, 115	113.05	116.65	13X-3, 45	114.65	116.75
m ₁	14X-2, 115	119.65	13X-1, 50	116.10	119.00			
m ₂	14X-3, 120	121.20	13X-2, 90	118.00	120.90			
m ₃	14X-4, 70	122.20	13X-3, 35	118.95	121.85			
n ₁	15X-1, 75	127.45	13X-6, 95	124.05	126.95	14X-3, 90	124.80	126.90
n ₂	15X-2, 135	129.55				14X-4, 65	126.05	128.15
n ₃	15X-3, 130	131.00				14X-5, 20	127.10	129.20
n ₄	15X-6, 15	134.35	14X-3, 45	128.75	132.55	15X-1, 95	131.45	133.55
o ₁	16X-2, 70	138.60	14X-4, 100	130.80	134.60			
o ₂	16X-3, 30	139.70	14X-5, 15	131.45	135.25			
p ₁	17X-1, 95	147.00	15X-2, 120	137.60	140.50			
p ₂	17X-2, 45	148.05	15X-3, 65	138.55	141.45			
p ₃	17X-3, 90	150.00	15X-4, 45	139.85	142.75			
p ₄	17X-4, 70	151.30	15X-5, 40	141.30	144.20	16X-2, 35	142.05	144.15
p ₅	17X-5, 100	153.10	15X-6, 70	143.10	146.00	16X-3, 75	143.95	146.05
p ₆	17X-6, 90	154.50	15X-7, 20	144.10	147.00	16X-4, 15	144.85	146.95
q ₁	18X-1, 120	157.00	16X-1, 65	145.25	148.55	16X-5, 35	146.55	148.65
q ₂	18X-2, 90	158.20	16X-2, 30	146.40	149.70	16X-5, 130	147.50	149.60
q ₃	18X-3, 45	159.25	16X-2, 110	147.20	150.50	16X-6, 60	148.30	150.40
q ₄	18X-4, 100	161.30	16X-3, 100	148.60	151.90			
q ₅	18X-5, 70	162.20	16X-4, 30	149.40	152.70			
q ₆	18X-6, 90	164.20	16X-5, 15	150.75	154.05	17X-2, 5	151.45	154.05
r ₁	19X-1, 110	166.60	17X-1, 125	155.55	158.25	17X-4, 145	155.85	158.45
r ₂	19X-2, 55	167.55	17X-2, 110	156.90	159.60	17X-5, 75	156.65	159.25
r ₃	19X-4, 70	170.70				17X-C, 20	159.30	161.90
r ₄	19X-5, 100	172.50				18X-1, 125	160.75	163.45
s ₁	20X-2, 105	177.75				18X-4, 130	165.30	168.00
s ₂	20X-3, 100	179.20				18X-6, 50	167.50	170.20
s ₃	20X-4, 65	180.35				18X-7, 5	168.55	171.25
s ₄	20X-4, 140	181.10	19X-1, 75	174.35	177.05	19X-1, 90	170.10	176.80
t ₁	21X-1, 20	185.10	19X-5, 30	179.90	182.60	19X-5, 90	176.10	182.80
t ₂	21X-2, 110	187.50	19X-6, 95	182.05	184.75	20X-1, 110	180.00	184.80
u ₁	22X-3, 30	197.90	20X-2, 65	185.45	188.15			
u ₂	22X-4, 65	199.75	20X-3, 75	187.05	189.75			
v ₁	23X-2, 45	206.25				21X-2, 40	190.40	195.20
v ₂	23X-3, 120	208.50	21X-1, 150	194.50	197.20	21X-3, 90	192.40	197.20
w ₁	24X-2, 60	216.00	22X-3, 45	206.15	211.15	22X-6, 50	206.20	211.00
w ₂	24X-3, 100	217.90	22X-4, 120	208.40	213.40			
x ₁	25X-3, 125	227.35				23X-3, 130	212.20	217.00
x ₂	25X-5, 65	229.75	23X-2, 120	215.10	219.20	23X-5, 45	214.35	219.15
y ₁	26X-3, 50	236.20	23X-6, 55	220.45	224.55	24X-3, 45	220.95	224.45
y ₂	26X-4, 90	238.10	23X-C, 40	222.20	226.30	24X-4, 75	222.75	226.25

Note: Depths are based on the correction factor of Table 14, which are based on ODP CORELOG data. Corrected depth = corrected depth for straigraphic thickness.

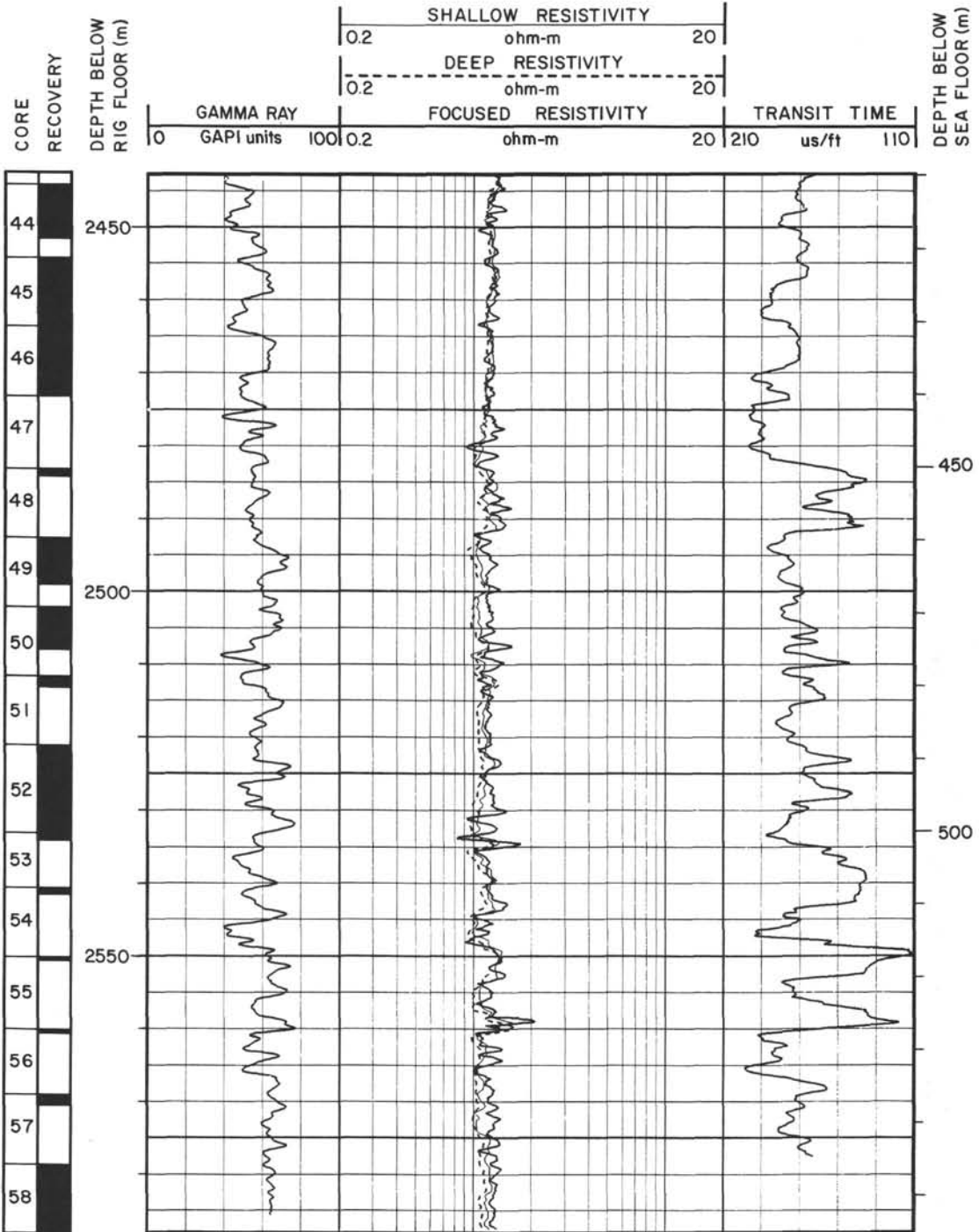
Summary Log for Hole 722B



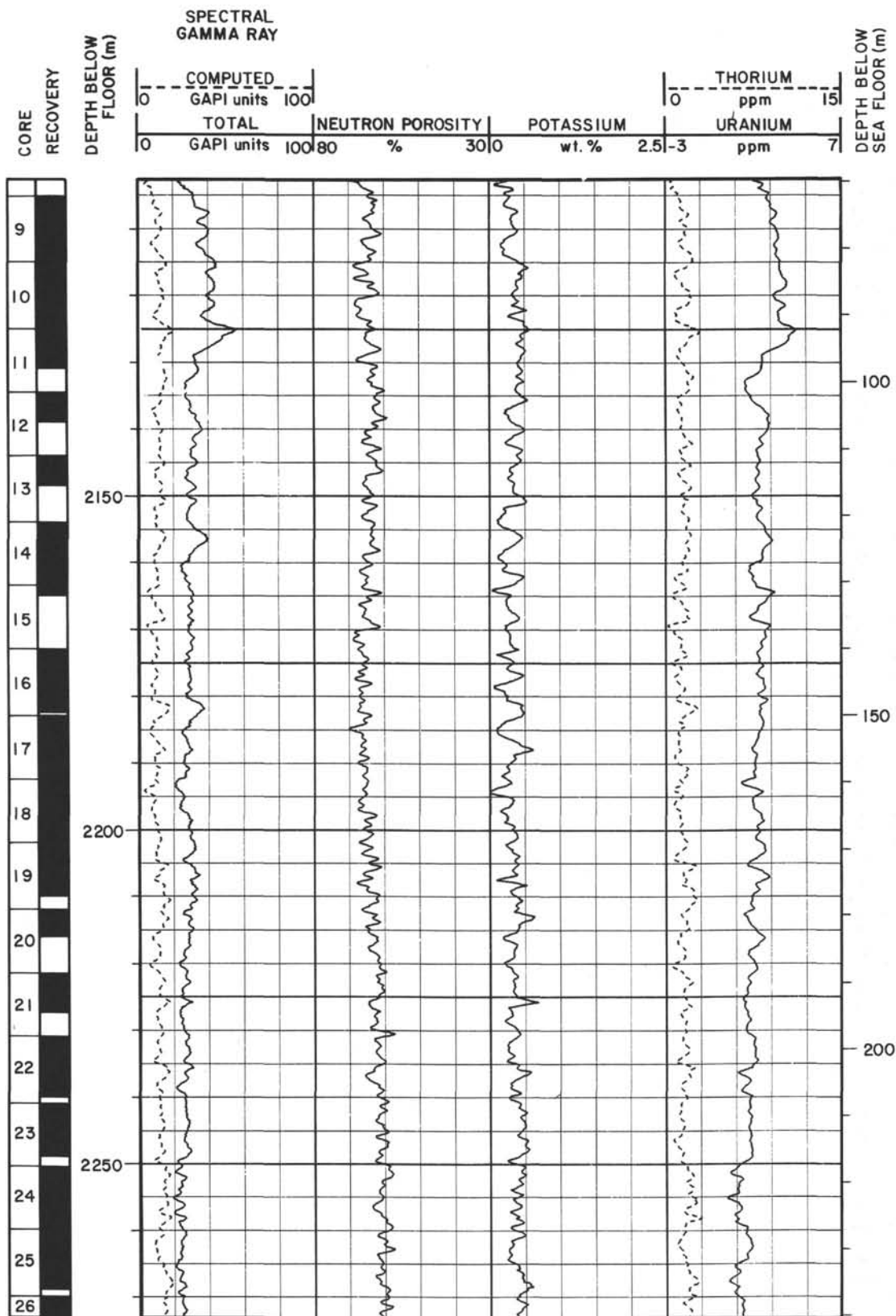
Summary Log for Hole 722B (continued)



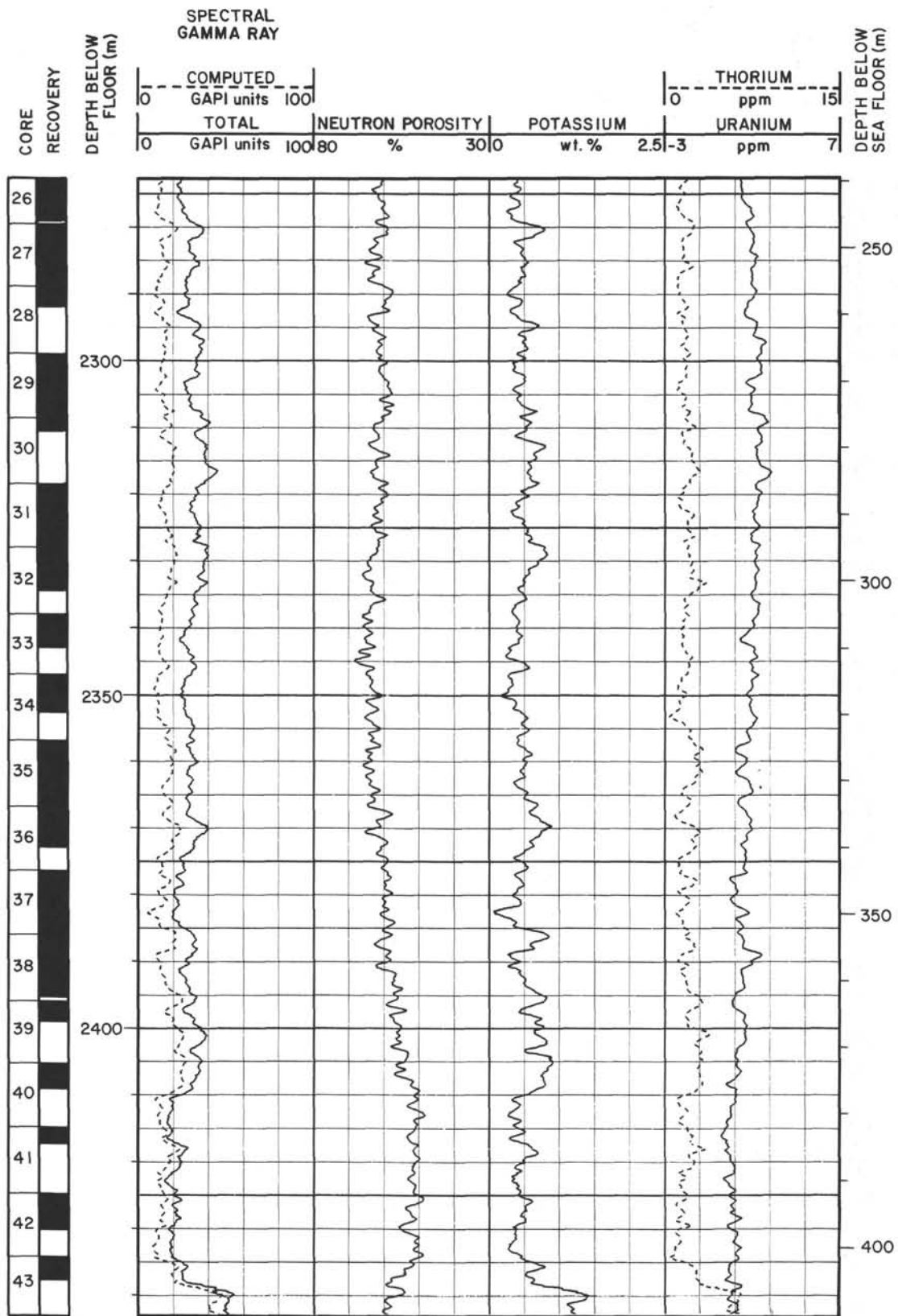
Summary Log for Hole 722B (continued)



Summary Log for Hole 722B (continued)



Summary Log for Hole 722B (continued)



Summary Log for Hole 722B (continued)

